



## CORE-II Virtual Special Issue

## An assessment of global and regional sea level for years 1993–2007 in a suite of interannual CORE-II simulations



Stephen M. Griffies<sup>a,\*</sup>, Jianjun Yin<sup>b</sup>, Paul J. Durack<sup>c</sup>, Paul Goddard<sup>b</sup>, Susan C. Bates<sup>d</sup>, Erik Behrens<sup>e</sup>, Mats Bentsen<sup>f</sup>, Daohua Bi<sup>g</sup>, Arne Biastoch<sup>e</sup>, Claus W. Böning<sup>e</sup>, Alexandra Bozec<sup>h</sup>, Eric Chassignet<sup>h</sup>, Gokhan Danabasoglu<sup>d</sup>, Sergey Danilov<sup>i</sup>, Catia M. Domingues<sup>j</sup>, Helge Drange<sup>k</sup>, Riccardo Farneti<sup>l</sup>, Elodie Fernandez<sup>m</sup>, Richard J. Greatbatch<sup>e</sup>, David M. Holland<sup>n</sup>, Mehmet Ilıcak<sup>f</sup>, William G. Large<sup>d</sup>, Katja Lorbacher<sup>g</sup>, Jianhua Lu<sup>h</sup>, Simon J. Marsland<sup>g</sup>, Akhilesh Mishra<sup>h</sup>, A.J. George Nurser<sup>o</sup>, David Salas y Méria<sup>p</sup>, Jaime B. Palter<sup>q</sup>, Bonita L. Samuels<sup>a</sup>, Jens Schröter<sup>i</sup>, Franziska U. Schwarzkopf<sup>e</sup>, Dmitry Sidorenko<sup>i</sup>, Anne Marie Treguier<sup>r</sup>, Yu-heng Tseng<sup>d</sup>, Hiroyuki Tsujino<sup>s</sup>, Petteri Uotila<sup>g</sup>, Sophie Valcke<sup>m</sup>, Aurore Voldoire<sup>p</sup>, Qiang Wang<sup>i</sup>, Michael Winton<sup>a</sup>, Xuebin Zhang<sup>t</sup>

<sup>a</sup> NOAA Geophysical Fluid Dynamics Laboratory, Princeton, USA

<sup>b</sup> Department of Geosciences, University of Arizona, Tucson, USA

<sup>c</sup> Program for Climate Model Diagnosis and Intercomparison, Lawrence Livermore National Laboratory, USA

<sup>d</sup> National Center for Atmospheric Research, Boulder, USA

<sup>e</sup> GEOMAR Helmholtz Centre for Ocean Research Kiel, Kiel, Germany

<sup>f</sup> Uni Climate, Uni Research Ltd., Bergen, Norway

<sup>g</sup> Centre for Australian Weather and Climate Research, a partnership between CSIRO and the Bureau of Meteorology, Commonwealth Scientific and Industrial Research Organisation (CSIRO), Melbourne, Australia

<sup>h</sup> Center for Ocean-Atmospheric Prediction Studies (COAPS), Florida State University, Tallahassee, FL, USA

<sup>i</sup> Alfred Wegener Institute (AWI) for Polar and Marine Research, Bremerhaven, Germany

<sup>j</sup> Antarctic Climate and Ecosystems Cooperative Research Centre, University of Tasmania, Hobart, Australia

<sup>k</sup> University of Bergen, Bergen, Norway

<sup>l</sup> International Centre for Theoretical Physics (ICTP), Trieste, Italy

<sup>m</sup> Centre Européen de Recherche et de Formation Avancée en Calcul Scientifique (CERFACS), URA 1875, CNRS/INSU, Toulouse, France

<sup>n</sup> New York University, New York 10012, USA

<sup>o</sup> National Oceanography Centre Southampton (NOCS), Southampton, UK

<sup>p</sup> Centre National de Recherches Météorologiques (CNRM-GAME), Toulouse, France

<sup>q</sup> McGill University, Montreal, Canada

<sup>r</sup> Laboratoire de Physique des Océans, UMR 6523, CNRS-Ifremer-IRD-UBO, Plouzane, France

<sup>s</sup> Meteorological Research Institute (MRI), Japan Meteorological Agency, Tsukuba, Japan

<sup>t</sup> Centre for Australian Weather and Climate Research, a partnership between CSIRO and the Bureau of Meteorology, Commonwealth Scientific and Industrial Research Organisation (CSIRO), Hobart, Australia

## ARTICLE INFO

## Article history:

Received 2 October 2013

Received in revised form 27 March 2014

Accepted 31 March 2014

Available online 21 April 2014

## Keywords:

Sea level

CORE global ocean-ice simulations

Steric sea level

Global sea level

Ocean heat content

## ABSTRACT

We provide an assessment of sea level simulated in a suite of global ocean-sea ice models using the interannual CORE atmospheric state to determine surface ocean boundary buoyancy and momentum fluxes. These CORE-II simulations are compared amongst themselves as well as to observation-based estimates. We focus on the final 15 years of the simulations (1993–2007), as this is a period where the CORE-II atmospheric state is well sampled, and it allows us to compare sea level related fields to both satellite and *in situ* analyses. The ensemble mean of the CORE-II simulations broadly agree with various global and regional observation-based analyses during this period, though with the global mean thermosteric sea level rise biased low relative to observation-based analyses. The simulations reveal a positive trend in dynamic sea level in the west Pacific and negative trend in the east, with this trend arising from wind shifts and regional changes in upper 700 m ocean heat content. The models also exhibit a thermosteric sea level rise in the subpolar North Atlantic associated with a transition around 1995/1996 of the North

\* Corresponding author. Tel.: +1 609 452 6672; fax: +1 609 987 5063.

E-mail address: [Stephen.Griffies@noaa.gov](mailto:Stephen.Griffies@noaa.gov) (S.M. Griffies).

Atlantic Oscillation to its negative phase, and the advection of warm subtropical waters into the subpolar gyre. Sea level trends are predominantly associated with steric trends, with thermosteric effects generally far larger than halosteric effects, except in the Arctic and North Atlantic. There is a general anti-correlation between thermosteric and halosteric effects for much of the World Ocean, associated with density compensated changes.

Published by Elsevier Ltd.

## 1. Introduction

There are growing observation-based measures of large-scale patterns of sea level variations with the advent of the Argo floats (since the early 2000s) and satellite altimeters (since 1993). Such measures provide a valuable means to evaluate aspects of global model simulations, such as the global ocean-sea ice simulations run as part of the interannual Coordinated Ocean-sea ice Reference Experiments (Griffies et al., 2009b; Danabasoglu et al., 2014). In this paper, we present an assessment of such CORE-II simulations from 13 model configurations, with a focus on their ability to capture observation-based trends in ocean heat content as well as steric, thermosteric and halosteric sea level.

Our assessment focuses on the final 15 year period (1993–2007) of the CORE-II simulations to enable direct comparison of the simulations to both *in situ* and satellite based analyses. During this relatively short period, sea level variations have a large component due to natural variability (Zhang and Church, 2012; Meyssignac et al., 2012). This situation is compatible with the CORE-II simulations, as they are primarily designed for studies of interannual variability (Doney et al., 2007; Large and Yeager, 2012). Focusing our assessment on these years also ensures that the Large and Yeager (2009) atmospheric state, used as part of the CORE-II air-sea flux calculations, contains interannual satellite-based radiation, which is available only after 1983.

The practical basis for our study is a suite of global ocean-sea ice models forced with 60 years of the interannual CORE-II atmospheric state from Large and Yeager (2009), with this atmosphere state repeated five times for a total of 300 years. Details of the protocol can be found in Griffies et al. (2009b), which focused on the use of a repeating annual cycle; i.e., the Normal Year Forcing of the CORE-I project. Further details specific to the interannual CORE-II protocol are provided in the Atlantic study by Danabasoglu et al. (2014), with that study also providing many details of the models forming the suite of CORE-II simulations analyzed here.

### 1.1. Questions asked in this paper

Sea level change due to human-induced climate change has the potential to affect coastal regions over the remainder of the 21st century and for centuries thereafter. From among the many physical processes impacting sea level, it is the evolution of land ice sheets on Greenland and Antarctica that offers the greatest degree of uncertainty and broadest potential for significant impact. For example, the growth and decay of ice sheets have caused sea level change on the order of 100 m over the recent 450 thousand years with fluctuations of about 100 thousand years (Lambeck et al., 2002; Rohling et al., 2009). We ignore here such sea level changes associated with melting land ice (except to the extent that such water fluxes are contained in the CORE-II river runoff data based on Dai et al., 2009). There are complementary global ocean-sea ice studies that consider the ocean's response to melt events, such as those from Gerdes et al. (2006), Stammer (2008), Weijer et al. (2012) and Lorbacher et al. (2012).

Ocean warming causes ocean volume to increase due to a decrease in density. As estimated by Church et al. (2011) and Gregory et al. (2013), such changes in global mean thermosteric

sea level determine about one-third to one-half of the observed global mean sea level rise during the late 20th and early 21st centuries, with changes in ocean mass contributing the remainder. Although limited largely to examinations of natural variability over the relatively short period of 1993–2007, our assessment is of some use to determine the suitability of global ocean-sea ice models for capturing longer term observed trends largely due to anthropogenic effects, such as those considered in Levitus et al. (2005), Boyer et al. (2005), Domingues et al. (2008), Ishii and Kimoto (2009), Hosoda et al. (2009), Durack and Wijffels (2010), Church et al. (2011), Gleckler et al. (2012) and Levitus et al. (2012). In particular, we can assess the ability of forced global ocean-sea ice models to represent observed changes in patterns of ocean heat content and thermosteric sea level change (Lombard et al., 2009; Kuhlbrodt and Gregory, 2012). Furthermore, we note the importance of ocean warming on ice shelf melt (e.g., Yin et al., 2011), with this connection providing yet another reason that an assessment of how models simulate observed warming provides a useful measure of their skill for making projections.

The following two questions regarding the global mean sea level trends and associated spatial patterns frame our assessment of the CORE-II simulations.

- GLOBAL MEAN THERMOSTERIC SEA LEVEL: Do CORE-II global ocean-sea ice simulations reproduce the observed global mean sea level variations associated with thermosteric effects estimated from the observation-based analyses? To address this question, we focus on ocean temperature and heat content trends, and how these trends are associated with changes in thermosteric sea level.
- PATTERNS OF DYNAMIC SEA LEVEL: Do CORE-II ocean-sea ice simulations reproduce observation-based changes to dynamic sea level patterns? To address this question, we partition dynamic sea level trends into their halosteric and thermosteric patterns, as well as bottom pressure contributions.

Answers to these questions are not simple, nor do we presume our contribution leads to unequivocal results. Nonetheless, we aim to provide physical and mathematical insight in the process of assessing the physical integrity of the CORE-II simulations. An underlying hypothesis of CORE is that global ocean-sea ice models coupled with the same prescribed atmospheric state produce similar simulations (Griffies et al., 2009b; Danabasoglu et al., 2014). We consider this hypothesis in the context of our sea level analysis. We hope that our presentation assists in the ongoing scientific quest to understand observed sea level changes, and to characterize some of its causes as realized in global ocean-sea ice models.

### 1.2. Style and structure of this paper

We aim to physically motivate and mathematically detail a suite of methods for sea level studies, providing sufficient information to both understand and reproduce our analyses. In this way, we hope that this paper serves both as a benchmark for how the present suite of CORE-II simulations performs in the representation of sea level, and provides a reference from which the reader may understand this, and other, studies of simulated sea level even after the models used here become obsolete.

The remainder of this paper consists of the following sections. We initiate the main text in Section 2 by considering aspects of the sea level question as framed by the CORE-II simulations with global ocean–sea ice models. In particular, we refine the questions posed in Section 1.1 by exposing some of the limitations inherent in the CORE-II experimental design and the atmospheric state used to drive the models. Our analysis of the global mean sea level from the CORE-II simulations is then presented in Section 3. It is here that we focus on the first question posed above concerning how well the CORE-II simulations represent the global thermosteric rise in sea level as compared to observation-based estimates. We follow in Section 4 with a discussion of the ocean heating trends over the years 1993–2007, with comparison to estimated observation-based trends. In Section 5 we then present the regional patterns of sea level (second question raised above), partitioning sea level trends into thermosteric, halosteric, and bottom pressure trends. We complete the main text with a summary and discussion in Section 6.

We provide a selection of support material in the appendices. Some of this material is rudimentary, yet it is central to the theoretical and practical foundation of this paper. Appendix A focuses on the global mean sea level question as posed in ocean–sea ice climate models, which can be addressed through kinematic considerations. Appendix B presents dynamical notions of use to interpret patterns of sea level, in particular the partitioning of sea level tendencies into thermosteric, halosteric, and bottom pressure tendencies. Appendix C examines the ability of ocean models to conserve heat throughout the ocean fluid.

### 1.3. Scope of our analysis

This paper contains a wealth of information in its many multi-panelled figures. However, we do not fully discuss each detail in the figures, as doing so requires a tremendous amount of discussion making a long paper even longer. We suggest that many readers may find it sufficient to focus on the CORE-II ensemble means that are provided for most of the figures, with our discussion often focusing on the ensemble mean.

Furthermore, our presentation is descriptive in nature, as framed within the physically based analysis methodology detailed in the appendices. There is, however, little insight offered for the underlying physical mechanisms that explain model–model or model–observational differences. For example, we do not try to associate a particular model behaviour with the choice of physical parameterization. Such work is beyond our scope, with the present analysis intent on helping to identify areas where process-based studies may be warranted to isolate mechanisms accounting for differences.

Some readers may be disappointed with our reticence to penetrate deeper into such mechanisms. We too are disappointed. However, we are limited in how much we can answer such questions based on available diagnostic output from the simulations. Nonetheless, this excuse, which is in fact ubiquitous in such comparison papers utilizing CORE or CMIP (Coupled Model Intercomparison Project) simulations, is unsatisfying. The logistics of coordinating a comparison become increasingly complex when aiming to compare detailed diagnostics, such as budget terms, in a consistent manner. Yet more should be done to mechanistically unravel model–model differences. We provide further comment in Section 6.6 regarding this point. We argue there that progress on this issue is possible, with one means requiring a physical process-based analysis of the heat, salt, and buoyancy budgets.

## 2. Sea level in CORE-II simulations

We frame here the sea level question for the CORE-II simulations. Of interest are salient ocean model fundamentals and limitations, and aspects of the CORE-II experimental design.

### 2.1. CORE-II simulations compared to CMIP

Many sea level simulations are based on global coupled climate or earth system models, such as those participating in the Coupled Model Intercomparison Project (CMIP) (Meehl et al., 2007; Taylor et al., 2012). We take a different approach here by considering a suite of global ocean–sea ice model configurations following the CORE-II protocol. Both CMIP and CORE-II allow one to study the role of natural and anthropogenic forcing on decadal time scales, as well as to consider elements of ocean and climate system predictability.

The interannually forced CORE-II simulations considered in this paper offer the potential for a mechanistic characterization of observed ocean changes over the years 1948–2007. Danabasoglu et al. (2014) provides an example for the North Atlantic, with further studies ongoing in the community. Nonetheless, it is important to note that this potential is rarely realised unambiguously, as there are practical limitations associated with an incomplete observational record; uncertainties in the prescribed atmospheric state used as part of the flux calculations, especially for years prior to the use of satellite radiation starting mid-1983; relative shortness of the atmospheric state that prompts its recycling; and the inevitable biases and limitations in numerical models. One further limitation concerns the CORE-II experimental design related to surface boundary fluxes. Namely, CORE-II eliminates an interactive atmospheric component. Doing so introduces uncertainties associated with missing or corrupted air–sea feedbacks and ambiguities concerning the surface salinity boundary condition. These issues are reviewed in Griffies et al. (2009b).

We here compare the CMIP and CORE approaches.

- **PRESCRIBED FORCING:** In the historical component of CMIP simulations, global climate models are forced with solar radiation and estimates of historical atmospheric composition/emissions/volcanoes. Air–sea fluxes are computed based on the evolving ocean, atmosphere, and sea ice states. For CORE-II, air–sea fluxes are computed based on a common bulk formula and common prescribed atmospheric state, with the prescribed atmospheric state estimated from reanalysis and observation-based products as compiled by Large and Yeager (2009). Only the ocean and sea ice are prognostic in CORE-II simulations. Hence, air–sea flux differences for CORE-II models arise from differences in the surface ocean and sea ice states.
- **UNCERTAINTIES:** For CMIP, there are uncertainties in the representation of atmospheric processes associated with buoyancy and momentum fluxes across the air–sea interface. Uncertainty and model spread are induced by the entire climate system (the atmosphere, ocean, ice, land surface, etc.). For CORE-II, there are uncertainties in how well the prescribed atmospheric state represents the real world. However, because the atmosphere is prescribed in CORE-II, model spread is induced only by the prognostic ocean and sea ice components. In principle, results from CORE-II can help interpret and attribute model spread in CMIP.
- **DRIFT:** For CMIP, changes in sea level associated with climate change scenarios are typically isolated by subtracting a control simulation, thus providing a means (albeit imperfect) to remove model drift. The CORE-II simulations derive their forcing based on a prescribed atmospheric state. There is no control in the sense used for CMIP. Model drift, particularly associated with deep ocean temperature and salinity, is a function of how long the model has been spun-up. The CORE-II protocol followed here considers five cycles of 60 years duration each (years 1948–2007), whereas the deep ocean takes order thousands of years to equilibrate (Stouffer, 2004; Danabasoglu, 2004; Wunsch and Heimbach, 2014).

- **INITIAL STATES:** The centennial-scale CMIP simulations generally start with a spun-up ocean state obtained by running the climate model for a time sufficient to reach quasi-equilibrium, whereas the more recent CMIP5 decadal prediction experiments initialize the ocean state based on observational estimates (Meehl et al., 2007; Taylor et al., 2012). The CORE-II simulations are initialized from observational estimates based on potential temperature and salinity from the Polar Science Center Hydrographic Climatology (PHC2; a blending of the Conkright et al. (2002) analysis with modifications in the Arctic based on Steele et al., 2001). Sea ice for CORE-II is generally initialized from a previous simulation. Further details for the CORE-II initialization can be found in Griffies et al. (2009b) and Danabasoglu et al. (2014).

One final point of comparison is to observe that the CMIP5 model archive contains results that are written in a common format with standardized names and grid information (Griffies et al., 2009a; Taylor et al., 2012). In contrast, CORE-II variable names generally differ across the models, as does the grid information, and even sign conventions on the vertical direction. The less strict protocol for CORE-II data submission facilitates the participation of a wider suite of research groups. Unfortunately, it places a burden on the analyst who must sift through the data on a model-by-model basis. We suggest that broadening the CORE project in a manner reflective of CMIP must include resources to produce model output in a common format.

## 2.2. What is “sea level” as computed by ocean models?

There are many terms used in the literature for “sea level” and its variants. We define those terms used in this paper, and in turn identify what is available from the CORE-II simulations.

### 2.2.1. Relative sea level

Relative sea level is the distance between the ocean bottom and the sea surface (see Section 13.1.2 of Church et al., 2013b). Relative sea level can thus change if the bottom changes due to solid earth geophysical processes, or the surface changes due to modifications of ocean mass or density. There are many geophysical processes that impact relative sea level, some involving dynamics of the liquid ocean (e.g., density and currents simulated in ocean climate models), and some involving other geophysical processes such as solid earth and gravitational dynamics.

### 2.2.2. Sea surface height (SSH)

The ocean–sea ice models used in this paper, as with nearly all global ocean climate models, assume a fixed land–sea configuration and fixed gravitational and rotational effects. We refer to the ocean surface computed by such models as the *sea surface height* (SSH) and denote it by  $\eta$ . In principle, the SSH measures the sea surface deviation from a constant geopotential surface. Note that we use the term SSH whether the model respects volume conserving Boussinesq kinematics or mass conserving non-Boussinesq kinematics (see below and Section 2.5).

### 2.2.3. Global mean sea level

Global mean sea level is given by

$$\bar{\eta} = \frac{\int \eta dA}{\int dA}, \quad (1)$$

where the area integral extends over the surface of the World Ocean. Global mean sea level reflects the global averaged impacts of changes to the ocean’s density structure and to its mass (Appendix A.2). It has been the subject of many studies, with Gregory et al.

(2013) quantifying how physical processes impact global mean sea level. Although no single location on the planet measures global mean sea level, it remains an important field to consider in all sea level studies.

### 2.2.4. Boussinesq fluid

The Boussinesq approximation is commonly made for ocean climate models (see Table 1), whereby the kinematics is approximated by those of a volume conserving fluid. The volume of a Boussinesq ocean changes in the presence of precipitation, evaporation, or runoff, and remains constant if the net volume of water added to the global ocean vanishes. In contrast, the mass of a Boussinesq ocean generally changes even without a boundary mass flux, since density changes translate into mass changes in a volume conserving fluid.

### 2.2.5. Non-Boussinesq fluid

Rather than conserving volume, the ocean fluid in fact conserves mass. The kinematics of a non-Boussinesq fluid respects the mass conserving nature of an ocean fluid parcel, with two of the contributing CORE-II models mass conserving (see Table 1). The total mass of a non-Boussinesq ocean changes in the presence of precipitation, evaporation, or runoff, and remains constant if these fluxes have a zero net over the globe. The volume of a non-Boussinesq ocean generally changes even without a boundary volume flux, since density changes translate into volume changes in a mass conserving fluid. Consequently, the budget for total ocean volume, and hence for the global mean sea level, includes source/sink terms arising from steric effects (see Griffies and Greatbatch, 2012 for much more on this point).

### 2.2.6. Steric effects

As seawater density changes from changes in the temperature, salinity, and pressure, so too does sea level through expansion or contraction of the ocean volume. Density induced sea level changes are referred to here as *steric effects*. We sometimes refer to the sea level changes associated with steric effects as the *steric sea level*, along with its components *thermosteric sea level* and *halosteric sea level*.

Griffies and Greatbatch (2012) in their Section 1.2 identify three distinct steric effects. We summarize here some of the salient points, which are presented in more detail in the Appendices A and B in the present paper. These points prove to be important for how we analyze sea level in the CORE simulations.

1. The *global steric* effect is given by (see Eq. (27) in Appendix A.2)

$$\left(\frac{\partial \bar{\eta}}{\partial t}\right)^{\text{global steric}} \equiv -\frac{\mathcal{V}}{\mathcal{A}} \left(\frac{1}{\langle \rho \rangle} \frac{\partial \langle \rho \rangle}{\partial t}\right), \quad (2)$$

where  $\mathcal{V}/\mathcal{A}$  is the ratio of the global ocean volume to global ocean surface area; i.e., the global mean ocean depth. The global steric effect gives rise to a change in global mean sea level,  $\bar{\eta}$ , due to changes in global mean *in situ* density  $\langle \rho \rangle$ . For example, as global mean density decreases, global mean sea level rises.

2. The *local steric* effect is given by (see Eq. (47) in Appendix B.1)

$$\left(\frac{\partial \eta}{\partial t}\right)^{\text{local steric}} = -\frac{1}{\rho_o} \int_{-H}^{\eta} \frac{\partial \rho}{\partial t} dz, \quad (3)$$

where the vertical integral of the local time tendency of *in situ* density extends over the full ocean column from the bottom at  $z = -H(x, y)$  to surface at  $z = \eta(x, y, t)$ , and where  $\rho_o$  is a representative ocean density commonly used to approximate the surface density  $\rho(\eta)$ . The local steric effect accounts for changes in sea level arising from local time tendencies of density. We can partition sea level evolution in a hydrostatic fluid into the local

**Table 1**

Summary of various properties of the ocean models used in this study, with focus here on choices that directly impact on simulated sea level. Many further details important for the CORE-II configurations chosen by the model groups are provided in the appendices to Danabasoglu et al. (2014). The first column of this table gives the model name, and the second column notes the name of the ocean model code. The next column provides the horizontal grid resolution and vertical degrees of freedom. All models have non-uniform grids in the both the horizontal and vertical, so the horizontal resolution is a nominal value that roughly corresponds to the indicated uniform grid resolution. The fourth column notes whether the model kinematics uses the volume conserving Boussinesq approximation or mass conserving non-Boussinesq formulation. The fifth column indicates the global mean of the geothermal heat flux, with most models choosing not to use geothermal heating. Note that all models that use geothermal heating apply it according to a regional pattern, with just the global ocean mean reported in this table. The sixth column notes whether the ocean model uses a real water flux for evaporation, precipitation, and rivers, or rather a virtual salt flux. The seventh column notes whether the model conserves total ocean heat, as determined by comparing the global mean temperature evolution to the ocean boundary heat fluxes (Appendix C.2). FSU-HYCOM is the only model that fails to conserve heat, with an estimated heat non-conservation of  $+1 \text{ W m}^{-2}$ .

Model	Ocean code	Grid size	Boussinesq	Geothermal $\text{W m}^{-2}$	Real water	Heat conserved
ACCESS	MOM	1 deg $\times$ 50	Yes	0	Yes	Yes
AWI	FESOM	1 deg $\times$ 46	Yes	0	No	Yes
Bergen	Bergen	1 deg $\times$ 51	No	0	no	Yes
CERFACS	NEMO	1 deg $\times$ 42	Yes	0.084	Yes	Yes
CNRM	NEMO	1 deg $\times$ 42	Yes	0.084	Yes	Yes
FSU	HYCOM	1 deg $\times$ 32	No	0	No	No ( $+1 \text{ W m}^{-2}$ )
GFDL-GOLD	GOLD	1 deg $\times$ 63	Yes	0.06	Yes	Yes
GFDL-MOM	MOM	1 deg $\times$ 50	Yes	0.06	Yes	Yes
ICTP	MOM	2 deg $\times$ 30	Yes	0.06	Yes	Yes
Kiel	NEMO	0.5 deg $\times$ 46	Yes	0	Yes	Yes
MRI	MRI.COM	1 deg $\times$ 50	Yes	0	Yes	Yes
NCAR	POP	1 deg $\times$ 60	Yes	0	No	Yes
NOCS	NEMO	1 deg $\times$ 75	Yes	0	Yes	Yes

steric effect plus a term arising from changes in the mass within a fluid column (Section B.1). The mass term is found to be about an order of magnitude smaller in the CORE-II simulations than the local steric term (compare Figs. 19 and 20).

3. The non-Boussinesq steric effect is given by (see Eq. (15) in Appendix A.1)

$$\left(\frac{\partial \eta}{\partial t}\right)^{\text{non-bouss steric}} = - \int_{-H}^{\eta} \frac{1}{\rho} \frac{d\rho}{dt} dz, \quad (4)$$

where  $d\rho/dt$  is the material or Lagrangian time derivative of *in situ* density. The non-Boussinesq steric effect is thoroughly detailed in Griffies and Greatbatch (2012), with particular focus on how physical processes (e.g., mixing, eddy transport, boundary fluxes of buoyancy, nonlinear equation of state effects) affect global mean sea level. However, the non-Boussinesq steric effect is not of direct concern in the present paper.

Although these three steric effects are associated with density, they generally refer to physically distinct processes and thus manifest in ocean models in distinct manners. In particular, sea level in a mass conserving non-Boussinesq model is impacted by all three steric effects. In contrast, as emphasized by Greatbatch (1994), the prognostic sea level in Boussinesq fluids is not impacted by the global steric effect nor the non-Boussinesq steric effect. Additionally, due to the use of volume conserving kinematics, Boussinesq fluids alter mass, and hence bottom pressure, when density changes (Huang and Jin, 2002). To determine changes in global mean steric sea level in Boussinesq models, it is necessary to perform an *a posteriori* diagnostic calculation. We detail salient diagnostic methods in Appendix A.3 (see also Appendix D in Griffies and Greatbatch (2012)).

Although the prognostic sea level in Boussinesq models is unaffected by global steric and non-Boussinesq steric effects, it is influenced by local steric effects. Hence, both Boussinesq and non-Boussinesq sea level patterns are affected by changes in ocean temperature, salinity, and pressure. For the present paper, we are concerned with global steric effects when considering global mean sea level, and local steric effects when considering patterns of sea level change.

### 2.2.7. Dynamic sea level (DSL)

The global spatial anomaly of SSH is referred to as the *dynamic sea level*,  $\zeta$ , and is determined according to

$$\zeta = \eta - \bar{\eta}. \quad (5)$$

DSL gradients give rise to pressure forces acting to accelerate fluid motion. SSH is identical to the DSL for the special case of a volume conserving Boussinesq model employing zero surface water fluxes (e.g., virtual salt flux models; Section 2.5). For more realistic models, such as mass conserving non-Boussinesq models, models with a mass/volume flux across the ocean surface, and/or models impacted by changes in the atmospheric loading, the SSH also includes an evolving global mean component, in which case  $\zeta$  and  $\eta$  differ.

Horizontal patterns of dynamic sea level reflect nearly all of the many physical oceanographic processes active in the ocean, from the bottom to the surface. We may compute such patterns using either a mass conserving non-Boussinesq ocean model, or volume conserving Boussinesq model, with negligible difference seen at the large scales of concern here (e.g., see Fig. 3 in Griffies and Greatbatch (2012)). In particular, regional impacts of local steric changes are included in both Boussinesq and non-Boussinesq models (see Appendix B).

### 2.2.8. Sea level under sea ice

The upper ocean surface responds to the pressure loading from sea ice,  $p_{\text{ice}}$ , in an inverse barometer manner (see Appendix C to Griffies and Greatbatch, 2012). Some models in this study (e.g., GFDL-MOM, GFDL-GOLD) depress their ocean model free surface under sea ice, whereas others do not and so in effect levitate their sea ice. We measure the effective sea level defined according to the free surface plus any applied loading from ice (see Eq. (206) in Griffies and Greatbatch (2012))

$$\eta^{\text{effective}} = \eta + \frac{p_{\text{ice}}}{g \rho_o}, \quad (6)$$

where  $g$  is the gravitational acceleration and  $\rho_o = 1035 \text{ kg m}^{-3}$  is a representative ocean density. This is the sea level relevant for climate impacts, as, for example, considered by Kopp et al. (2010) and Yin et al. (2010a).

### 2.2.9. Static equilibrium sea level

In the absence of ocean currents, a resting sea level coincides with a level of constant geopotential, which defines the static equilibrium sea level. Changes in the mass field of the earth, including changes in the ocean mass, impact on the static equilibrium sea level, as do effects from the earth's rotation and solid-earth motions (e.g., Mitrovica et al., 2001, 2010). An interactive on-line computation of

this effect on sea level has yet to be incorporated into global climate models.

### 2.3. Comments on thermosteric effects

Ocean mass, heat, and salt are conserved so that their total ocean content is altered only through associated boundary fluxes. In contrast, neither ocean volume nor buoyancy are conserved in a mass conserving non-Boussinesq ocean. Rather, ocean volume and buoyancy are altered by interior sources and sinks, even when there is no corresponding flux across the ocean surface. A key reason neither are conserved relates to the nonlinear equation of state for seawater. One central nonlinearity for sea level studies concerns the temperature and pressure dependence of the thermal expansion coefficient

$$\alpha = -\frac{1}{\rho} \frac{\partial \rho}{\partial \Theta}, \quad (7)$$

where  $\rho$  is the *in situ* density and  $\Theta$  is the potential or conservative temperature of seawater (McDougall, 2003; IOC et al., 2010).<sup>1</sup> It is the thermal expansion coefficient that translates a change in ocean temperature to a change in buoyancy, and thus to a change in ocean volume and sea level. The thermal expansion coefficient is roughly ten times larger in the surface tropical waters than surface high latitudes (Fig. 1). It also reaches a minimum around 1500 m in the cold abyss, but increases towards the bottom due to pressure effects (seawater is more compressible as pressure increases). Although there are some rare regions of cold and fresh water where heating increases density, in the bulk of the ocean heating reduces seawater density and so raises sea level.

To illustrate how variations in the thermal expansion can impact on sea level changes, consider expression (3) for the local steric effect, and isolate the impacts from temperature tendencies

$$\left(\frac{\partial \eta}{\partial t}\right)^{\text{local thermosteric}} = \int_{-H}^{\eta} \alpha \left(\frac{\partial \Theta}{\partial t}\right) dz. \quad (8)$$

A nonzero temperature tendency arises when heat converges or diverges from a region, via either boundary heat fluxes or interior ocean heat transport. The large variations in  $\alpha$  shown in Fig. 1 mean that where heat is deposited or removed determines the degree to which heating alters sea level. Furthermore, the rather large spatial gradients of  $\alpha$  mean that transport of heat from one region to another, especially in the meridional direction, can modify sea level even without altering the total ocean heat content.

The horizontal map in Fig. 1 indicates that tropical surface heating leads to roughly ten times larger thermosteric sea level rise than the same heating in the high latitude surface ocean (see also Lowe and Gregory, 2006). The zonal mean map indicates that heat deposited in the upper tropical ocean leads to more sea level rise than the same heat deposited to the deeper ocean. Conversely, high latitude surface heating leads to less sea level rise than deep high latitude heating. Additionally, heating generally remains in the upper tropical ocean since it is more highly stratified than the high latitude. In general, warming enhances the upper ocean stratification (e.g., Capotondi et al., 2012), and so affects how and where warming impacts sea level.

There is an additional complexity impacting high latitude sea level. Namely, surface warming generally enhances ocean stratifi-

cation and leads to reduced deep water formation in the high latitudes. As a result, heat that otherwise leaves the abyssal high latitude ocean through convective activity will remain in the abyss, thus giving rise to deep heating relative to the case where convective ventilation occurs. Sequestering warm water in the abyss in turn contributes to sea level rise, and it does so more than if the same heat was near the surface in the high latitudes.

The story about thermosteric sea level change is thus intimately related to the amount of heating applied to the ocean, where that heating occurs, and where the heat is transported (Kuhlbrodt and Gregory, 2012; Hallberg et al., 2013). Furthermore, as the ocean warms, the efficiency by which heating raises sea level increases since the thermal expansion coefficient generally increases as seawater warms. That is, sea level rise through thermosteric processes accelerates as the ocean warms, with this acceleration a result of thermodynamic properties of the seawater equation of state (IOC et al., 2010).

### 2.4. Comments on halosteric effects

We now consider how local halosteric effects impact on sea level. For this purpose, consider expression (3) for the local steric effect, and isolate the impacts from salinity tendencies

$$\left(\frac{\partial \eta}{\partial t}\right)^{\text{local halosteric}} = -\int_{-H}^{\eta} \beta \left(\frac{\partial S}{\partial t}\right) dz, \quad (9)$$

where

$$\beta = \frac{1}{\rho} \frac{\partial \rho}{\partial S} \quad (10)$$

is the haline contraction coefficient. As for ocean heating, sea level is impacted both by the magnitude of the salinity tendencies, as well as spatial patterns of  $\beta$ . We note here two important reasons why the halosteric effect is far smaller in its impacts on global mean sea level relative to the thermosteric effect.

- As seen in Fig. 1, the haline contraction coefficient has far less relative spatial variation than corresponding variations in the thermal expansion coefficient. Values of  $\beta$  change on the order of 5% globally, which contrasts to the factor of 10 variations seen in the thermal expansion coefficient. Hence, for many purposes, it can be accurate enough to assume  $\beta$  is constant over the globe.
- Salt is exchanged principally via the relatively small amounts associated with seasonal melt and formation of sea ice. In turn, the total salt mass in the World Ocean is nearly constant on climate time scales. This property holds even with trends in sea ice and the measurable impact on sea level (Shepherd et al., 2010). Relatedly, the best observational precision on salinity measurements is 0.002 PSS-78, which is far larger than potential global mean salinity changes associated with sea ice trends. Combined with the relatively small spatial variations in  $\beta$ , we conclude that the global halosteric effects are far smaller than global thermosteric effects (see also Section A.5 for more details).

In contrast to their global effects, halosteric contributions to regional sea level trends can be significant. In particular, the North Atlantic and Arctic oceans exhibit important trends in sea level associated with halosteric effects (Section 5.3). Halosteric effects are significant in these regions due to the nontrivial salinity tendencies, and due to the very small thermal expansion coefficient in the high latitudes that suppresses thermosteric effects. Furthermore, the absolute value of the haline contraction coefficient is such that a unit change in salinity (g/kg) renders a larger change in density than a unit change in temperature (degrees C).

<sup>1</sup> "Temperature" in this paper refers to the ocean model prognostic potential temperature or the prognostic conservative temperature. The alternative *in situ* temperature is not a prognostic variable in ocean models since it does not provide a precise measure of ocean heat (McDougall, 2003). ACCESS is the only model in this study that uses the conservative temperature of McDougall (2003), as recommended by IOC et al. (2010). All other models use potential temperature for their prognostic temperature field. We note that many observation-based analysis products supply *in situ* temperature. Conversion to potential or conservative temperature is required before comparing to model output.

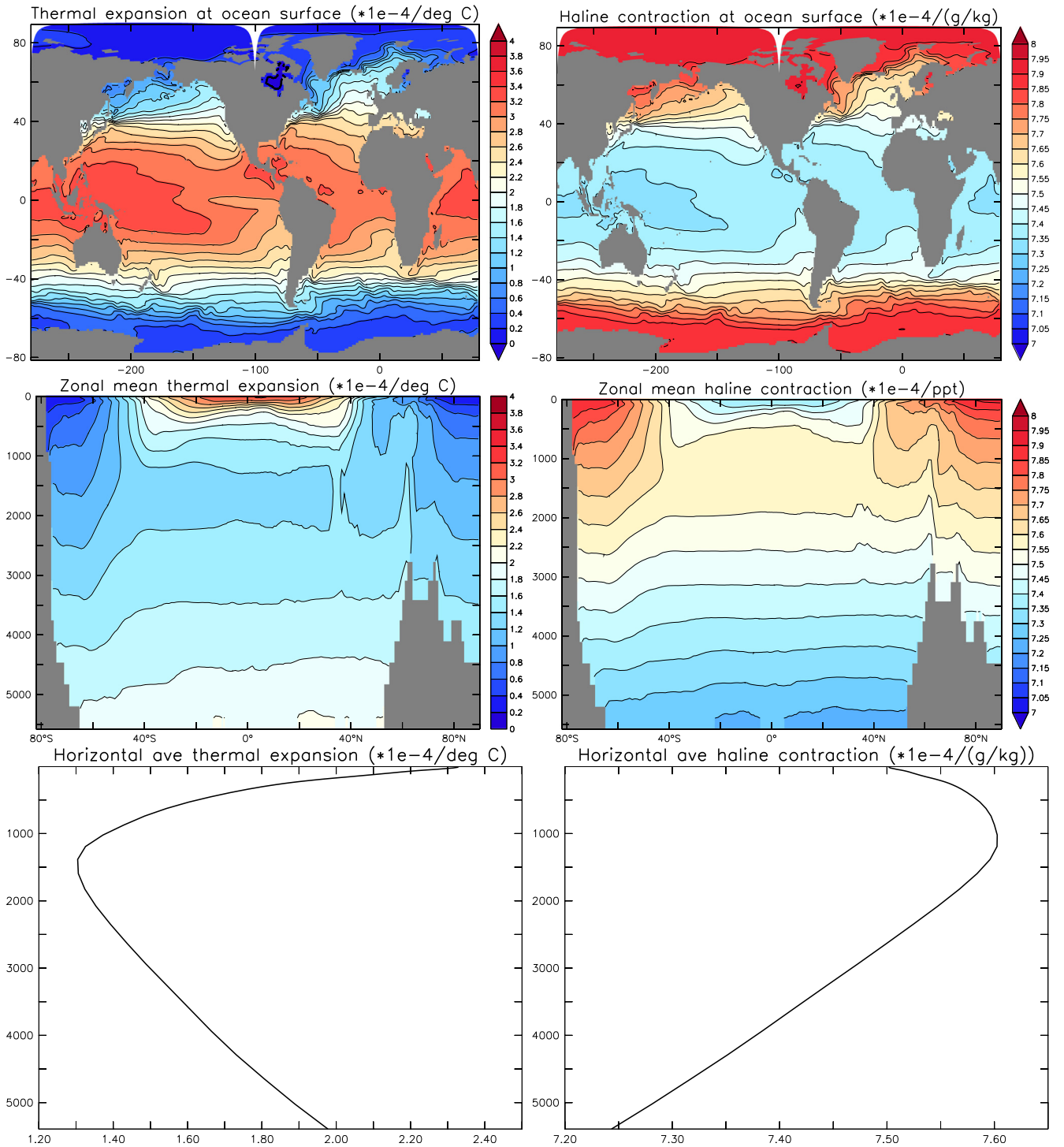


**Fig. 1.** Left column: climatological mean thermal expansion coefficient,  $\alpha$  (Eq. (7)). Right column: climatological mean haline contraction coefficient,  $\beta$  (Eq. (10)). We show values at the ocean surface, zonal average, and global horizontal mean, each multiplied by  $10^4$ . These results are based on a simulation using the GFDL-MOM configuration forced for 20 years using the repeating annual cycle from the Normal Year Forcing of Large and Yeager (2009) as per the protocol of Griffies et al. (2009b). For the thermal expansion coefficient, note the larger values in the tropics (up to ten times larger than the poles); minimum around 1500 m, and increase towards the deep ocean. The global mean over the upper 1000 m is around  $1.7 \times 10^{-4} \text{ } ^\circ\text{C}^{-1}$ , whereas the global mean over the full ocean is roughly  $1.54 \times 10^{-4} \text{ } ^\circ\text{C}^{-1}$ . The global mean haline contraction coefficient over the upper 1000 m is around  $7.6 \times 10^{-4} \text{ (g/kg)}^{-1}$ , whereas the global mean over the full ocean is roughly  $7.5 \times 10^{-4} \text{ (g/kg)}^{-1}$ . In general there is a far smaller range in values of  $\beta$  (only a few percent) relative to those of  $\alpha$  (upwards of a factor of 10). The wide range of variations for  $\alpha$  relative to the far smaller variations in  $\beta$  play a fundamental role in determining how surface boundary buoyancy fluxes and ocean transport/mixing impact on sea level.

### 2.5. Ocean model algorithmic choices directly affecting sea level simulations

All models used for this study assume a spherical geometry when formulating the ocean equations; consider a constant gravitational acceleration; retain a static land-sea boundary; and

ignore impacts on sea level from the mass of the overlying atmosphere. There are further algorithmic assumptions that directly impact on simulated sea level, with models used here choosing differing approaches. In general, how an ocean model represents the sea surface height determines the utility of a model for studying questions about sea level.

### 2.5.1. Rigid lid approximation

Rigid lid Boussinesq models retain a constant ocean volume, so do not transfer water across the ocean surface (Huang, 1993; Griffies et al., 2001; Yin et al., 2010b). Additionally, rigid lid models do not directly compute an undulating surface height. Hence, the analyst must resort to indirect methods to extract sea level information from model output, with Gregory et al. (2001) providing a summary of the available methods. There is no model used in the present CORE-II study that employs the rigid lid approximation, since the rigid lid method is obsolete for purposes of realistic ocean climate modelling.

### 2.5.2. Virtual tracer fluxes

As meltwater from glaciers and land ice sheets mixes with the ambient seawater, it impacts on the ocean baroclinic structure by modifying ocean density, with the associated modification in the thickness of density layers remotely transmitted through baroclinic waves (Bryan, 1996; Hsieh and Bryan, 1996; Stammer, 2008). Meltwater also initiates a much faster (roughly 100 times faster) barotropic ocean signal. In the matter of a few days, the barotropic signal communicates around the globe information about a regional change in ocean volume (Lorbacher et al., 2012). Equilibration of this barotropic signal requires weeks, and equilibration of the associated baroclinic signal requires decades.

A virtual tracer flux ocean model does not transfer water across the ocean boundary. Hence, there is no direct barotropic signal in virtual tracer flux models associated with changes to ocean volume (in a Boussinesq model) or mass (in a non-Boussinesq model). For example, the meltwater study of Stammer (2008), which used an ocean model with virtual tracer fluxes, was only able to identify baroclinic, or more precisely steric, aspects of meltwater events, whereas the far more rapid barotropic signals associated with volume changes were ignored (Gower, 2010; Yin et al., 2010b; Lorbacher et al., 2012). It is thus important to recognize this limitation of the virtual salt flux models when assessing the regional impacts of meltwater on sea level.

Another limitation of virtual tracer flux models concerns the absence of a bottom pressure signal in response to a meltwater flux. The addition of salt to an ocean model operationally only impacts the salt equation. It does not affect the continuity equation. Hence, melting land ice, implemented as a virtual salt flux as in Stammer (2008), will not modify bottom pressure in a mass conserving non-Boussinesq model. It will impact bottom pressure in a volume conserving Boussinesq model, but only through changes in density, with such changes a spurious result of the Boussinesq approximation (see Section D.3.3 of Griffies and Greatbatch (2012)). This limitation precludes virtual flux models from being used to study static equilibrium sea level changes associated with ice and water mass redistributions. Studies involving mass changes are of interest for investigating the impact of melting land ice, where changes in both dynamic sea level and static equilibrium sea level can be comparable (Kopp et al., 2010).

A third limitation of virtual tracer flux models arises from the potentially different responses of the overturning circulation to meltwater pulses. As shown by Yin et al. (2010b), virtual salt flux models tend to exaggerate their freshening effect relative to the response seen in real water flux models. As changes to the Atlantic overturning are thought to be important for regional sea level changes (Yin et al., 2009; Lorbacher et al., 2010), it is useful to remove unnecessary assumptions, such as virtual tracer fluxes, when considering model responses to climate change associated with meltwater events.

Virtual tracer fluxes are typically associated with rigid lid models, though some free surface ocean climate models also use virtual tracer fluxes (see Table 1). We do not consider meltwater scenarios in this paper, so the limitations of virtual flux models are of no

direct concern for our analysis. However, the limitations are of concern for realistic coupled climate models that aim to incorporate a wide suite of ocean-related processes impacting sea level (Slangen et al., 2012). It is therefore critical that the analyst understand these limitations.

### 2.5.3. Boussinesq approximation

As noted in Section 2.2, the prognostic sea surface height produced by a volume conserving Boussinesq ocean model does not account for changes in sea level due to global steric effects (Greatbatch, 1994). Furthermore, the mass of seawater in a column of Boussinesq fluid is affected by spurious sources and sinks, since changes in density in a volume conserving fluid are associated with mass changes. Hence, the Boussinesq model requires corrections in order to study impacts on the geoid and earth rotation associated with changing seawater mass distributions (Bryan, 1997; Kopp et al., 2010). Nonetheless, as noted in Section 2.2, there is a broad agreement between the large-scale patterns of dynamic sea level produced in Boussinesq and non-Boussinesq ocean climate simulations (Losch et al., 2004; Griffies and Greatbatch, 2012). Thus, in practice, ocean climate modellers need only be concerned with global corrections to the Boussinesq sea level to account for steric effects on the global mean. Salient details are given in Appendix A. All but two of the ocean models considered in this paper use a volume conserving Boussinesq formulation (Table 1).

### 2.5.4. Conservation of heat and salt

From the ocean climate perspective considered in this paper, the sea level question relates to how and where heat and salt are fluxed across ocean boundaries, and then transported within the ocean, with the associated buoyancy anomalies giving rise to regional and global steric sea level changes. In particular, for global mean sea level, changes arise from the net heat fluxed across the ocean surface. This heat flux is the relatively small residual of large fluxes arising from many heating components such as shortwave, longwave, latent, and sensible. A necessary condition to reliably simulate thermosteric sea level change is that the numerical model conserve heat, locally and globally, preferably at the level of computational roundoff. The same level of precision is needed for salt in order to properly capture halosteric sea level changes, particularly those contributing to regional patterns (Durack et al., 2012; Church et al., 2013a).

The conservative evolution of ocean heat or salt means that heat and salt both satisfy a conservation law whereby their evolution within a region is impacted only through fluxes crossing region boundaries. It does not mean that the property (i.e., heat or salt) remains constant in time within the region. So when examining the heat conservation properties of the CORE-II ocean models in Appendix C, we examine whether the total heat within the global ocean model evolves according to the heat flux crossing the ocean boundaries. If we need to invoke a significant internal source or sink to explain the heat budget, then we conclude that the model is not conservative. These comments are relevant also for studies of sea level, heat content, and salt content using ocean data assimilated models or state estimates, such as those described by Storto et al. (2014), Hernandez et al. (2014), Palmer et al. (2014) and Alves et al. (2014). Methods used in the state estimation of Wunsch et al. (2007) and Wunsch and Heimbach (2014) ensure that the ocean tracers maintain a physically appropriate conservation equation (see Wunsch and Heimbach, 2013 for a review). Other methods commonly associated with prediction systems (see Schiller et al., 2013 for a review) employ internal sources and sinks that in turn compromise their utility for sea level studies.

One of the models used in the present study is not conservative (Table 1). This model, HYCOM, has been shown to exhibit similar non-conservation behaviour when coupled to an atmospheric

model for purposes of studying global climate (Megann et al., 2010). However, there is a new version of HYCOM that in fact conserves heat and salt, to within computational roundoff (Rainer Bleck and Shan Sun, personal communication 2013). A suitable CORE-II simulation using this updated code was not available in time for inclusion in the present study.

## 2.6. Global mean SST in the CORE-II simulations

Fig. 2 shows the time series for global mean sea surface temperature (SST) from the simulations over the fifth CORE-II cycle. Time series for the models reach a cyclo-stationary state, so that each of the five CORE-II cycles show nearly the same temporal behaviour of SST for the respective models. It is striking how well the various models agree in their SST evolution, with interannual fluctuations aligned across the models. This result follows from the large

impact on SST from the common CORE-II atmospheric state of Large and Yeager (2009).

### 2.6.1. Discrepancy between observed SST and CORE-II simulated SST

The CORE-II simulations exhibit a slight jump in SST around 1980 associated with the climate regime shift (discussed in Trenberth and Hurrell, 1994 and Meehl et al., 2009), after which time they transition to a higher SST and then fluctuate around this higher decadal mean value until 2007. This transition is present in the 10 m air temperature based on the NCEP reanalysis (Kalnay et al., 1996) used in the CORE-II atmospheric state (third panel of Fig. 2). The global mean SST in all CORE-II simulations is roughly 0.1–0.2°C warmer at the end of 2007 than the start of 1948.

The transition from 2007 back to 1948 presents an unphysical periodic element to the CORE-II simulations. The amplitude of the transition, in the global mean, is about 0.1–0.2°C, corresponding to the rise in SST over the 60 years of the cycle. Even if the CORE-II atmospheric state of Large and Yeager (2009) was a perfect rendering of the real atmosphere, the periodicity 1948 → 2007 → 1948 → etc. introduces a lag to the ocean response to low frequency variability, with the lag time directly related to the time scale for the ocean to equilibrate. We thus expect that the CORE-II simulations of global mean sea level will lag behind observation-based sea level estimates.

A notable feature seen in the third panel of Fig. 2 is the difference between the amount that SST increases in the CORE-II simulations relative to that found in the observation-based analysis of Hurrell et al. (2008). Although there is a positive correlation between interannual SST fluctuations, the CORE-II ensemble mean SST is roughly 0.1–0.2°C warmer at the end of 2007 than the start of 1948, whereas the Hurrell et al. (2008) SST is roughly 0.4°C warmer over the same period. There is a notable absence in the CORE-II simulations of a positive SST trend post-1980, even though there is a trend in the air temperature in the CORE-II forcing (Fig. 2). We note that the SST trends in the Hurrell et al. (2008) analysis is sensitive to the assumptions made about sea ice. For the time series shown here, we do not mask regions under sea ice, which accords with the approach used for the models.

### 2.6.2. SST evolution in the NCAR CORE-II simulation

A thorough exploration of the SST evolution is beyond our scope. Nonetheless, we expose some details from the NCAR CORE-II simulation to more fully describe the behaviour during the period post-1984 (where satellite information is more complete for the CORE atmospheric state), and to illustrate the difficulty uncovering cause and effect. To furthermore remove questions about sea ice impacts on surface fluxes, we consider only the region between 40°S and 40°N.

The air temperature in the CORE-II atmospheric state post-1984 increases in response to the increase in SST used as part of the NCEP reanalysis. The air temperature rise leads to a reduction in sensible cooling of the ocean in the NCAR CORE-II simulation by roughly  $1 \text{ W m}^{-2}$  (i.e., an increase in ocean heating). The air humidity also rises by about  $0.2 \text{ g kg}^{-1}$ . For a constant SST and surface humidity, the rise in air humidity leads to a decrease in evaporation and thus a further increase in ocean heat flux by about  $2.5 \text{ W m}^{-2}$ . The combined sensible and latent change of more than  $3 \text{ W m}^{-2}$  is balanced by a decrease in the ISCCP-FD satellite downwelling longwave heating by about the same amount (Large and Yeager, 2012). The net heat flux into the ocean is therefore near  $0 \text{ W m}^{-2}$ , which is reflected in the approximately constant SST in the NCAR CORE-II simulation after 1984 (Fig. 2). This near-zero net heat flux is also consistent with the five-cycle spin-up nearly achieving a steady state for the NCAR CORE-II simulation (see Fig. 3 discussed in Section 3.1).

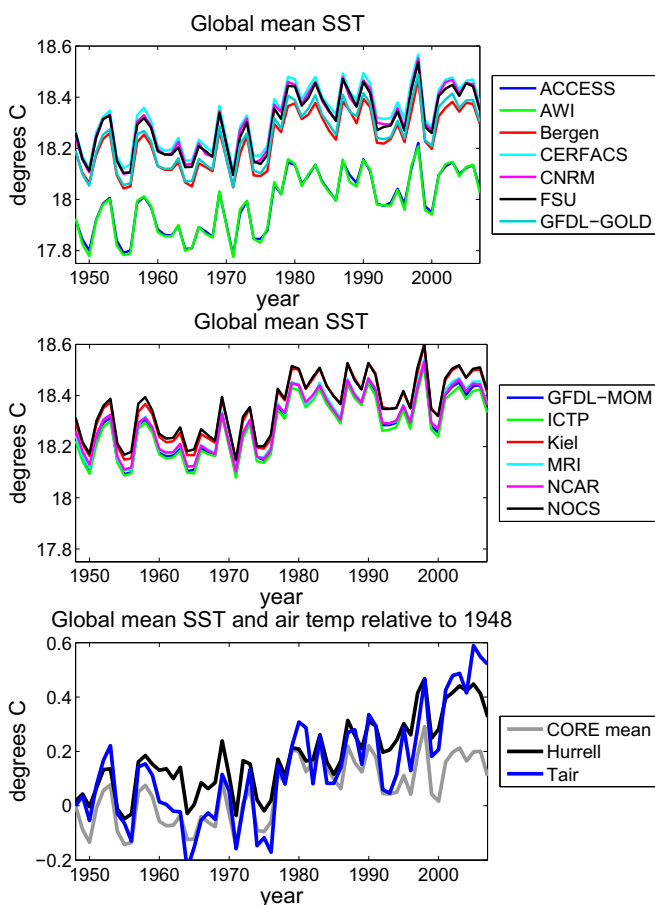


**Fig. 2.** Time series for global area mean sea surface temperature (SST) for the fifth CORE cycle. Time series for all of the models rapidly reach a cyclo-stationary state, so that global mean SST is nearly the same for each of the five cycles. We do not know why ACCESS and AWI-FESOM show a consistently low offset from the other models. All models show a transition centred around 1975 to higher values extending to the end of the simulation, with this transition associated with the climate regime shift discussed in Trenberth and Hurrell (1994) and Meehl et al. (2009). Throughout the 60 years shown, there is a strong correlation between interannual SST fluctuations in the CORE-II simulations and the Hurrell et al. (2008) observation-based analysis (third panel). However, all models show about half the magnitude of the upward long-term SST trend relative to Hurrell et al. (2008), as revealed by the third panel that shows the CORE-II ensemble mean, air temperature used for the CORE-atmosphere, and the Hurrell et al. (2008) analysis, relative to their respective values at 1948. Whereas the CORE-II ensemble mean is roughly 0.1–0.2°C warmer at the end of 2007 than the start of 1948, the Hurrell et al. (2008) analysis is roughly 0.4°C warmer over the same period. There is a notable absence in the CORE-II simulations of a positive SST trend after 1980, which contrasts to the air temperature and the SST analysis from Hurrell et al. (2008).

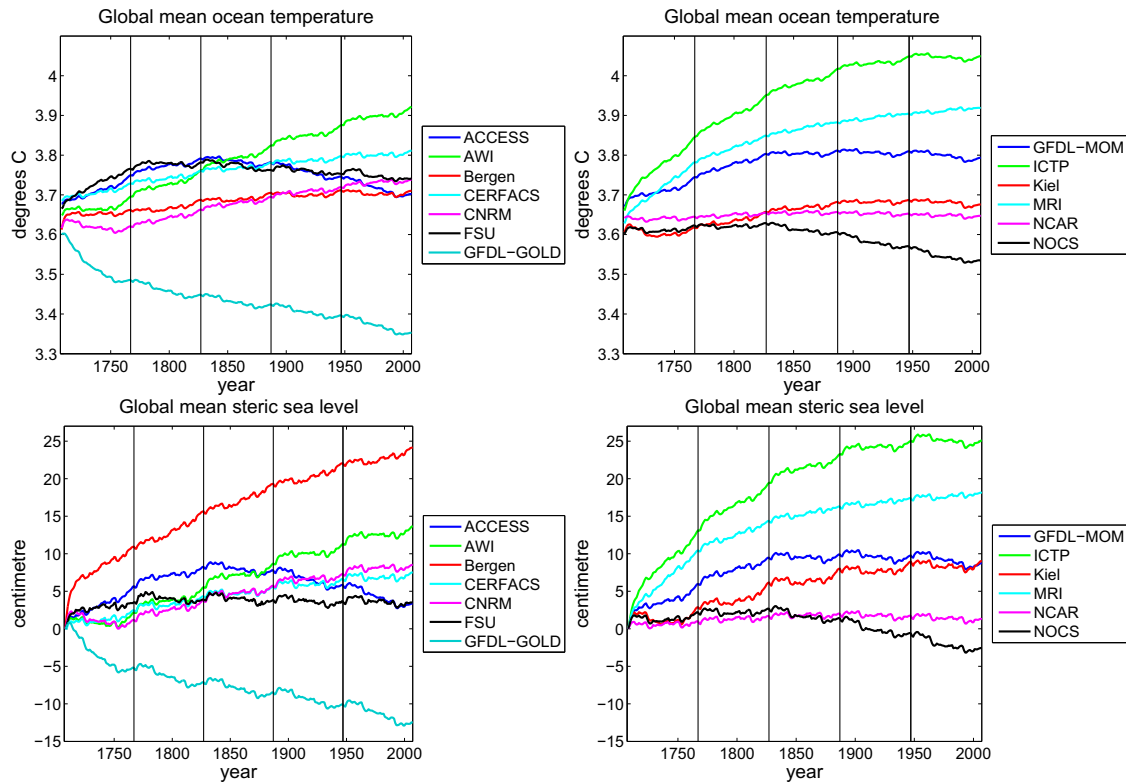


**Fig. 3.** Time series for global volume mean annual ocean temperature and global mean annual steric sea level as computed in the interannual CORE-II simulations. Each panel illustrates drift in the various models over the five CORE-II cycles. Note the nominal start year of 1708 allows for a continuous increase in time over the 300 years of the five-times repeated cycles of the interannual CORE-II atmospheric state (years 1948–2007). The vertical lines denote the start of a new CORE-II cycle. The global mean sea level arising from global steric effects is computed according to Eq. (29). The diagnostic global mean steric sea level for each model is separately initialized at zero in order to emphasize trends in the respective simulations. Note the close correspondence between the global mean steric sea level and the global volume mean temperature (see Section A.5). The Bergen model is an exception, in which global steric sea level rises much more than global volume mean temperature. The steric sea level rises in this model largely due to a decrease in global volume mean salinity, where the salinity decrease is associated with the lack of zero normalization of the surface restoring salt-flux.

We now consider the case of fluxes computed based on the CORE-II atmospheric state and the observation-based SST of Hurrell et al. (2008). In this “observed” case, the rising SST warms and moistens the atmosphere as for the NCAR CORE-II simulation. However, the resultant increase in the surface air temperature is less than the rise in SST (see Fig. 10 from Bates et al. (2012)). Because the rising SST outpaces the increase in surface air temperature between 1984 and 2007, both the latent and sensible heat fluxes become more negative (i.e. cooling the ocean) by  $-5.3 \text{ W m}^{-2}$  and  $-1 \text{ W m}^{-2}$ , respectively. The only mechanisms that could allow for SST to increase in the presence of cooling air-sea fluxes is a through warming induced by ocean circulation or mixing. Large and Yeager (2012) infer that a reduction in mixing across the thermocline is likely responsible for the SST rise over this period; i.e., reduction in upwelled cold waters. Such an effect could not continue indefinitely, in which case SST would be expected to stop rising at some point, which indeed it has. This analysis suggests that the CORE-II simulations do not simulate the natural variability in the upper ocean boundary layer that leads to this inferred change in vertical mixing, at least over the years 1984–2007 (Large and Yeager, 2012).

### 2.6.3. Connection to global mean sea level

If the global mean ocean temperature was directly a function of the SST, then we might expect the CORE-II simulations to be biased low in regards to volume mean global ocean heating, as indeed they are (Section 3). However, there are many other factors that impact on volume mean ocean heat, including model drift, sea ice effects, and long-term adjustment to surface heating. It is therefore not generally possible to infer that volume mean global ocean heat changes will be lower than observations just because SST

increases less than observations in the CORE-II simulations. So although we find the CORE-II simulations to be generally biased low in their volume mean ocean heat trends, a deductive story explaining this low-bias is available only after far more analysis than presented in this paper. We note that any such analysis is associated with far more observational uncertainty than associated with an analysis of SST evolution.

### 2.7. Restricting our analysis to the 15 years 1993–2007

The study from Doney et al. (2007) considered four cycles of 40-year simulations using an earlier version of the Large and Yeager (2009) atmospheric state. They compared SST patterns to the observation-based estimates from Reynolds et al. (2002), and found good agreement between model and observations for the first two empirical orthogonal functions. The agreement between modelled and observed patterns of variability is consistent with the close correlation between interannual fluctuations in the global mean SST shown in Fig. 2. However, it does not imply that the lower frequency trends match, as indeed they do not.

The study of Large and Yeager (2012) considered many features of ocean surface fluxes that impact on the SST within the context of the CORE-II atmospheric state of Large and Yeager (2009), using the SST from Hurrell et al. (2008) to generate these fluxes. Differences in ocean surface fluxes in the Large and Yeager (2012) study relative to the CORE-II simulations arise from differences in the simulated SSTs. As with Doney et al. (2007), the papers from Large and Yeager (2009) and Large and Yeager (2012) emphasize that the CORE-II atmospheric state is suited mostly for studies of interannual variability, rather than longer term multi-decadal

trends such as that associated with anthropogenic warming. Our focus on 15 year trends pushes the envelope over which the atmospheric state is of use.

Doney et al. (2007) and Large and Yeager (2012) identify many reasons to focus analyses on the latter portion of the CORE-II simulations. A notable reason is that it is not until 1984 that satellite information is used for radiation, with climatology used in earlier years. As discussed in Large and Yeager (2012), there is a nontrivial “shock” to the atmospheric state (and hence to ocean boundary heat fluxes) associated with introducing the satellite radiation, mostly arising from changes to the downward long wave radiation. There is additional motivation to focus analysis on years 1993–2007, since we can make use of satellite sea level measures to directly compare against the CORE-II simulations (e.g., Figs. 15–17).

Based on these considerations, we consider the four early CORE cycles, as well as the years prior to 1993 in the fifth cycle, as part of a spin-up phase. We discuss aspects of this spin-up in Section 3 to expose elements of long-term model drift. Yet we focus analysis on the final 15 years of the fifth CORE cycle throughout the bulk of this paper, with this period the only one that we directly compare to observation-based analyses. This period is relatively short, meaning that a great deal of the simulated trends in sea level and ocean heat content arise from natural variability (e.g., Zhang and Church, 2012) rather than longer-term anthropogenic effects. Our comparison between CORE-II simulations and observation-based analyses, especially of subsurface ocean properties, can be viewed as a common evaluation of two imperfect measures of the recent ocean.

### 2.8. CORE-II ensemble means & comparison to observation-based analyses

For many results presented in this paper, we compute differences between simulations and observation-based analyses. Additionally, we find it very useful to compute an ensemble mean of the CORE-II simulations. For both purposes, we first map the simulation results to a common spherical coordinate grid, and if necessary to a common vertical grid.<sup>2</sup> Quantitative model-model and model-observation comparisons are performed with all results on the common grid. The CORE-II ensemble mean is also computed on this common grid, with equal weighting to all models. We make use of the CORE-II mean especially for the summary discussion in Section 6.

We use of the following observation-based analyses to compare against the CORE-II simulations.

- We already encountered the HadSST3 sea surface temperature analysis in Fig. 2. We make use of an updated version of that described by Kennedy et al. (2011) and available from the web site <http://www.metoffice.gov.uk/hadobs/hadsst3/>.
- The analysis of Levitus et al. (2012) provides estimates for the upper 700 m ocean heat content and associated thermosteric sea level. This analysis is used as part of Figs. 8, 13, 14, and 26. Note that heat content trends require the conversion of *in situ* temperature to potential temperature. For this purpose, we used the World Ocean Atlas climatological salinity (Antonov et al., 2010) and *in situ* temperature (Locarnini et al., 2010) (both relative to 1957–1990), and the anomalous *in situ* temperature, and used these fields to compute the trend in potential temperature.
- We make use of an updated version of the analysis of Domingues et al. (2008) and Church et al. (2010), again for use in the upper 700 m ocean heat content and associated thermosteric sea level found in Figs. 8, 13, 14, and 26.

- The Durack and Wijffels (2010) analysis extends over the upper 2000 m of the ocean. This analysis is based on profiles containing both temperature and salinity. This approach has the advantage that no corrections are necessary to remove instrumental biases in XBTs or MBTs discussed in Wijffels et al. (2008). However, the total number of profiles used by Durack and Wijffels (2010) is well under one-half of those used in the Levitus et al. (2012) analyses.

We make use of an updated version of the Durack and Wijffels (2010) analysis of temperature changes, with results presented in Fig. 13 for the upper 700 m heat content change, and Fig. 14 for the upper 2000 m zonal temperature change. We also use their analysis for upper 700 m steric, thermosteric, and halosteric trends shown in Figs. 25–27. As part of the updated analysis, we did not filter interannual signals associated with El Niño Southern Oscillation. Eliminating this filter, which is used in the original Durack and Wijffels (2010) analysis, allows for the updated analysis to be directly comparable to the CORE-II simulations and to the other observation-based analyses.

- In Figs. 15–17, we make use of the dynamic sea level available from the gridded satellite altimeter product from the AVISO project (Archiving, Validation, and Interpolation of Satellite Oceanographic Data) (Le Traon et al., 1998; Ducet et al., 2000). The particular version of this product was taken from NASA’s Jet Propulsion Laboratory on the web site

[podaac.jpl.nasa.gov/dataset/AVISO.L4.DYN.TOPO.1DEG.1MO](http://podaac.jpl.nasa.gov/dataset/AVISO.L4.DYN.TOPO.1DEG.1MO).

- In Section 3.5, we discuss further observation-based analysis products and some of the caveats regarding their use.

## 3. Steric impacts on global mean sea level

The CORE protocol (Griffies et al., 2009b and Danabasoglu et al., 2014) introduces a negligible change to the liquid ocean mass (non-Boussinesq) or volume (Boussinesq), and the salt remains nearly constant (except for relatively small exchanges associated with sea ice changes). For simulations with zero net water crossing the ocean surface and constant salt content, changes to the simulated global mean sea level arise predominantly through the global mean of thermosteric effects. That is, global mean sea level will change due to changes in ocean heat content and redistribution of heat.

Not all models considered in the present study strictly adhered to the CORE protocol (see full details in Danabasoglu et al., 2014), in that their water content and/or salt content changed during the simulation far more than just via exchange with sea ice. Nonetheless, for all models except one (see Fig. 3), we find that changes in global mean steric sea level are dominated by changes in global mean ocean temperature. Halosteric effects generally become important when considering patterns of sea level, either in the horizontal (Section 5) or vertical (Section 3.4). We are, unfortunately, unconvinced that details of the halosteric patterns are physically robust since the CORE-II simulations use surface salinity relaxation, which has no counterpart in the real climate system (see Section 3 of Griffies et al., 2009b). This caveat must remain part of interpreting the impacts of salinity on regional sea level in the CORE-II simulations (Section 5).

We gave many reasons in Section 2 to focus our assessment on years 1993–2007. Nonetheless, it is of interest to expose some of the longer term features of the simulations, and we do so in this section. This presentation serves to illustrate the different drift properties of the simulations, and allows us to ask general questions about heat and salt conservation (Appendix C.2). It also provides further motivation to limit our analysis to 1993–2007. Quite

<sup>2</sup> We performed this remapping using tools available within the NOAA/PMEL Ferret free-software package.

simply, a comparison of global mean behaviour in the CORE-II over longer time scales is fraught with huge difficulties and caveats.

### 3.1. Global mean ocean temperature and sea level: the five CORE-II cycles

Fig. 3 exhibits time series of global mean ocean temperature and global steric sea level from the suite of CORE-II simulations. Although aiming to initialize the models using the same analysis from Steele et al. (2001), the initial global mean ocean temperature in fact slightly differs for the various models. We conjecture that the differences are associated with details for how the models interpolate from the Steele et al. (2001) grid to the model grid, with differences in model topography also impacting the initial global mean values.

It is useful to contrast the drift in global mean ocean temperature shown in Fig. 3 with that of the relatively stable global mean SST in Fig. 2. Again, SST in the CORE-II simulations is largely constrained by the prescribed CORE-II atmospheric state of Large and Yeager (2009). In contrast, global mean ocean temperature and sea level are a function of the global mean surface fluxes, which are in turn a function of the simulated SST, ocean surface currents, and sea ice cover. Each model differs in numerical formulations, physical parameterizations, and/or grid resolution, each of which contributes to differences in simulation features, particularly when considering multi-decadal and longer simulations. We therefore expect the models to exhibit differing drifts over the course of the five CORE-II cycles.

For all but two models, the simulated global mean ocean temperature increases. Rising global mean temperatures may be expected, since the observational record from 1961–2008 shows an ocean warming trend (Church et al., 2011). However, this expectation must be qualified by noting that the ocean initial conditions from Steele et al. (2001) do not correspond to those at 1960. The models that exhibit a small trend include NCAR, in which case there is a negligible overall trend for the full 300 years. Those models with negligible global mean temperature drift are in close balance with the atmospheric state, so that the global mean heat flux crossing the ocean boundary is nearly zero. The GFDL-GOLD simulation is an outlier as it has a negative trend throughout the five cycles. The negative temperature trend in this model is largely associated with abyssal and deep cooling, much of which originates from the Southern Hemisphere and spreads throughout the deep ocean (not shown).

Along with global volume mean ocean temperature, we also show in Fig. 3 the anomalous global mean sea level as determined by global steric effects. This *steric sea level* is computed according to Eq. (29) discussed in Appendix A.3. The time series is initialized at the first year of the first cycle to have zero anomaly, thus allowing for a direct comparison of the relative change in global steric sea level between simulations in the model suite over the course of the five cycles. As expected based on the discussion in Appendix A.5, the global mean sea level changes associated with steric effects largely follow the behaviour in global volume mean temperature.

### 3.2. Global mean salinity and sea level: details of surface salinity restoring

In Fig. 3, we see that the Bergen simulation exhibits a global mean steric sea level that rises far more relative to the global mean temperature. This behaviour is distinct from the other models, in which the global mean steric sea level parallels global volume mean temperature. For the Bergen model, global mean steric sea level rises due to a nontrivial decrease in global mean salinity. This global mean salinity decrease arises from the absence of a global

adjustment to zero of the net salt crossing the ocean associated with the surface restoring salt flux.

Details of the salt flux adjustment, or “normalization”, are discussed in Appendix B.3 of Griffies et al. (2009b) and Appendix C in Danabasoglu et al. (2014). In effect, the adjustment ensures there is no net salt added to or removed from the ocean-sea ice system associated with the restoring. We note that some models convert the surface salinity restoring into an implied surface freshwater flux. In this case, an adjustment must be made to ensure there is no net water added to or subtracted from the ocean-sea ice system as a result of the restoring. As the surface restoring has no physical counterpart in the real climate system, there is nothing more or less physical about choosing to use a restoring salt flux or restoring water flux.

Returning to the Bergen simulation, we see that without an adjustment to zero of the net surface salt flux, the global mean steric sea level has a significant contribution from the halosteric effect due to drift in ocean salt content. In contrast, all other CORE-II models are dominated by the global thermosteric effect. This result emphasizes the need for models to adjust their restoring salt flux (or restoring water flux) to be zero globally in order to avoid a potentially nontrivial drift in global mean sea level.

### 3.3. The fifth CORE-II cycle and years 1993–2007

Drift in deep ocean temperature plays a role in the temperature and steric sea level trends seen in Fig. 3. Due to the nature of the CORE-II simulations, we cannot remove drift by subtracting a “control” (see Section 2.1). Instead, we focus on the fifth cycle, where in general (though not universally) the global volume mean temperature drift is smaller than for earlier cycles. For this purpose, we recompute the anomalous global mean sea level over just the fifth cycle (i.e., impose a zero anomaly at the start of the 5th cycle), with this result shown in Fig. 4.

In Fig. 4, we note certain downturns in global mean steric sea level associated with volcanic eruptions in 1963/1964 (Agung); 1982 (El Chichón); and 1991 (Pinatubo), as reflected in the observational estimates from Church et al. (2011). Furthermore, eight of the 13 models have higher global mean sea level at year 2007 relative to 1948. This result is consistent with the observational estimates from Church et al. (2011), in which global mean sea level rises due to ocean warming over the years 1961–2008. However, the CORE-II simulations for this period are biased on the low side relative to observations, and we return to this point in Section 3.5 when discussing upper ocean thermosteric sea level. We noted some reasons for a low bias in Section 2.6.

As a final refinement to our analysis period, we present in the second panel of Fig. 4 the global mean steric sea level anomalies referenced to 1993 in the fifth CORE-II cycle. It is only when focusing on this final 15 years of the simulation that nearly all of the models exhibit a rise in global mean sea level (albeit only a slight rise in some models). We compare to observation-based estimates over this time period when discussing thermosteric sea level in Section 3.5.

### 3.4. Vertical dependence of steric, thermosteric, and halosteric sea level rise

Fig. 5 shows the vertical projection of steric impacts on sea level as a function of time over years 1993–2007; Fig. 6 shows the corresponding thermosteric component; and Fig. 7 shows the halosteric component. These vertical-time patterns are the integrands of equations (56)–(58) discussed in Appendix B.1.

Long term temperature and salinity trends, or drift, become apparent in deeper portions of the water column. Furthermore, the lack of agreement between models in the deep ocean is

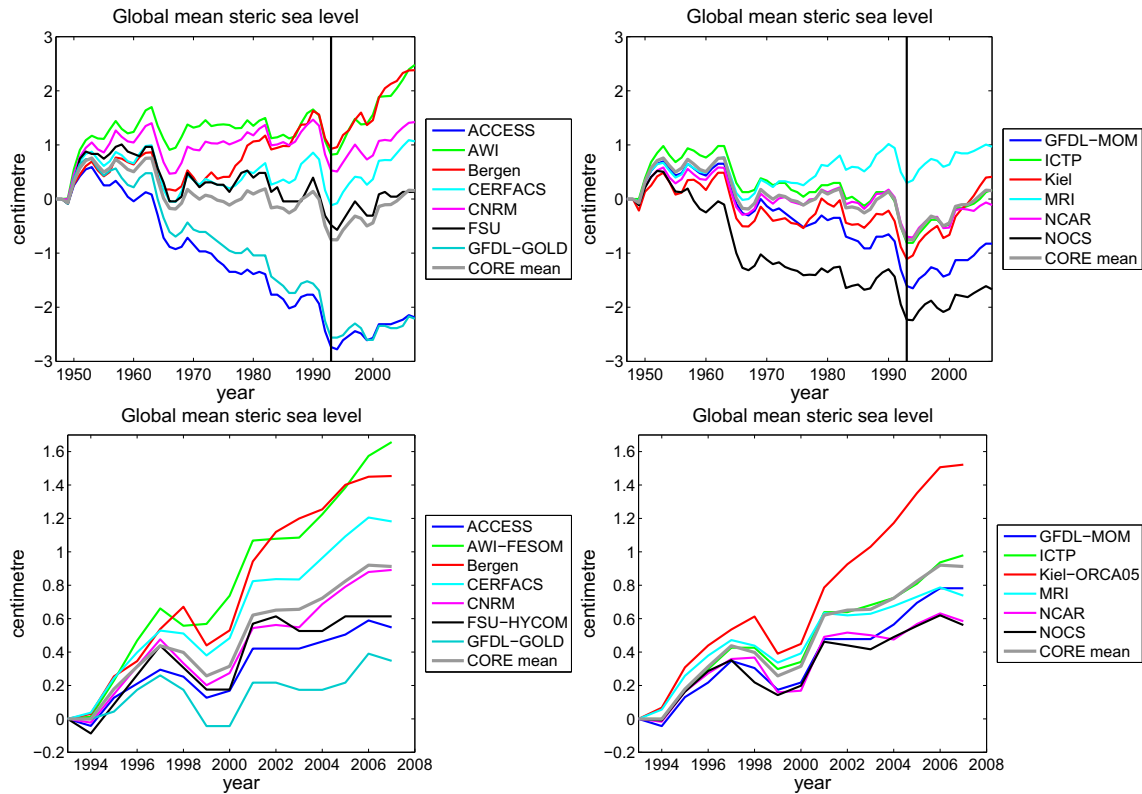


**Fig. 4.** Time series for global mean steric sea level in the fifth cycle of the CORE-II simulations. The first row shows the global mean sea level arising from global steric effects, referenced to the start of the fifth cycle rather than the start of the first cycle (Fig. 3). There are notable downturns in global mean steric sea level associated with volcanic eruptions in 1963/1964 (Agung); 1982 (El Chichón); and 1991 (Pinatubo). Note that many models show a gradual decrease in global mean sea level over the 60 year simulation, until around year 1993 (denoted by a vertical line) at which point most models then show a gradual increase. The second row focuses just on the years 1993–2007 for the fifth CORE-II cycle in order to highlight the increase over the final 15 years, with the global mean now computed relative to 1993. Note the different vertical axis for the two rows. The ensemble mean for the CORE-II simulations over 1993–2007 rises by about 0.8 cm over the 15 years, which is consistent with the observational range for thermosteric sea level of  $15 \text{ yr} \times (0.6 \pm 0.2 \text{ mm yr}^{-1})$  from Church et al. (2011).

indicative of differing drift. We thus focus attention on the upper 700 m, given its lower degree of model drift and significantly better observational sampling (Section 3.5). Contributions to steric sea level change in the upper 700 m are predominantly associated with thermosteric effects, though most models (except Kiel-ORCA05) also show a slightly negative halosteric effect in this depth range. Due to the differing treatment of surface salinity restoring (see Danabasoglu et al., 2014 for details), we are not convinced of the physical reliability of the simulated halosteric patterns seen in Fig. 7. Additionally, we found no systematic connection between surface salinity restoring strength and the behaviour seen in Fig. 7. For the thermosteric patterns shown in Fig. 6, there is a general agreement between the models, though with differing magnitudes. Some of the models show a slight cooling trend centred around 200 m depth, with the ICTP, Kiel-ORCA05, and MRI simulations the most prominent. These cooling trends act to suppress thermosteric sea level rise in the upper 700 m for these three models (see Fig. 8).

### 3.5. Heat content and thermosteric sea level rise

Comparisons to observations must be considered with the appropriate caveats. Uncertainties in thermosteric sea level changes are largest for early years of the historical record (before 1970); below 400 m before the frequent use of deep XBTs in the mid-1990s; below 700 m before the Argo array achieved near-global ocean coverage in 2005; and in the Southern Hemisphere (especially south of 30°S) before Argo (see Fig. 2 in Wijffels et al., 2008 for evolution of the archive of thermal observation

platforms). Current Argo float technology does not allow for full-depth profiling. Hence, we continue to have poor sampling below 2000 m, which means we do not sample roughly 50% of the total ocean volume. Observation-based differences also exist for ocean heat content in the upper 700 m even in historically well-sampled regions, such as the North Atlantic (Gleckler et al., 2012). Although consistent with the rates estimated for the multi-decadal periods, the thermosteric sea level rate for the Argo period (2005–present) is unlikely to represent long-term changes. Over such a short period, long-term changes can be easily obscured by more energetic ocean variability, such as fluctuations in the phase of the El Niño Southern Oscillation (Roemmich and Gilson, 2011).

We consider estimates for observed thermosteric sea level anomalies for the upper 700 m of ocean and within the latitude range 65°S–65°N, as based on recent Argo data as well as historical bottle, CTD and XBT data, the latter with fall-rate corrections from Wijffels et al. (2008). Domingues et al. (2008) determine a trend between the years 1971–2010 of  $0.6 \pm 0.2 \text{ mm yr}^{-1}$ , with this estimate consistent with the more recent Argo data analyzed by Leuliette and Willis (2011). Levitus et al. (2012) provide an estimate of  $0.1 \pm 0.1 \text{ mm yr}^{-1}$  for depths between 700–2000 m. Purkey and Johnson (2010) then estimate a contribution of  $0.1 \pm 0.1 \text{ mm yr}^{-1}$  for abyssal and deep waters in the Southern Ocean. For our purposes, we take an estimated global thermosteric sea level rise to be  $0.8 \pm 0.4 \text{ mm yr}^{-1}$ , which follows that used in Church et al. (2011) and Hanna et al. (2013) for the full depth integrated global steric sea level.

The CORE-II simulations generally show an upper 700 m ocean warming for the 15 years 1993–2007 (Fig. 8). Corresponding to

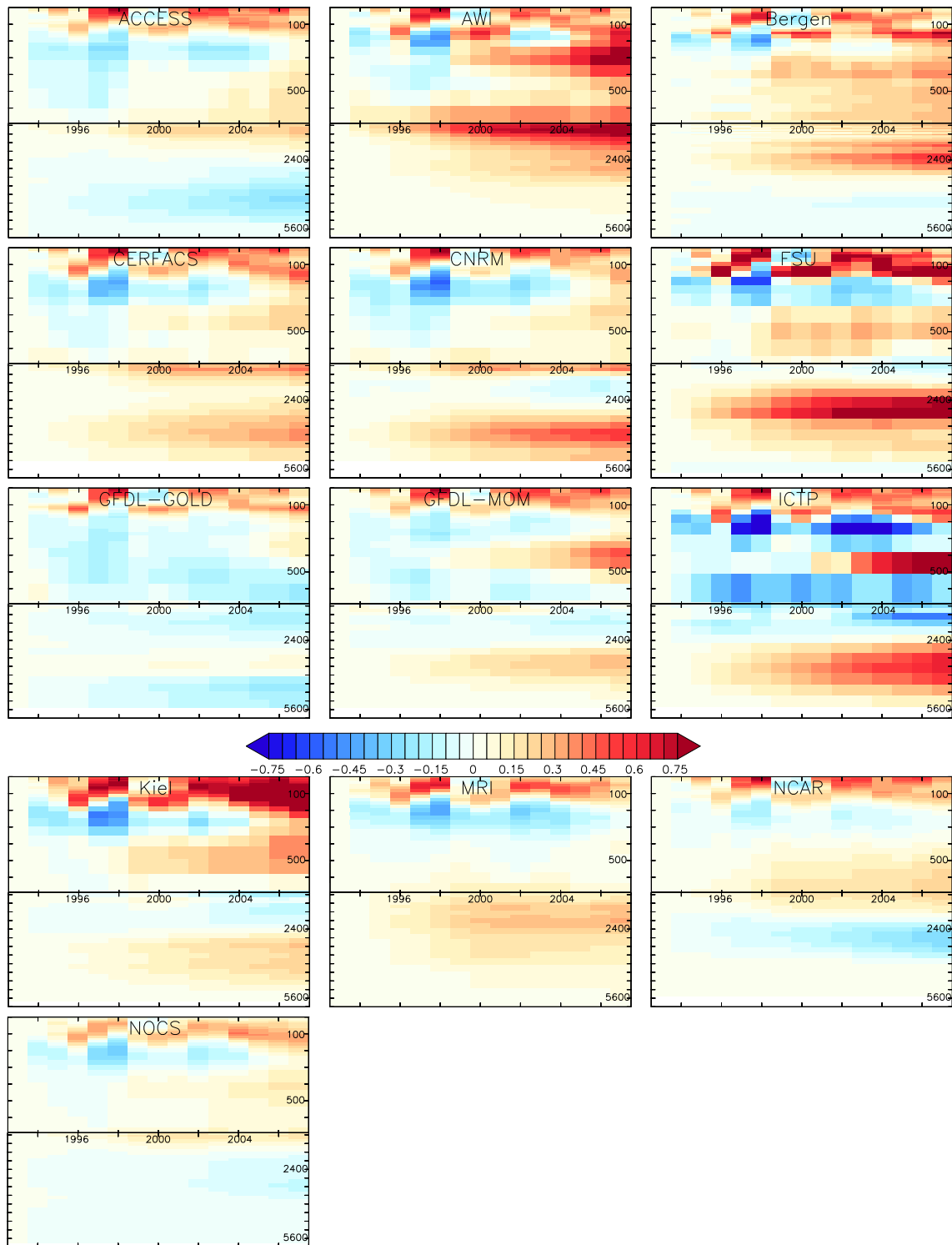


**Fig. 5.** Time series for the horizontally integrated annual mean contributions to steric sea level as a function of depth (in metres), during the years 1993–2007 of the fifth CORE-II cycle. The units are millimetres, and the vertical sum yields the time series for the global mean steric sea level in the second panel of Fig. 4. The upper 700 m is stretched relative to the deeper ocean, thus highlighting the upper ocean trends. The deep ocean portion extends from 700 m to 6000 m. Tick marks in the upper ocean are set 100 m apart, whereas those in the deeper ocean are 800 m apart. The horizontal axis has tick marks every two years from 1993–2007.

the warming is an increasing global steric sea level rise over the same period. A low end to the observational estimates of thermoclinic rise in the upper 700 m suggests a sea level rise of  $0.4 \text{ mm yr}^{-1} \times 15 \text{ yr} = 0.6 \text{ cm}$ , whereas a high end yields  $0.8 \text{ mm yr}^{-1} \times 15 \text{ yr} = 1.2 \text{ cm}$ . Wunsch et al. (2007) reported a

global mean steric sea level rise of roughly  $0.5 \text{ mm yr}^{-1}$  over the years 1993–2004 using a state estimation system.

Estimates of steric sea level from observations consider only thermoclinic effects. This focus arises from the smaller uncertainties in temperature measurements than salinity. It is

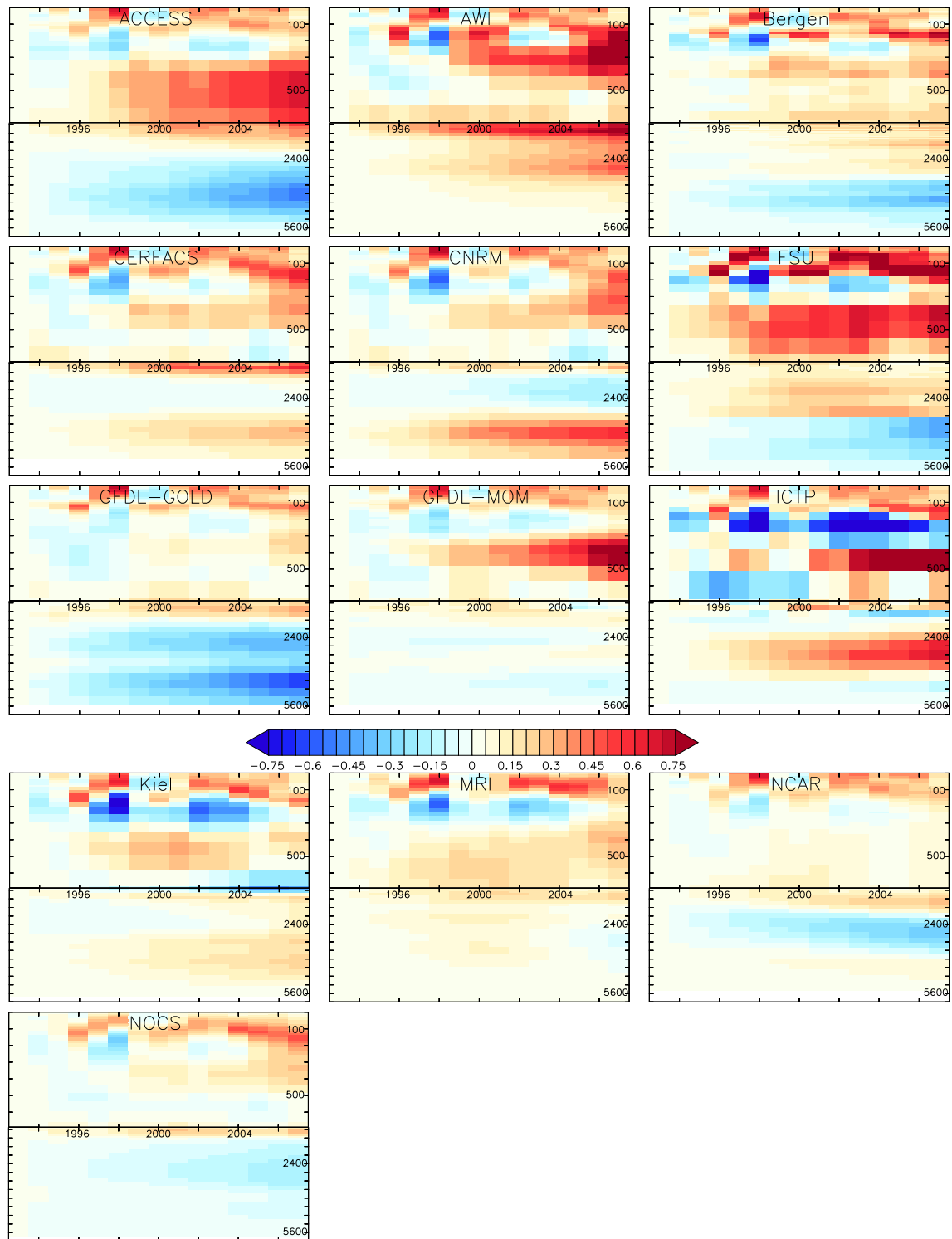


**Fig. 6.** Time series for the horizontally integrated annual mean contributions to thermosteric sea level as a function of depth (in metres), during the years 1993–2007 of the fifth CORE-II cycle. The units are millimetres. The vertical sum yields approximately the time series for the global mean steric sea level in the second panel of Fig. 4. The upper 700 m is stretched relative to the deeper ocean, thus highlighting the upper ocean trends. The horizontal axis has tick marks every two years from 1993–2007.

also justified by the generally small contributions to global mean sea level from halosteric effects (see Appendix A.5 and the corresponding Fig. 36). To compare the CORE-II simulations to the observation-based estimates, we display in Fig. 8 the global heat content and global mean thermosteric contribution to simulated sea level from the depth ranges 0–700 m, and Fig. 9 shows the global mean thermosteric sea level from the depth

range 700–2000 m. The deeper thermosteric changes are generally consistent with the slow rise seen in the observational estimates. For the upper ocean, the observational range is reflected by the bulk of the CORE-II simulations for the years 1993 to 2007, though with most simulations exhibiting an upward trend at the lower end of the observation-based trend of 0.6–1.2 cm.

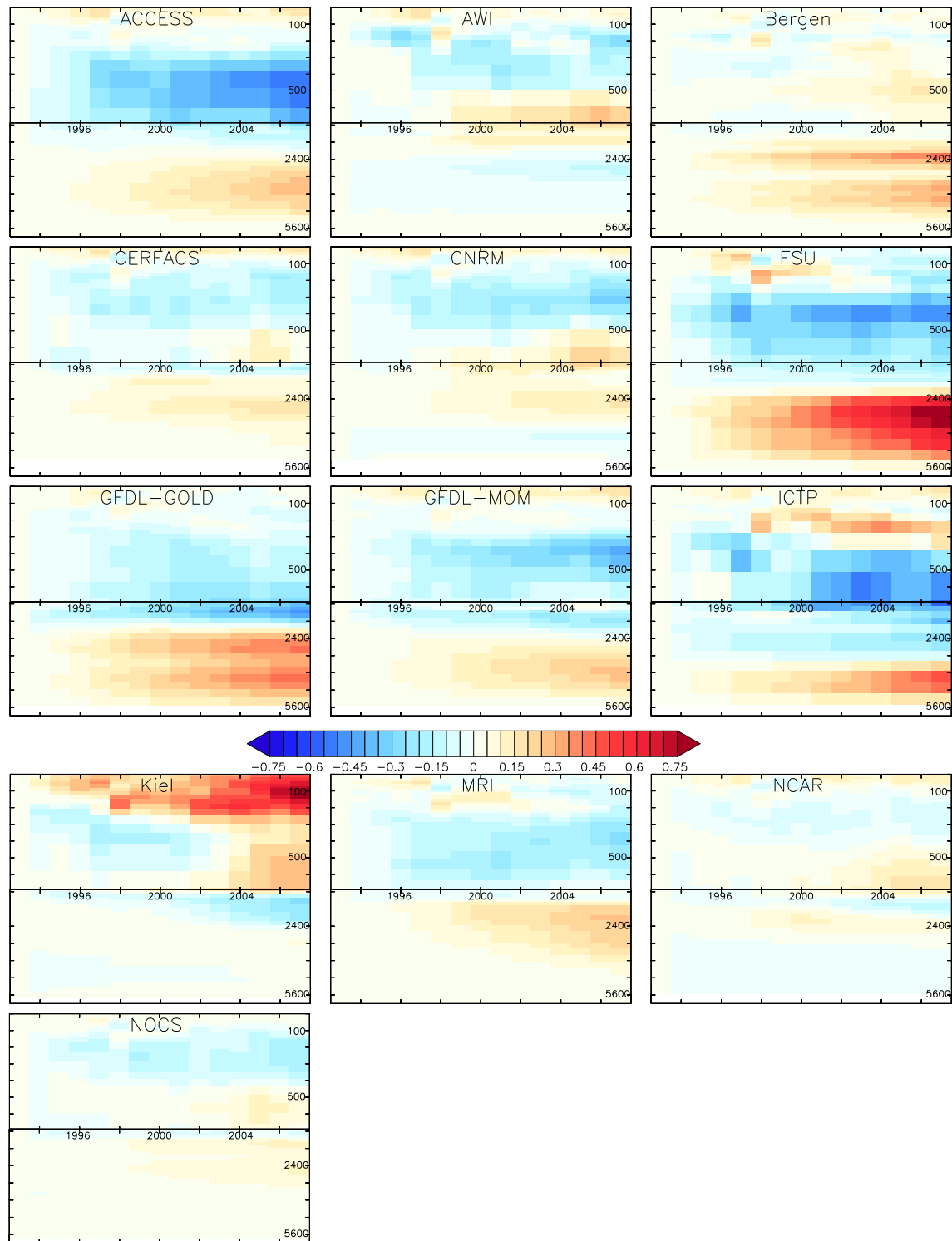


**Fig. 7.** Time series for the horizontally integrated annual mean contributions to halosteric sea level as a function of depth (in metres), during the years 1993–2007 of the fifth CORE-II cycle. The units are in millimetres. The vertical sum is negligible compared to the vertical sum of the thermosteric contributions in Fig. 6, thus indicating the dominance for global mean sea level of the thermosteric effects. However, over certain depth ranges, halosteric effects can be important for some of the models. The upper 700 m is stretched relative to the deeper ocean, thus highlighting the upper ocean trends. The horizontal axis has tick marks every two years from 1993–2007.

#### 4. Temperature and heat content trends for 1993–2007

Global sea level change in the CORE-II simulations is directly correlated to the change in ocean heat content, with the global mean temperature shown in Fig. 3 directly related to the net heat

flux entering the ocean through its boundaries (Eq. (40) in Appendix A.4). We thus find it useful to consider the heat fluxes and ocean heat content and temperature trends seen in the CORE-II simulations. Following the discussion in Sections 2.6 and 2.7, we consider the period 1993–2007 in the fifth CORE-II cycle.

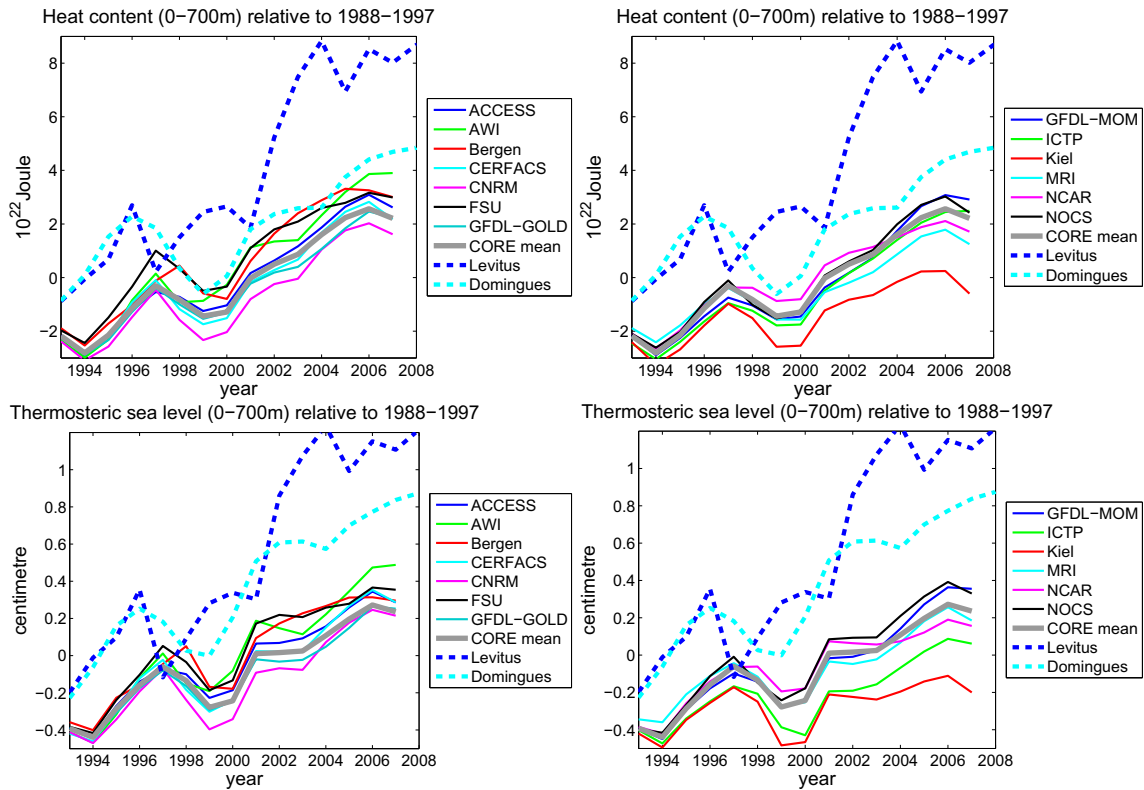


**Fig. 8.** Time series for ocean heat content and thermosteric sea level integrated in the upper 700 m of ocean. To reduce dependence on a single chosen reference date, each result is computed with respect to the ten year mean for the respective model or observational time series, and we chose years 1988–1997. The CORE-II ensemble mean is also shown, as computed from all of the simulations. We also show estimates from observations based on analysis of [Levitus et al. \(2012\)](#) and [Domingues et al. \(2008\)](#). Model results are global, and correspond to the sum from roughly the upper 700 m in the vertical-time plots shown in [Fig. 6](#). Note that if we remove a linear trend, variability in the CORE-II simulations is closer in agreement to [Domingues et al. \(2008\)](#) than [Levitus et al. \(2012\)](#). In Section 2.6, we discuss the slower increase in heating within the CORE-II simulations relative to observations.

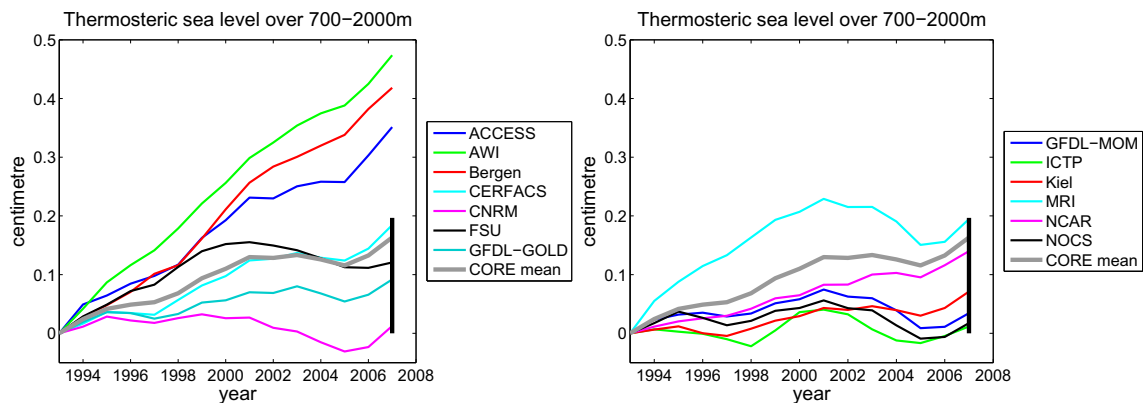


**Fig. 9.** Time series for the thermosteric sea level computed from the depth range 700–2000 m. The CORE-II ensemble mean is shown as computed from all of the simulations. The solid black vertical line at year 2007 represents an estimate of the spread in the observational estimates at the end of the 15 years, computed using a trend of  $0.1 \pm 0.1 \text{ mm yr}^{-1}$  for 700–2000 m (Section 3.5). Each time series is computed relative to the respective model’s steric sea level at 1993.

#### 4.1. Boundary heat fluxes

[Fig. 10](#) shows the time mean boundary heat flux computed over years 1993–2007 for the CORE-II simulations. These patterns include the shortwave, longwave, latent, and sensible heat flux passing across the ocean surface, as well as geothermal heating in those models where it is included ([Table 1](#)). Additionally, the heat flux due to water transport across the ocean surface is included for those models employing a real water flux ([Table 1](#)),

with this heat flux detailed in Section A.4. Finally, there is an adjustment of the heat flux associated with frazil ice formation.

All models exhibit heating in the tropics, which is where global mean sea level is affected the most from surface heating due to the relatively large tropical thermal expansion coefficient ([Fig. 1](#)). All models also show a heat loss in western boundary currents due to the sensible and latent heat loss arising from generally warm waters under a cooler atmosphere. The subpolar North Atlantic is a region where the models generally experience surface heat loss,

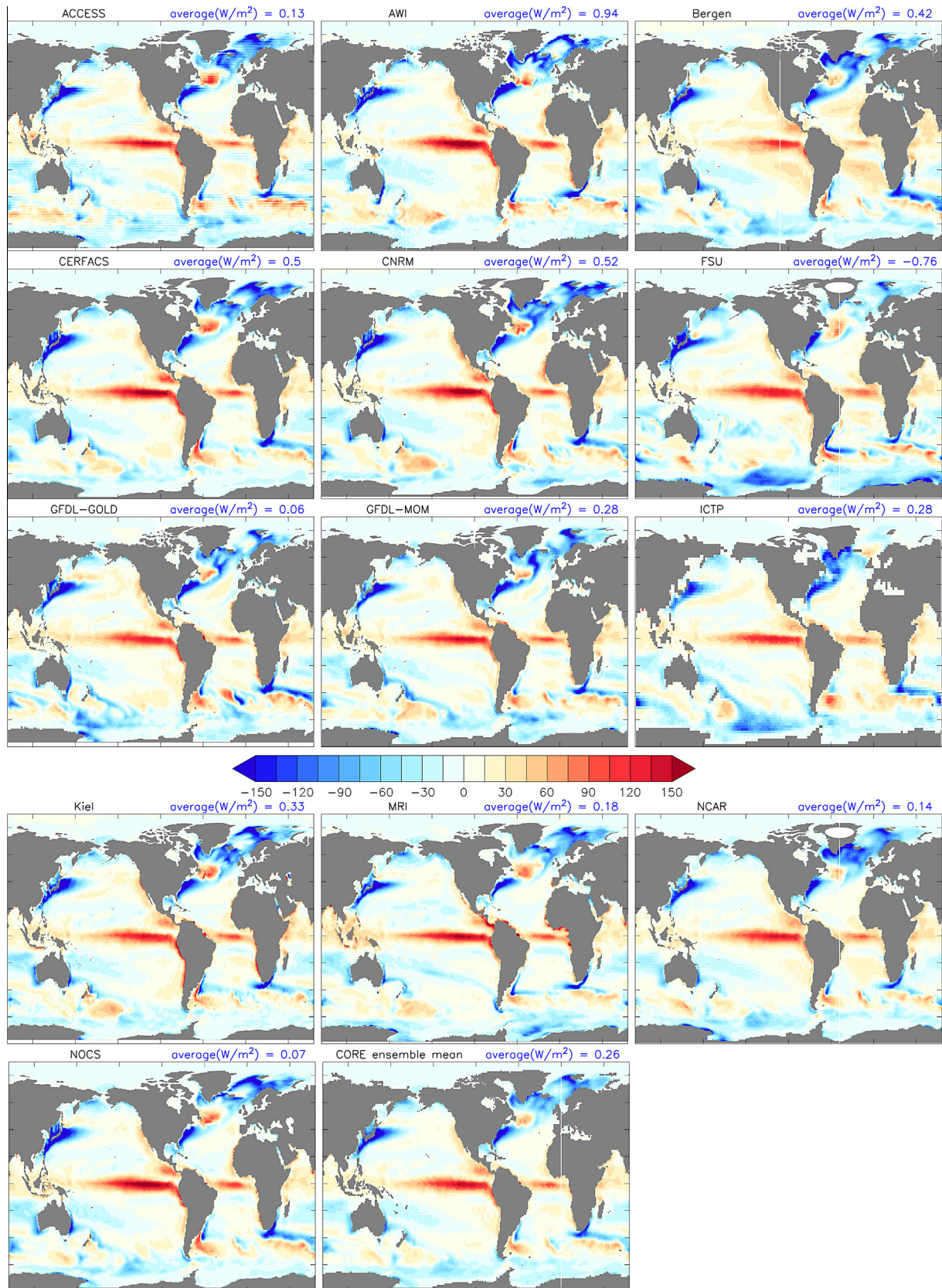


**Fig. 10.** Boundary ocean heat fluxes (units  $\text{W m}^{-2}$ ) for the years 1993–2007 as computed from the fifth CORE-II cycle. A positive number represents heat going into the ocean. The time mean heat flux over this period is indicated on the title to each panel. Also note the simulations from GFDL-GOLD, GFDL-MOM, and ICTP include a geothermal heat flux, with a global ocean mean of  $0.06 \text{ W m}^{-2}$ ; the CERFACS and CNRM simulations include a geothermal heat flux with a global ocean mean of  $0.084 \text{ W m}^{-2}$ . Land masking is set according to the respective model land-sea masks.

though with all models except ICTP exhibiting heat gain near Newfoundland, and with the FSU-HYCOM simulation losing far less surface heat than the other simulations. Deviations between the models largely reflect the paths of the Gulf Stream and North Atlantic Current. Such differences are also reflected in coupled climate models contributing to CMIP (Yin et al., 2010a; Pardaens et al., 2011b; Yin, 2012; Slangen et al., 2012; Bouttes et al., 2013).

The global mean of the ocean boundary heat flux during years 1993–2007 is indicated on each panel of Fig. 10. There are rather large differences in heat flux regionally, particularly in the high latitudes. In general, differences in heat flux illustrate that although the CORE-II simulations use the same atmospheric state, they do not necessarily realize the same heat flux due to differences in simulated ocean and sea ice states. Many models have a net heat flux in the range 0.2–0.6 W m<sup>-2</sup>, though the AWI-FESOM model exhibits a larger heat flux of roughly 1 W m<sup>-2</sup> and GFDL-GOLD and NOCS show a near zero mean boundary heat flux. The FSU-HYCOM simulation shows a negative surface heat flux of roughly -0.7 W m<sup>-2</sup>. However, global mean sea level in the FSU-HYCOM simulation is rising slightly during the period 1993–2007 (see Fig. 4), with the rise due to the spurious numerical heat source on the order of 1 W m<sup>-2</sup> (Appendix C and Table 1).

Fig. 11 shows the time series for the running sum of the global mean annual ocean heat flux for the years 1993–2007. The running sum measures how much heat accumulates within the ocean relative to the start of the integration. All models, except FSU-HYCOM, agree that surface fluxes are adding heat globally to the ocean during the period 1993–2007.

#### 4.2. Ocean heat content trends

Fig. 12 shows the linear trend in full-depth integrated ocean heat content, per unit ocean horizontal area, over the years 1993–2007. We compute this diagnostic according to

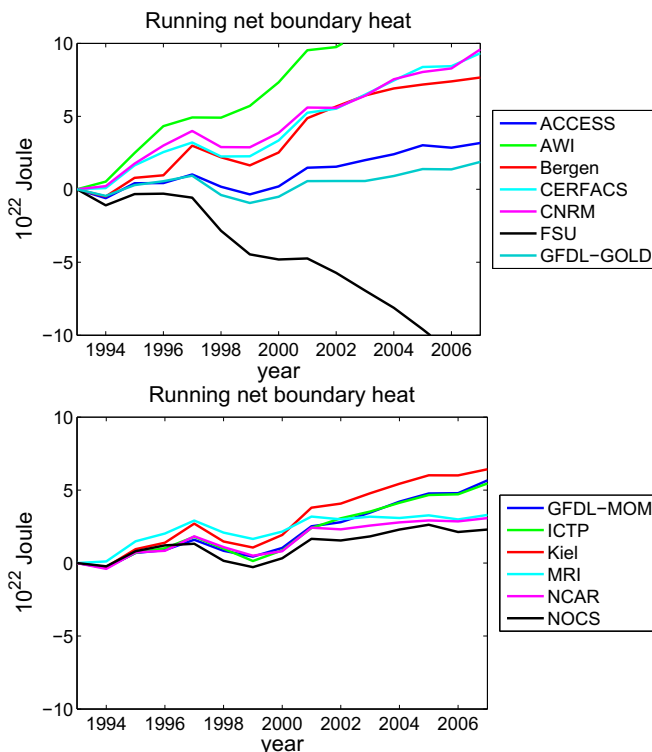


**Fig. 11.** Time series for the running global integrated heat entering the ocean for the CORE-II simulations, relative to 1993 in the fifth CORE-II cycle. Note that all simulations, except that from FSU-HYCOM, exhibit an upward trend in heat accumulation.

$$\frac{\Delta H}{\Delta t} = \rho_o C_p \sum_z \left( \frac{\partial \Theta}{\partial t} \right) dz \quad \text{W m}^{-2}, \quad (11)$$

where the tendency  $\partial \Theta / \partial t$  is approximated by computing the slope of a line fit to the annual mean temperature over the years 1993–2007. Because of the vertical weighting, a relatively small change in the deep ocean temperature can correspond to sizable changes in heat content. We also show the vertically integrated heat content trend, per unit ocean horizontal area, over just the upper 700 m of water in Fig. 13, with this depth range allowing us to compare to three observation-based analyses. Finally, the trend in zonally averaged temperature is shown in Fig. 14, which reveals the vertical and meridional extent of temperature changes. The zonal mean trends reveal that much of the trend in the high latitude occurs below 700 m.

We use three observation-based analyses in Fig. 13 to help expose uncertainties in comparison to the CORE-II simulations, and offer the following comments regarding these three analyses.

- Domingues et al. (2008) and Levitus et al. (2012) generally agree in the low and middle latitudes of all ocean basins, with warming in the west Pacific the dominant pattern of change. Moving southward, the Domingues et al. (2008) analysis shows broad regions of cooling in the northern flank of the Antarctic Circumpolar Current, whereas Levitus et al. (2012) has a much smaller signal. Cooling in the Southern Ocean is seen in the Durack and Wijffels (2010) analysis, reflective of that seen by Domingues et al. (2008) in the Pacific sector but not the Atlantic. We caveat the Southern Ocean observation-based estimates by noting that this is the most sparsely sampled region of the World Ocean.
- In the North Atlantic, Levitus et al. (2012) shows a sizable warming in the subpolar region, and slight cooling to the south along the Gulf Stream region. This warm-north/ cold-south pattern has been analyzed in several studies, such as Häkkinen (2000) and Esselborn and Eden (2001) and recently by Yin and Goddard (2013), with this pattern associated with fluctuations in the Atlantic meridional overturning circulation. We comment more on this pattern in Section 5.5. In contrast to this distinct Atlantic signal in the Levitus et al. (2012) analysis, Domingues et al. (2008) picks up very little signal. Durack and Wijffels (2010) capture a warming in the subpolar North Atlantic, though more confined to the Labrador Sea compared to Levitus et al. (2012), and a weaker cooling than Levitus et al. (2012) within the Gulf Stream region.
- As compared to Domingues et al. (2008) and Levitus et al. (2012), the Durack and Wijffels (2010) analysis exhibits larger warm anomalies in the west Pacific and cold anomalies in the east, with the cold anomalies having an El Niño Southern Oscillation (ENSO) signature largely absent from Domingues et al. (2008) and Levitus et al. (2012). To support this connection to ENSO, we considered a modified analysis based on Durack and Wijffels (2010) that includes a filter to remove the ENSO signal. This filtered pattern (not shown) in fact diminishes the amplitude of the Pacific heating trend in Fig. 13, thus suggesting that ENSO is a key contributor.

In general, the CORE-II ensemble mean shows a low and middle latitude warming roughly consistent, though larger, with the observation-based analyses. Models agree that heat is accumulating in the subpolar North Atlantic, with heat accumulating even in the abyssal regions (Fig. 14). This warming is reflected also in the Levitus et al. (2012) estimate, and to a lesser extent in Durack and Wijffels (2010), yet largely absent from Domingues et al. (2008).

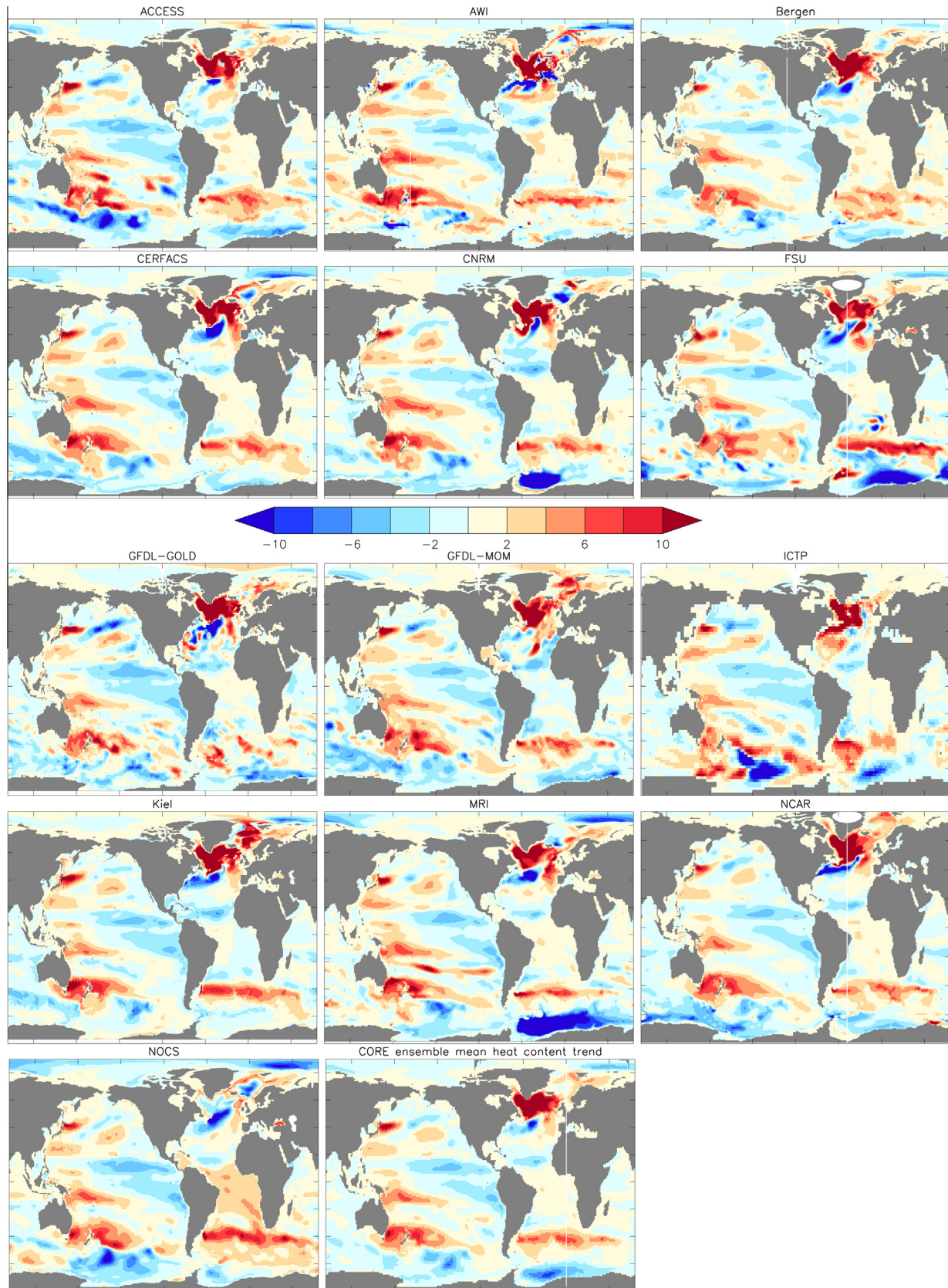


**Fig. 12.** Linear trend in depth integrated annual mean ocean heat content (units  $\text{W m}^{-2}$ ) for the years 1993–2007 as computed from the fifth CORE-II cycle. Note that most models exhibit a relatively strong warming in the subpolar North Atlantic (the NOCS model is a notable exception); a warming in the Kuroshio extension of the Pacific; warming in the mode water regions of the Southern Hemisphere centred around  $40^{\circ}\text{S}$ ; and cooling in the eastern central Pacific. Most models show a negligible trend in both the Arctic Ocean and Indian Ocean. Some show a strong cooling trend in the Weddell Sea and Ross Sea sectors of the Southern Ocean. The colour bar range is chosen to match that shown in Fig. 13 for the upper 700 m heat trends.

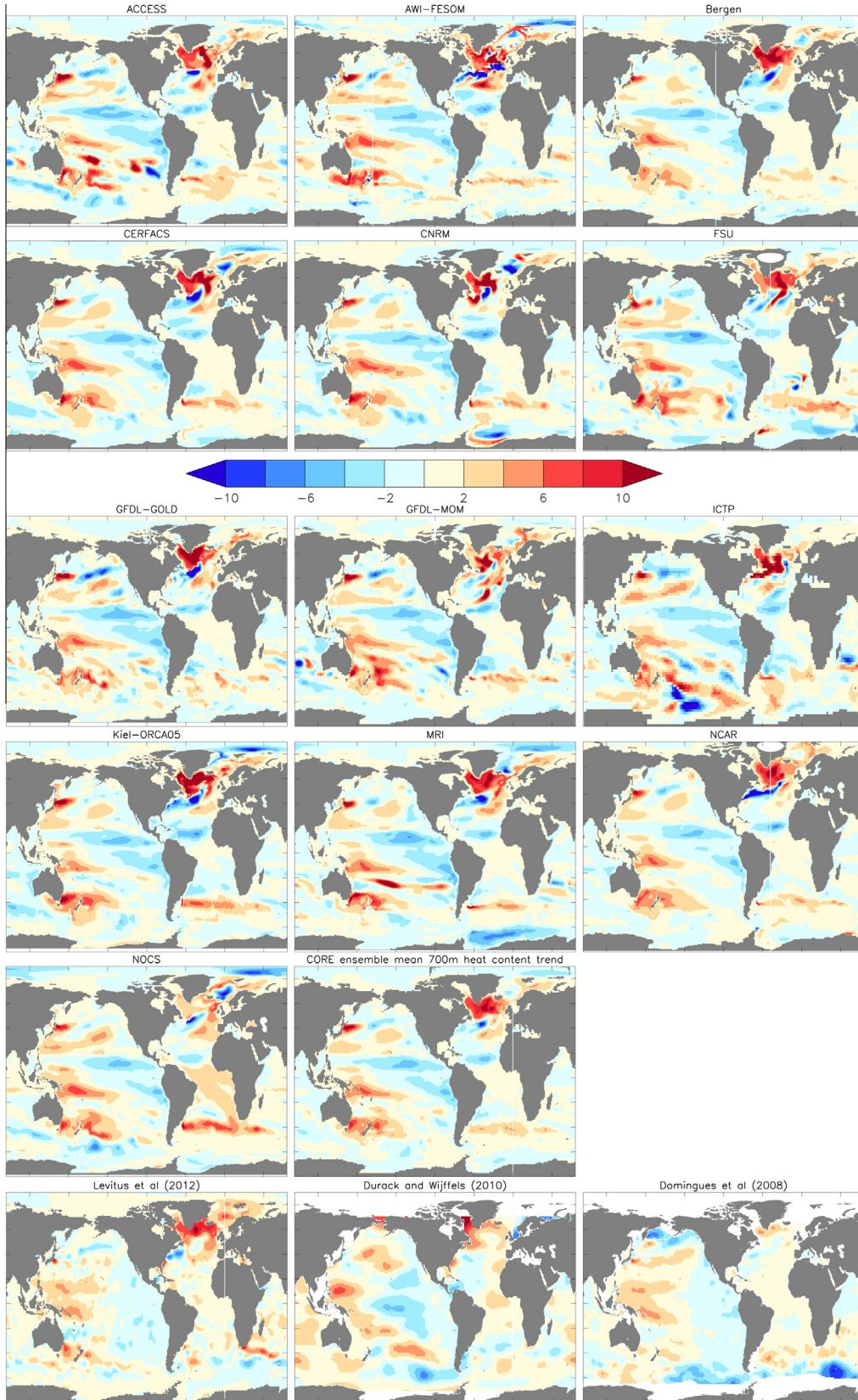


**Fig. 13.** Linear trend in annual mean ocean heat content vertically integrated over the upper 700 m of ocean (units  $\text{W m}^{-2}$ ) for the years 1993–2007, computed from the fifth CORE-II cycle. Also shown is the corresponding trend over years 1993–2007 from [Levitus et al. \(2012\)](#) analysis; an updated analysis from [Domingues et al. \(2008\)](#) and [Church et al. \(2010\)](#) (see their Fig. 6.3b); and the trend over years 1990–2010 using an updated version of the [Durack and Wijffels \(2010\)](#) analysis. Note that much of the high latitude trend seen in [Figs. 12 and 14](#) is missing here, since those trends occur in regions deeper than 700 m. The models also generally show some cooling in the west/central Pacific, with this cooling absent from the observation-based analyses. The spatial correlation between the CORE ensemble mean and the observation-based analyses is given by  $\text{CORE-Levitus} = 0.44$ ,  $\text{CORE-Domingues} = 0.34$ ,  $\text{CORE-Durack} = 0.29$ , where the correlation is computed as  $\text{corr}(A, B) = \frac{\int AB \, dx \, dy}{\left(\int A^2 \, dx \, dy\right)^{1/2} \left(\int B^2 \, dx \, dy\right)^{1/2}}$ , and we ignore regions where the observation-based analyses are missing.

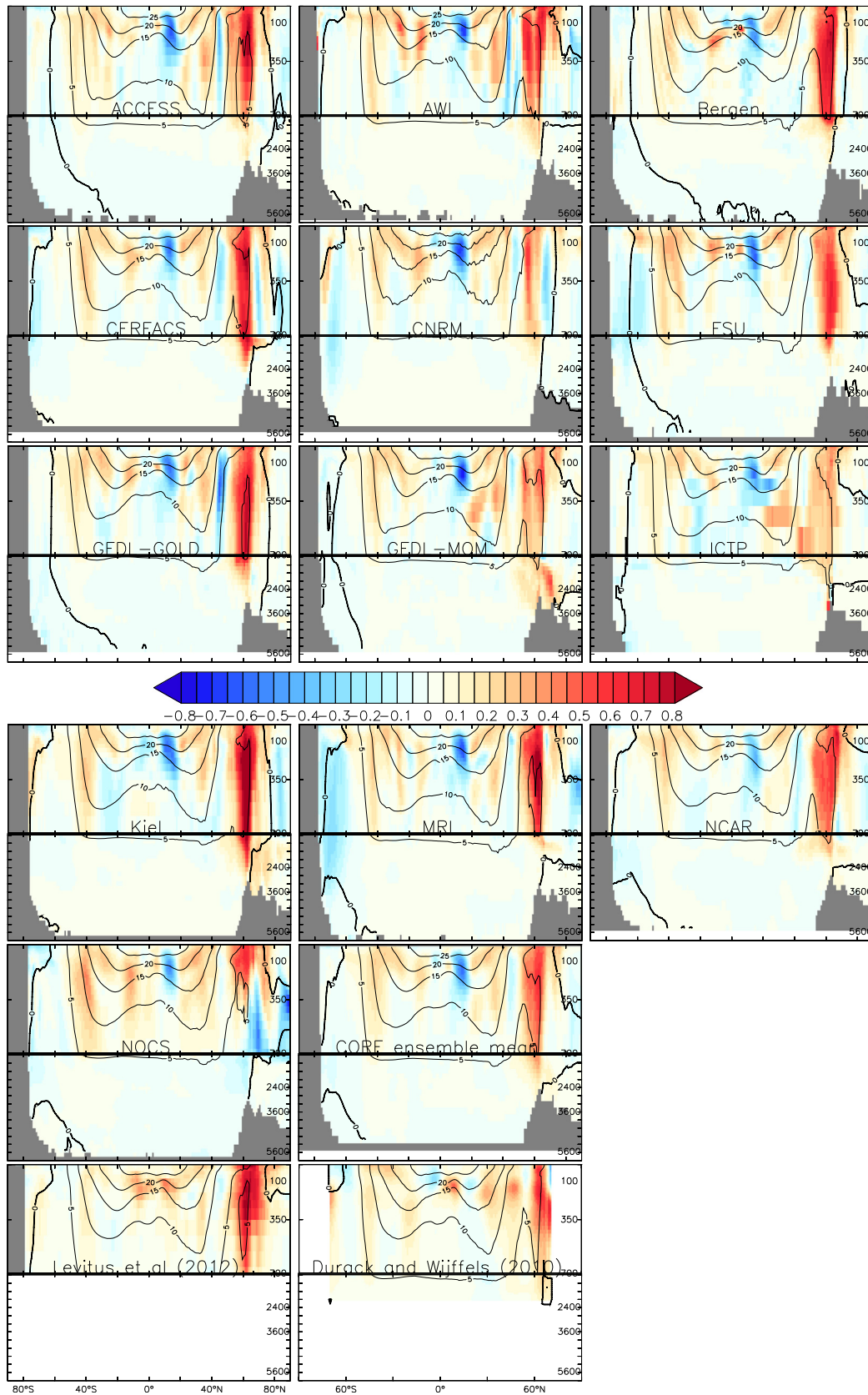


**Fig. 14.** Zonal average of the linear trend in annual mean ocean temperature ( $\text{deg C decade}^{-1}$ ) for the years 1993–2007 as computed from the fifth CORE-II cycle. Also shown are two estimates of the observation-based trends. Overlaying the trends are contours for the time mean temperature computed from each respective model and observation-based analysis. The upper 700 m of the ocean is split from the deeper ocean to emphasize changes in the upper ocean. The images are computed by first mapping the 3d model results to a common spherical grid with a common vertical spacing, and then performing the zonal average.

In the 1980s and early 1990s, the North Atlantic Oscillation (NAO) exhibited a persistent positive phase and the associated large negative surface fluxes acted as a pre-conditioner for an enhanced Atlantic meridional overturning circulation (AMOC). During this period, enhanced poleward oceanic heat transport associated with an enhanced AMOC was largely balanced by surface cooling due to the positive NAO. Around 1995/1996, a reduction in the surface ocean heat loss associated with a change in the NAO to its negative (or neutral) phase allowed for the northward oceanic heat transport to cause the subpolar gyre to transition to an anomalously warm phase. See [Esselborn and Edén \(2001\)](#) for attribution of 1990s sea level variability to redistribution of upper-ocean heat content associated with a fast dynamical response of the circulation to a drop in the NAO index. Further details can be found in [Lohmann et al. \(2009\)](#), [Robson et al. \(2012\)](#), [Yeager et al. \(2012\)](#) and [Danabasoglu et al. \(2014\)](#). This behaviour highlights that much of the Atlantic trend shown over this period is related to natural variability, with this point also emphasized by [Large and Yeager \(2012\)](#). We also note that the dipole pattern of warm-north/ cold-south within the North Atlantic, recently analyzed by [Yin and Goddard \(2013\)](#), is indeed reflected in the CORE ensemble mean (see Section 5.5 for more discussion).

Most models indicate a net cooling over the central and eastern tropical Pacific reflecting an ENSO-like pattern (as in the [Durack and Wijffels \(2010\)](#) analysis); a general pattern of warming in the equatorial flank of the Southern Ocean and cooling to the poleward flank; and a general warming for the Kuroshio region of the northwest Pacific ([Fig. 12 and 13](#)). For regions outside the strong trends in the North Atlantic, the zonal mean trends shown in [Fig. 14](#) indicate some variety in the upper ocean warming, largely in the middle to lower latitudes. There is a slight cooling seen around 20°–30°N in the upper ocean, and cooling in the abyssal Southern Ocean in many models. The deep Southern Ocean cooling trend may be indicative of a model drift that does not correspond to the estimated observed warming trends discussed by [Purkey and Johnson \(2010\)](#). It may also indicate a problem with the CORE-II atmospheric state, perhaps with too cold air temperatures inducing deep cooling, despite the corrections detailed in [Large and Yeager \(2009\)](#).

The broad qualitative agreement between the CORE-II simulations and observation-based analyses indicates some skill in the CORE-II simulations to capture patterns of observed trends in upper 700 m heat content. Certainly there are regions of differences. But given uncertainty in the observation-based analysis, and the wide range of model formulations considered in the CORE-II suite, we are generally pleased with the agreement. Furthermore, the agreement adds confidence to both the observation-based analyses and to the CORE-II simulations.

## 5. Dynamic sea level during 1993–2007

In [Fig. 15](#), we present the time mean of the dynamic sea level (Eq. (5)) over years 1993–2007 for the CORE-II simulations, as well as the dynamic sea level from the gridded satellite altimeter product from the AVISO project (Archiving, Validation, and Interpolation of Satellite Oceanographic) ([Le Traon et al., 1998](#); [Ducet et al., 2000](#)). Recall from the definition in Eq. (5), the DSL has a zero global area mean. [Fig. 16](#) shows the anomalies (model minus satellite), with model results mapped to the same spherical grid as the satellite analysis. The root-mean-square difference over the satellite region is computed according to

$$\text{RMS} = \sqrt{\frac{\int dA (\zeta - \zeta^{\text{obs}})^2}{\int dA}} \quad (12)$$

with  $dA$  the area of a grid cell and  $\zeta^{\text{obs}}$  the dynamic sea level from AVISO. The numbers are given in [Table 2](#). The models cluster around a global error between 0.09–0.15 m. The ensemble mean has a smaller difference than any of the models, except for CERFACS and NOCS.

[Fig. 17](#) shows the zonal mean of the RMS difference for the dynamic sea level in the models relative to AVISO, including the zonal mean of the difference for the ensemble mean. Note how the models generally are more consistent with observations in the lower latitudes, with the high latitudes leading to largest errors, particularly in regions of mode and deep water formation (poleward of 40 degrees latitude) as well as western boundary currents in the Atlantic and Pacific (see the difference maps in [Fig. 16](#)). Differences in simulated high latitude sea ice may also contribute to model differences from the satellite measures.<sup>3</sup> The north–south gradient of dynamic sea level across the Southern Ocean is weaker for many of the simulations relative to AVISO, perhaps suggesting a weaker than observed zonal transport in the Antarctic Circumpolar Current or a latitudinal shift in the models. The positive anomalies in the tropical Pacific, extending eastward from the warm pool region, may be a result of wind errors, as suggested when running the CERFACS model using the ECMWF-reanalysis based Drakkar forcing from [Brodeau et al. \(2010\)](#) (Christophe Cassou, personal communication, 2013). In general, we conclude that each of the CORE-II simulations produces a respectable 1993–2007 time mean dynamic sea level, meeting or surpassing the accuracy of the historical simulations considered as part of the CMIP3 analysis of [Yin et al. \(2010a\)](#).

In the remainder of this section, we present linear trends in dynamic sea level and associated steric and bottom pressure patterns computed over years 1993–2007 during the 5th CORE-II cycle. Note that for all figures in this section, we first subtract the global area mean of a chosen pattern for each year (to reveal the dynamic sea level as defined by Eq. (5)), and then compute the linear trend for the anomalous patterns.

### 5.1. Description of dynamic sea level (DSL) trends

[Fig. 18](#) shows the linear trend in annual mean dynamic sea level for years 1993–2007 in the CORE-II simulations, as well as the satellite measured sea level trend of the AVISO analysis. [Table 2](#) provides a root-mean-square difference between the models and AVISO within the satellite region. The observed DSL trend shows positive values in the western Pacific and the North Atlantic subpolar gyre, and negative values in the eastern and North Pacific as well as the Gulf Stream region. There is also a notable positive trend in the Southern Ocean south of Australia extending from the east Indian sector into the west Pacific sector. Adding the global sea level rise of 3.1 mm yr<sup>-1</sup> since 1993 increases/decreases the area and magnitude of the positive/negative sea level trends. In particular, the total sea level trend in the western Pacific since 1993 has been up to 10 mm yr<sup>-1</sup>, at least three times faster than the global mean, whereas sea level in the eastern Pacific has depressed. The Pacific pattern is likely dominated by inter-decadal variability and is closely related to the Pacific Decadal Oscillation ([Feng et al., 2010](#); [Bromirski et al., 2011](#); [Merrifield et al., 2012](#); [McGregor et al., 2012](#); [Zhang and Church, 2012](#)). We further discuss the Pacific patterns in Section 5.6. Similarly, the pattern in the North Atlantic mainly reflects decadal to multi-decadal time scale variability as impacted by the North Atlantic Oscillation ([Häkkinen and Rhines, 2004](#); [Lohmann et al., 2009](#); [Yeager et al., 2012](#); [Danabasoglu et al., 2014](#)).

<sup>3</sup> A detailed analysis of the freshwater budget and sea ice over the Arctic Ocean in the CORE-II simulations will be presented in a companion paper focusing on the Arctic region ([Qiang Wang, personal communication 2013](#)).

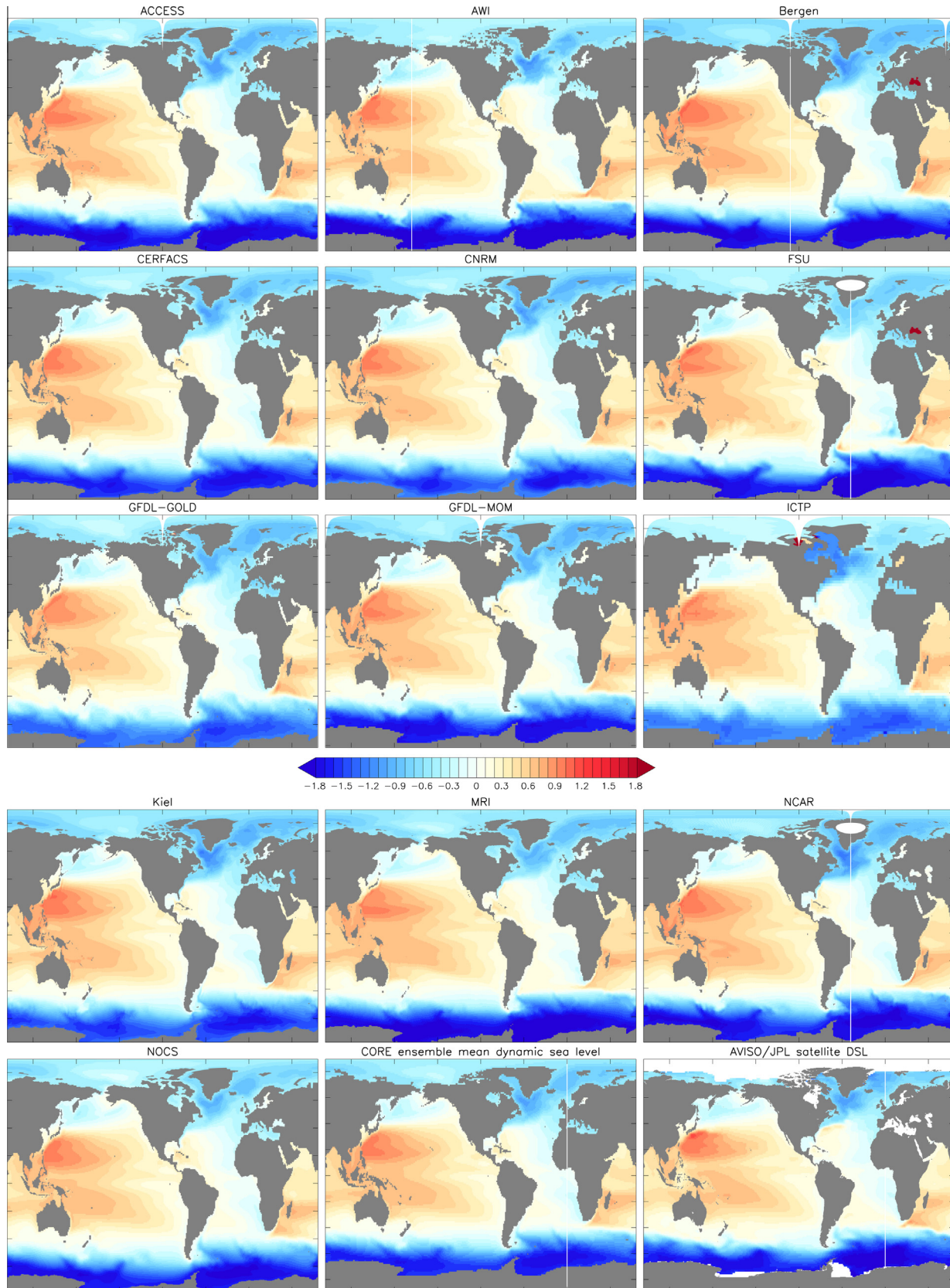


**Fig. 15.** Time mean dynamic sea level (metres) (Eq. (5)) for the years 1993–2007 as computed from the fifth CORE-II cycle, along with the ensemble mean from the CORE-II simulations. Also shown are observation-based estimates of the time mean based on satellite measurements as analyzed by JPL. The JPL sea level field was obtained from AVISO, and downloaded from [podaac.jpl.nasa.gov/dataset/AVISO\\_L4\\_DYN\\_TOPO\\_1DEG\\_1MO](http://podaac.jpl.nasa.gov/dataset/AVISO_L4_DYN_TOPO_1DEG_1MO). The area mean for each pattern has been removed, so that the field has a zero area integral. The spatial correlation between the CORE ensemble mean and the AVISO analysis is 0.95.

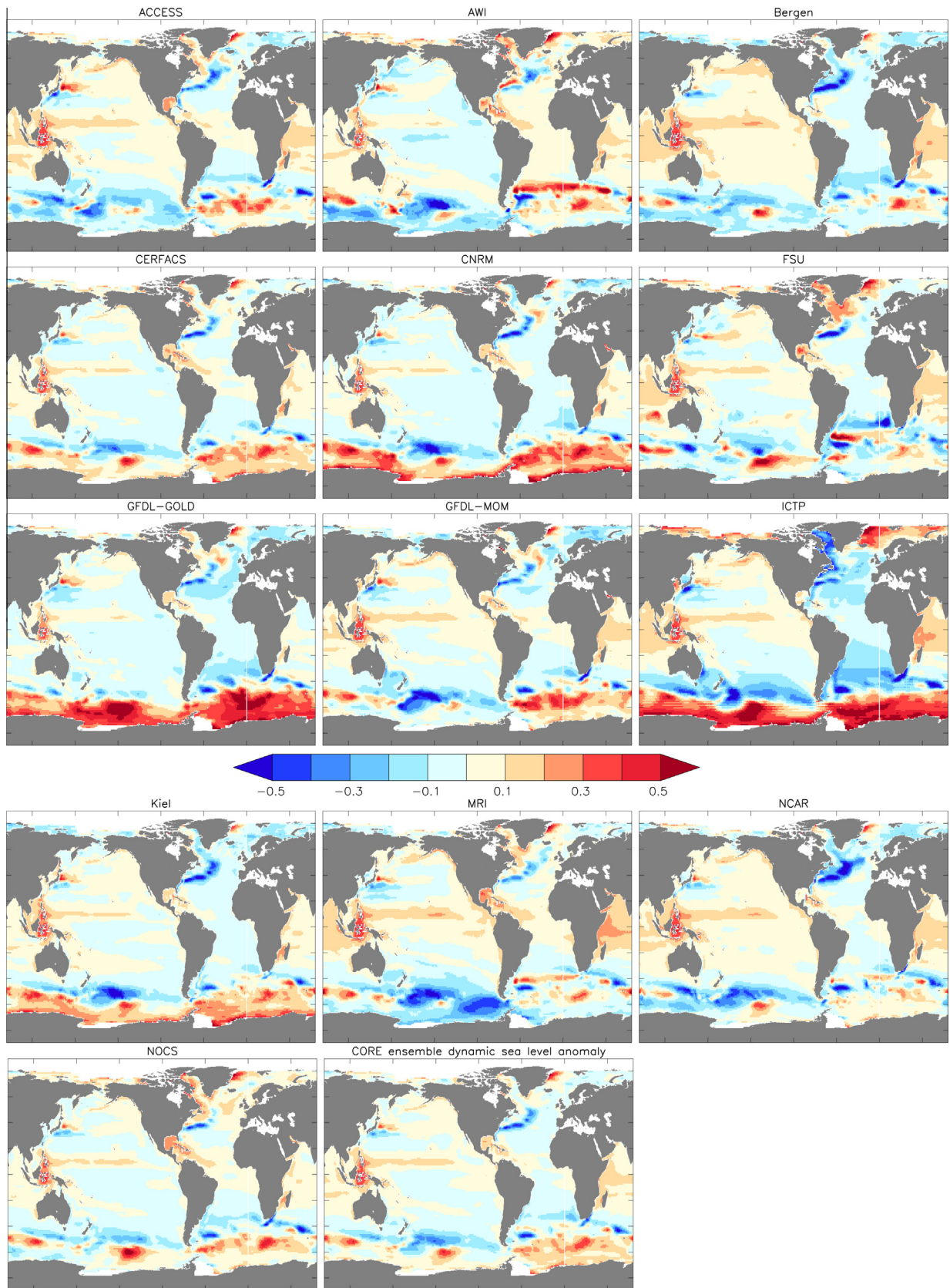


**Fig. 16.** Bias in dynamic sea level (metres) for the years 1993–2007 as computed from the fifth CORE-II cycle as compared to the satellite measurements analyzed by JPL/AVISO (see Fig. 15 caption). These patterns are computed as model minus satellite. The area mean for each pattern has been removed, so that the field has a zero area integral.

Determining whether long-term DSL trends exist in the Pacific and Atlantic basins is difficult due to the relatively short satellite records (Zhang and Church, 2012; Meyssignac et al., 2012). In the

Atlantic subpolar gyre and eastern North Atlantic, it takes about 20–30 years for a decadal sea level trend to rise above variability associated with high-frequency wind-driven and eddy generated

**Table 2**

Root-mean-square difference (metre) between the time mean (1993–2007) dynamic sea level from the CORE-II simulations and the JPL/AVISO satellite product over the same years (see Fig. 15 for the horizontal patterns). Also shown is the RMS difference ( $\text{mm yr}^{-1}$ ) between the DSL linear trend over years 1993–2007 in the CORE-II relative to the JPL/AVISO analysis (see Fig. 18 for the horizontal patterns). The statistics were computed over the satellite region, which is roughly within the latitude band  $60^\circ\text{N}$ – $60^\circ\text{S}$ . Each model result is remapped to the one-degree spherical grid defined by the JPL/AVISO grid in order to compute pattern differences.

Model	RMS diff for mean DSL (metre)	RMS diff for linear trend DSL ( $\text{mm yr}^{-1}$ )
ACCESS	0.11	3.0
AWI-FESOM	0.12	3.2
Bergen	0.12	2.6
CERFACS	0.10	2.8
CNRM	0.11	2.9
GFDL-GOLD	0.12	2.8
GFDL-MOM	0.12	3.0
FSU-HYCOM	0.12	3.5
ICTP	0.15	3.1
Kiel-ORCA05	0.10	3.1
MRI	0.13	3.1
NCAR	0.12	2.8
NOCS	0.09	2.7
CORE-II ensemble mean	0.10	2.6

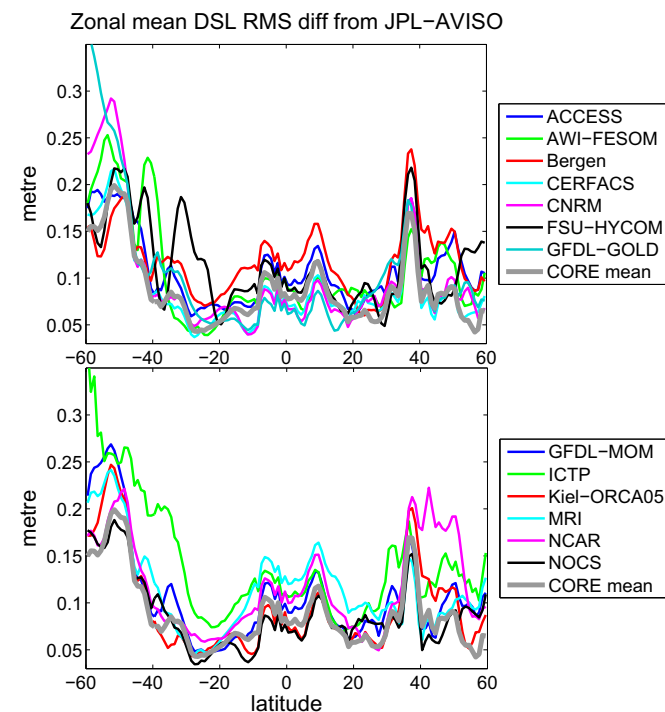


**Fig. 17.** Zonal mean of the root-mean-square difference in the 1993–2007 time mean dynamic sea level with respect to the observations (Fig. 15). This difference was computed as  $\sqrt{\int dx (\zeta - \zeta^{\text{obs}})^2} / \int dx$ , where  $\zeta^{\text{obs}}$  is the dynamic sea level taken from the AVISO product detailed in the caption to Fig. 15, and the zonal integral extends over the World Ocean. The satellite measurements cover a latitude band roughly equal to  $60^\circ\text{N}$ – $60^\circ\text{S}$ . The zonal mean difference for the ensemble mean sea level pattern is shown here in solid gray. Note the relatively small difference in the lower latitudes and large differences in the high latitudes, particularly in the Southern Ocean.

processes (Lorbacher et al., 2010). Kopp (2013) suggests that a long-term trend in sea level along the eastern US coast is only a recent occurrence, with no detectable trends in this region prior to 1980. Köhl and Stammer (2008), following Roemmich et al. (2007), suggest that much of the rise in dynamic sea level within the South Pacific subtropical gyres is associated with atmospheric decadal variability modes impacting the wind stress curl.

The simulations generally show positive/negative values in the western/eastern Pacific DSL trends, with structures comparing reasonably well to observations. However, most models simulate a strong negative centre at  $135^\circ\text{W}$ ,  $15^\circ\text{N}$ , with the magnitude stronger than in the observations. Also, the models generally show a decreasing trend in the Southern Ocean south of Australia, which is opposite to the positive trend found in the satellite analysis.

To varying degrees, the simulations and observations show a rise of the DSL south of Greenland. This rise in the models reflects the increased heat content in this region, as shown in Figs. 12 and 14. This heat content increase is associated with a recent spin-down of the subpolar gyre by decreased surface cooling in this region (Häkkinen and Rhines, 2004), whilst the northward meridional heat transport coming from the south is still high (Lohmann et al., 2009; Yeager et al., 2012; Danabasoglu et al., 2014).

In the Arctic ocean, where no satellite sea level measurements are available, most models simulate a significant rise of the DSL, especially in the Beaufort gyre region, and a lowering in the Canadian Archipelago and around Greenland. As shown in Fig. 23 discussed in Section 5.3, these changes are associated with halosteric effects. The rise in sea level north of Eurasia is associated with reductions in sea ice cover (e.g., Laxon et al., 2013), and increases in Eurasian river discharge (e.g., Peterson et al., 2002, 2011). The lowering of DSL in the Canadian Archipelago and around Greenland is associated with the increased salt content in regions impacted by the North Atlantic, where the changes in meridional transport are advecting more salt into this region.

In addition to the above regional trends, there are changes in the tropical Indian and Atlantic oceans and the South Atlantic, with CORE-II simulations and observations agreeing that the trends are small. Moving further south, the Southern Ocean mode water regions around  $40^\circ\text{S}$ – $50^\circ\text{S}$  generally show an increasing sea level trend, with AVISO also showing such a trend, though somewhat smaller than some of the models. The trend may be related to the southward shift of the westerlies (Yin, 2005; Yin et al., 2010a).

## 5.2. Sea level trends decomposed into mass and local steric effects

Tendencies in sea level can be decomposed into tendencies from mass and local steric changes. It has proven useful in various studies to perform this decomposition (e.g., Lowe and Gregory, 2006; Landerer et al., 2007b; Yin et al., 2009; Yin et al., 2010a; Pardaens et al., 2011a). For a hydrostatic fluid, this decomposition is written (see Eq. (47) in Appendix B.1)

$$\underbrace{\frac{\partial \eta}{\partial t}}_{\text{sea level tendency}} = \underbrace{\frac{1}{g\rho_o} \left( \frac{\partial(p_b - p_a)}{\partial t} \right)}_{\text{mass tendency}} - \underbrace{\frac{1}{\rho_o} \left( \int_{-H}^{\eta} \frac{\partial \rho}{\partial t} dz \right)}_{\text{local steric tendency}}. \quad (13)$$

This expression was introduced by Gill and Niiler (1973) for their analysis of observed steric changes over a seasonal cycle. The first term on the right hand side exposes those changes to sea level due to changes in the mass of fluid in an ocean column. As mass increases within a column, either through the movement of mass within the ocean, changes to the mass crossing the ocean boundary, or changes to the atmospheric pressure loading, the bottom pressure in turn increases and sea level also increases. We note that for the CORE-II simulations, changes associated with atmospheric loading are ignored, as all models impose a zero weight atmosphere on the ocean for purposes of driving ocean dynamics (see Appendix C5 in Griffies et al. (2009b)). The second term in equation (13) arises from local steric changes, in which decreasing density (as through warming) expands an ocean column and so raises sea level. As stated earlier, we are focused here on pattern changes, so differences in global means are removed, thus making our application of Eq. (13) equivalent for both Boussinesq and non-Boussinesq fluids.

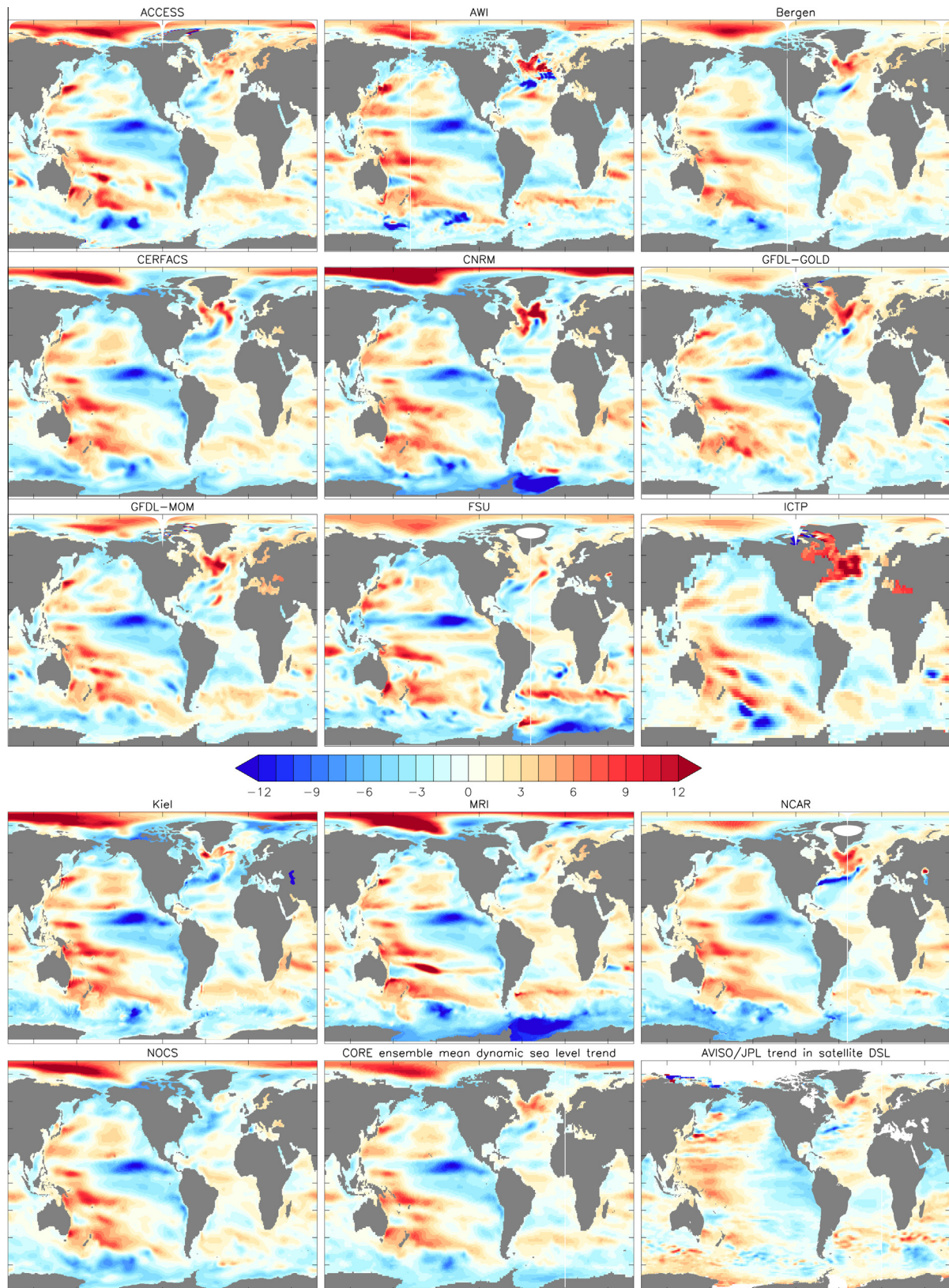


**Fig. 18.** Linear trend in annual mean dynamic sea level ( $\text{mm yr}^{-1}$ ) for the years 1993–2007 as computed from the fifth cycle of CORE-II simulations. Shown are results from the individual models as well as the ensemble mean computed using all simulations. Also shown are observation-based estimates of the trend based on satellite measurements (between roughly  $60^{\circ}\text{N}$ – $60^{\circ}\text{S}$ ) as analyzed at the Jet Propulsion Laboratory. The JPL sea level field was obtained from AVISO, and downloaded from [podaac.jpl.nasa.gov/dataset/AVISO\\_L4\\_DYN\\_TOPO\\_1DEG\\_1MO](http://podaac.jpl.nasa.gov/dataset/AVISO_L4_DYN_TOPO_1DEG_1MO). Root-mean-square differences of the trends are computed between the CORE-II simulations and the AVISO trend between roughly  $60^{\circ}\text{N}$ – $60^{\circ}\text{S}$ , with results given in Table 2. Linear trends for the model and observations are based on the annual mean of the spatial anomalous sea level field. That is, the trend is computed by first taking the annual mean sea level for each year and removing the global area mean, and then computing the trends of these annual mean spatial anomalies. The trends thus emphasize changes in patterns and do not include changes in the global mean. Consequently, positive trends in this figure represent sea level increases greater than the global mean, and negative trends are less than the global mean. For those regions where the AVISO analysis is nonzero, the spatial correlation between the CORE ensemble mean trend and the AVISO trend is 0.40.

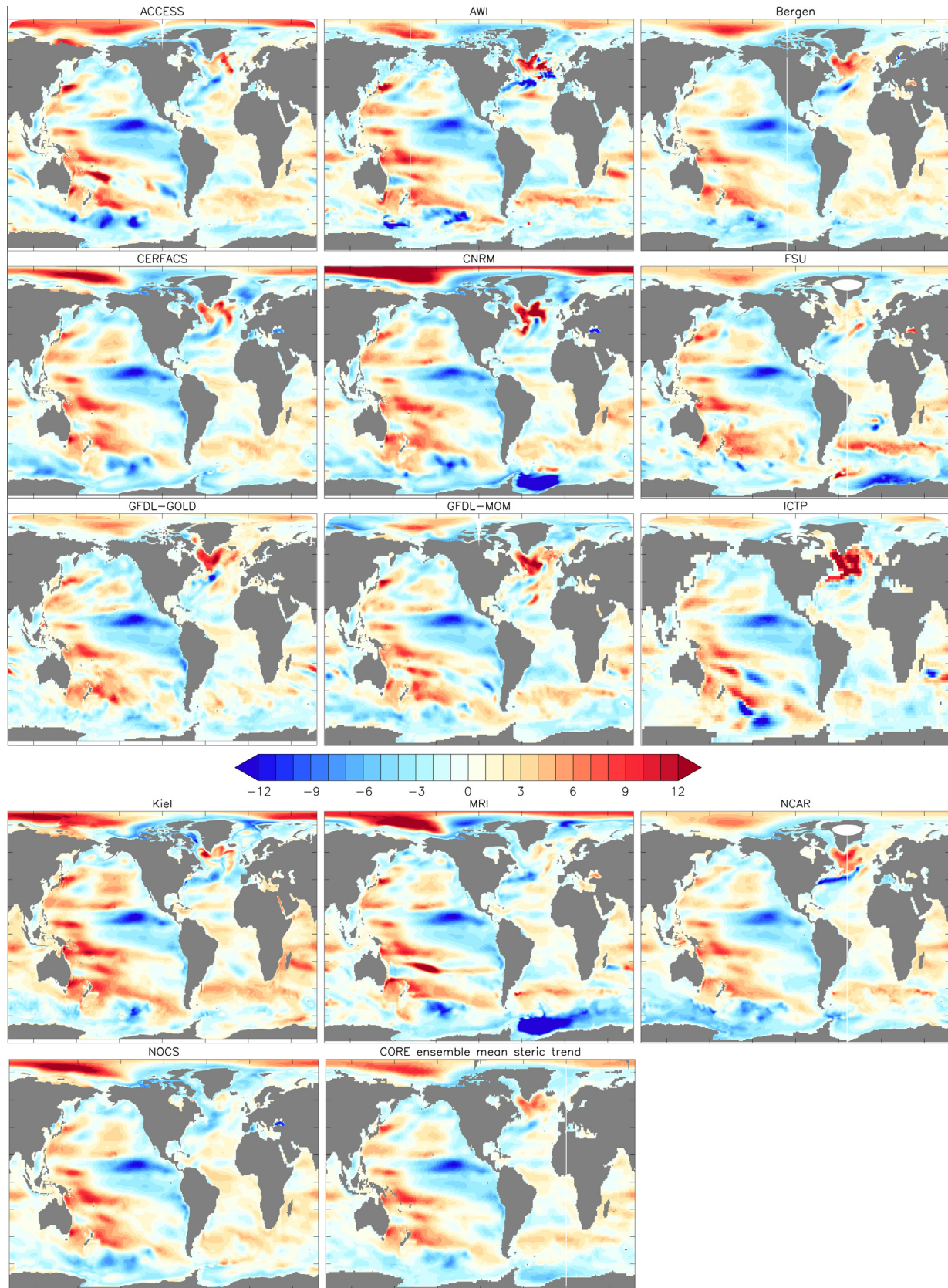


**Fig. 19.** Linear trend in local steric sea level over the years 1993–2007 for the 5th CORE-II cycle, following from equations (3) and (13). Shown are results from the individual models as well as the ensemble mean. The units are  $\text{mm yr}^{-1}$ . A root-mean-square difference from the ensemble mean is given in Table 3, with this statistic indicating the spread amongst the ensemble of CORE-II simulations. The linear trends are computed by taking the annual mean steric contribution to sea level for each year and removing the global mean, so that the trends emphasize changes in patterns.

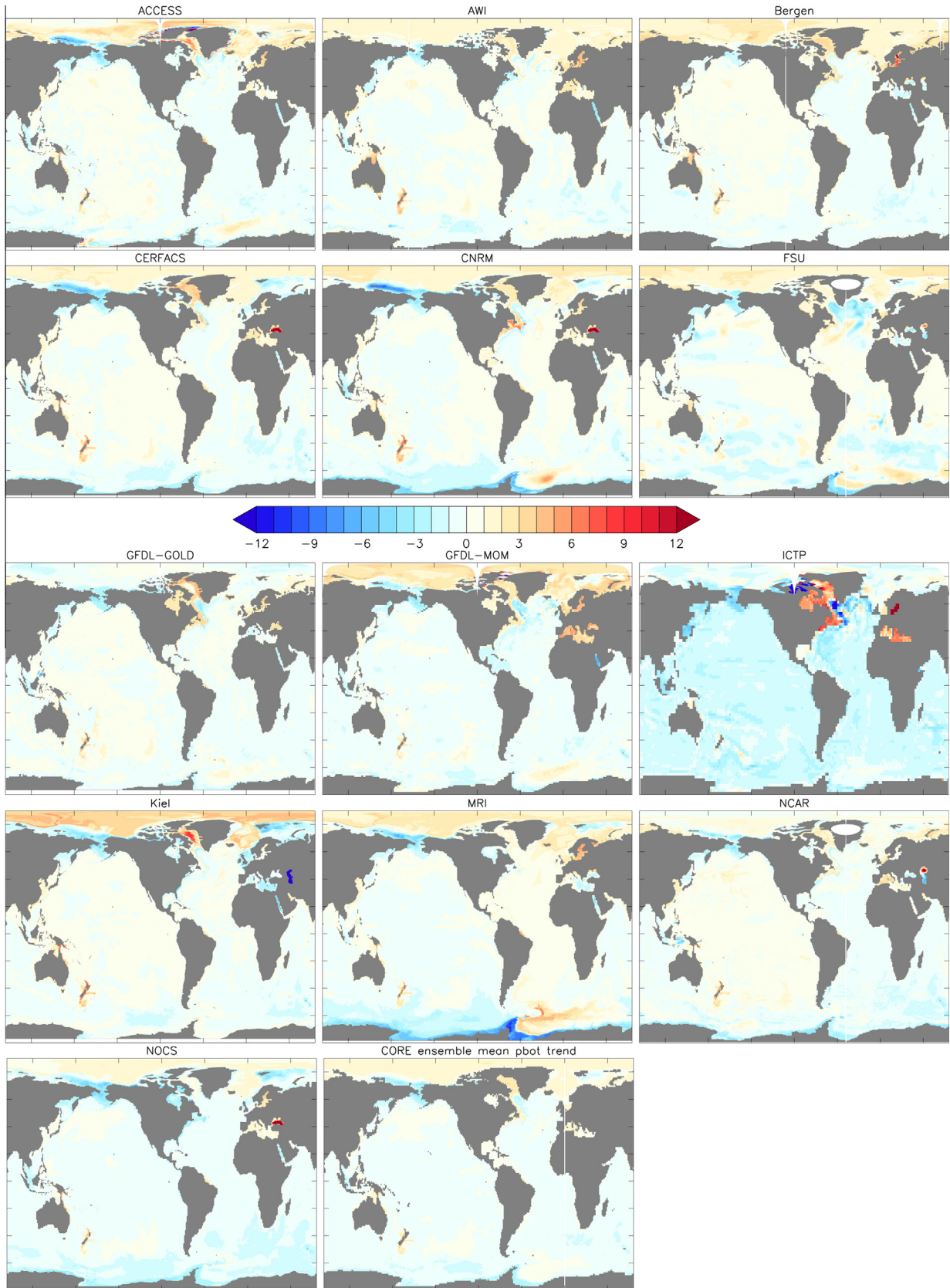


**Fig. 20.** Linear trend in bottom pressure, converted to  $\text{mm yr}^{-1}$  according to Eq. (13), for the years 1993–2007 as computed from the fifth CORE-II cycle. Shown are results from the individual models as well as the ensemble mean. The linear trends are computed by taking the annual mean bottom pressure for each year and removing the global mean, so that the trends emphasize changes in patterns. We keep the same colour scale as for the sea level and steric trends shown in Figs. 18–23 to facilitate direct comparison. However, Fig. 21 shows the ensemble mean with a smaller colour range to highlight changes in the higher latitudes. In general, the bottom pressure trends are far smaller than the steric trends. A root-mean-square difference from the ensemble mean is indicated in Table 3, with this statistic indicating the spread amongst the ensemble of CORE-II simulations. Note that the small basin-wide downward trend for the ICTP simulation is associated with the absence of water in this model returning from enclosed marginal seas to the main ocean basins. Correspondingly, we exclude the Baltic from this simulation for computation of the ensemble mean.

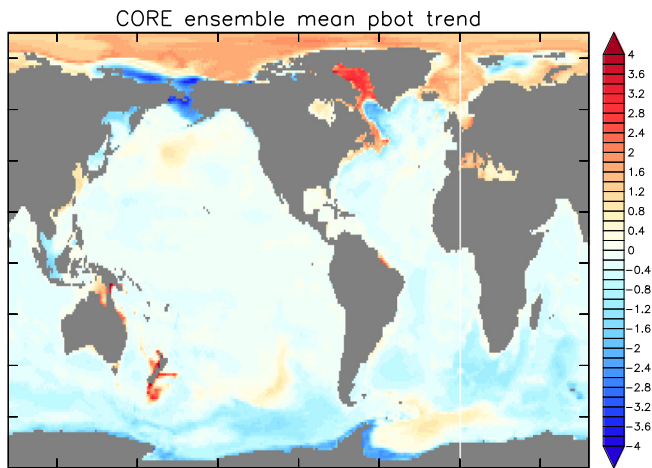


**Fig. 21.** Ensemble mean of the linear trend in bottom pressure, converted to  $\text{mm yr}^{-1}$  according to Eq. (13), for the years 1993–2007 as computed from the fifth CORE-II cycle. Shown are results from the ensemble mean as in Fig. 20, but with the colour scale reduced to emphasize the changes particularly in the higher latitudes and along shelves. Note the broad movement of mass from the Southern Hemisphere to the Northern Hemisphere, as discussed by Landerer et al. (2007a).

Fig. 19 exposes the linear trend in steric sea level (second term on right hand side of Eq. (13)), and Fig. 20 shows the trend in bottom pressure (first term on right hand side of Eq. (13)). Comparison to Fig. 18 indicates that the majority of the sea level trend is associated with steric changes. We thus have more to say regarding steric trends, including thermosteric and halosteric trends, in subsequent subsections.

The bottom pressure trends are largely localized to the Arctic regions, as well as certain shelf regions, with the shelf patterns more visible when choosing a smaller range for the colour bar as shown in Fig. 21. Landerer et al. (2007a,b), Yin et al. (2009) and Yin et al. (2010a) interpreted projections in the late 21st century of increased bottom pressure loading along shelves and marginal seas as arising from the tendency for deeper waters to expand more, thus creating a steric gradient moving mass towards the coast (see also Appendix B.1). The redistribution of ocean mass from the ocean interior towards the shallower shelf region is evident for the CORE-II simulations especially in the Arctic, given that the Arctic is the shallowest of the World Ocean basins. Indeed, as

noted by Landerer et al. (2007a), there is a general movement of ocean mass from the Southern Hemisphere to the Northern Hemisphere, which is reflected in the ensemble mean of the CORE-II simulations in Fig. 20. One exception is the region surrounding the Bering Strait and adjacent Siberian shelf region.

### 5.3. Steric sea level trends decomposed into thermosteric and halosteric trends

The steric term in Eq. (13) can be split into thermosteric and halosteric contributions, with details given in Appendix B.1. We note that changes in sea level due to pressure dependence of the *in situ* density are generally negligible (see Section A.5 for discussion of global mean sea level). Figs. 22 and 23 show the thermosteric and halosteric trends. In the Pacific, the steric sea level trend is dominated by thermosteric processes. However, the halosteric effect is important in the Atlantic, especially in the subpolar gyre region. In this region, the thermosteric and halosteric effects partially compensate, with the thermosteric effect being larger. Both the steric effect, through halosteric processes, and ocean mass redistribution contribute to the positive sea level trend in the Arctic.

Following Lombard et al. (2009) (see their Fig. 8), we present in Fig. 24 the correlation between time series of halosteric and thermosteric effects. Negative correlations indicate halosteric and thermosteric effects act mostly in a density-compensated manner so to reduce the overall steric effects relative to either the thermosteric or halosteric effects alone. Conversely, positive correlations mean thermosteric and halosteric effects act in concert. Density-compensated changes occur when advection is the dominant mechanism for transport, in which potential temperature and salinity are conserved on fluid parcels. We speculate that their impacts on density compensate one another largely because warm/salty waters and cold/fresh waters tend to occur in the mean due to climatological forcing (excess of precipitation in cold high latitudes; excess of evaporation in warm low latitudes). See also Section 2b in Wunsch et al. (2007) for more discussion.

The area average for the thermosteric/halosteric correlation over the World Ocean is negative for all of the models (see figure caption). As noted above, the Atlantic basin is notable for its rather large density-compensated fluctuations, whereas the other basins have some regions of nontrivial positive correlation. The bulk of the simulations have area averaged values of around  $-0.3$  to  $-0.4$ , with ACCESS, GFDL-MOM, ICTP, and GFDL-GOLD the largest negative correlations. Notably, the GFDL-GOLD and ICTP simulations indicate

**Table 3**

Global ocean root-mean-square difference ( $\text{mm yr}^{-1}$ ) between an individual CORE-II simulation and the ensemble mean of all CORE-II simulations. This statistic measures the spread amongst the ensemble. We compute this statistic for the linear trend in bottom pressure (Fig. 20); steric sea level (Fig. 19) and steric sea level over the upper 700 m of the ocean (Fig. 25); thermosteric sea level (Fig. 22) and thermosteric sea level over the upper 700 m of the ocean (Fig. 26); halosteric sea level (Fig. 23), and halosteric sea level over the upper 700 m of the ocean (Fig. 27). To compute the ensemble mean and differences, each model result is remapped to the one-degree spherical grid defined by the JPL/AVISO grid (Fig. 15). The final column shows the global area average of the correlation between the thermosteric and halosteric time series for the years 1993–2007, with the maps of this correlation shown in Fig. 24.

Model	Bott press	Steric (700 m)	Thermosteric (700 m)	Halosteric (700 m)	Correlate thermo/halo
ACCESS	0.48	1.53 (1.5)	2.2 (2.1)	1.4 (1.3)	−0.42
AWI	0.40	1.8 (1.56)	2.6 (2.3)	1.6 (1.4)	−0.28
Bergen	0.42	0.96 (0.86)	1.6 (1.3)	1.3 (0.92)	−0.36
CERFACS	0.36	1.0 (0.85)	1.7 (1.2)	1.3 (0.93)	−0.32
CNRM	0.51	2.2 (1.5)	2.7 (1.9)	1.6 (1.5)	−0.29
FSU	0.75	1.7 (1.3)	2.5 (1.9)	1.5 (1.2)	−0.49
GFDL-GOLD	0.48	1.4 (1.2)	2.4 (1.8)	2.0 (1.4)	−0.52
GFDL-MOM	0.54	1.4 (1.3)	2.6 (2.2)	2.0 (1.5)	−0.43
ICTP	1.51	2.1 (1.9)	3.4 (2.8)	2.2 (1.6)	−0.45
Kiel	0.58	1.6 (1.5)	2.0 (1.4)	2.1 (1.7)	−0.30
MRI	0.76	2.0 (1.6)	2.6 (2.0)	1.4 (1.2)	−0.38
NCAR	0.48	1.2 (1.1)	1.5 (1.2)	1.1 (1.0)	−0.33
NOCS	0.47	1.1 (0.88)	1.8 (1.2)	1.2 (0.94)	−0.30

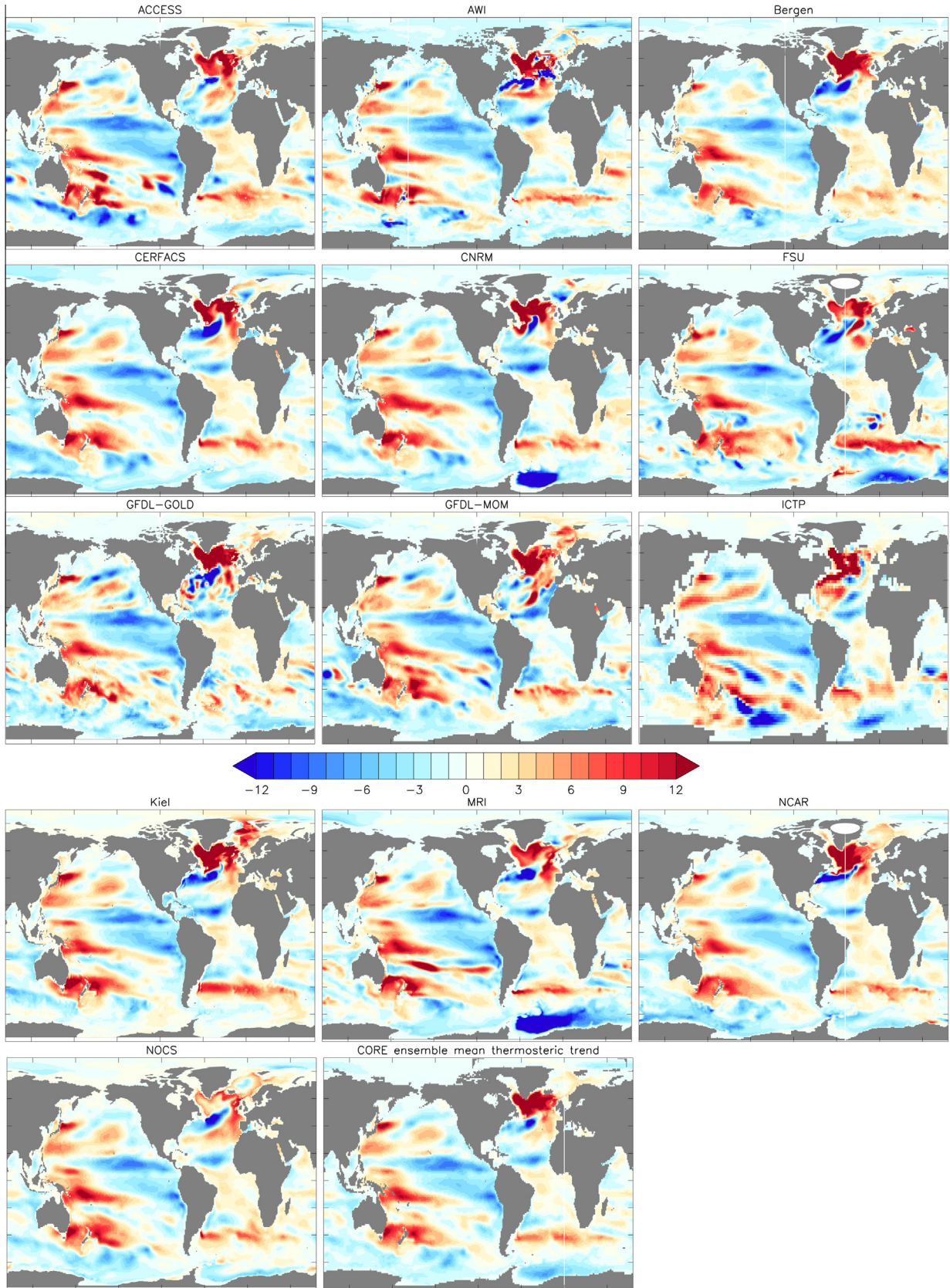


**Fig. 22.** Linear trend in thermosteric sea level over the years 1993–2007 for the 5th CORE-II cycle. Shown are results from the individual models as well as the ensemble mean. The ensemble mean is computed using all simulations. The units are  $\text{mm yr}^{-1}$ . The linear trends are computed by taking the annual mean thermosteric contribution to sea level for each year and removing the global mean, so that the trends emphasize changes in patterns. A root-mean-square difference from the ensemble mean is given in Table 3, with this statistic indicating the spread amongst the ensemble of CORE-II simulations.

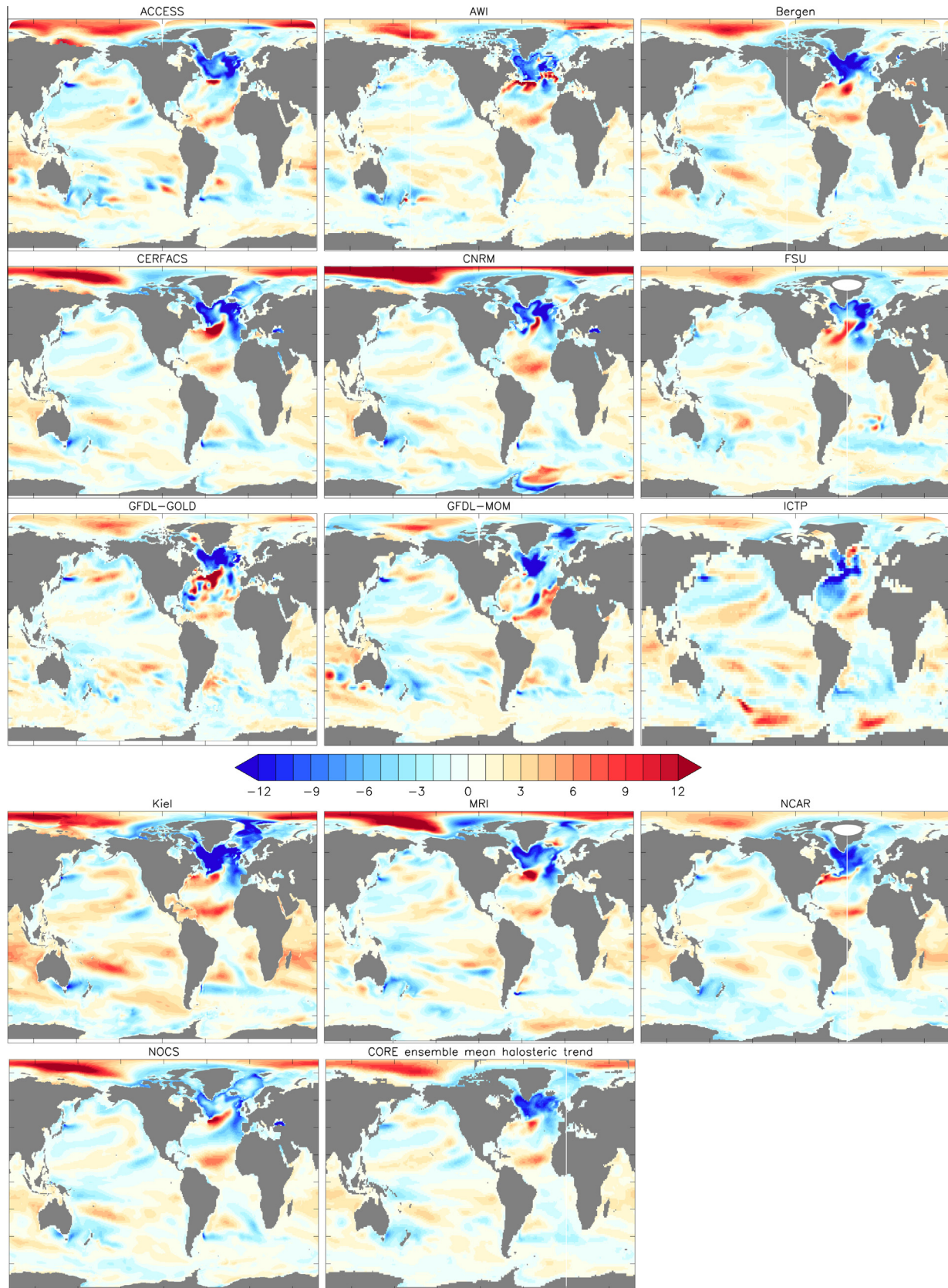


**Fig. 23.** Linear trend in halosteric sea level over the years 1993–2007 for the 5th CORE-II cycle. The units are  $\text{mm yr}^{-1}$ . Shown are results from the individual models as well as the ensemble mean. The ensemble mean is computed using all simulations. The linear trends are computed by taking the annual mean halosteric contribution to sea level for each year and removing the global mean for that year, so that the trends emphasize changes in patterns. Note the generally smaller magnitude for the halosteric patterns in this figure relative to the thermosteric patterns shown in Fig. 22, with exceptions being the rather large contributions in the subpolar North Atlantic and the Arctic ocean. A root-mean-square difference from the ensemble mean is given in Table 3, with this statistic indicating the spread amongst the ensemble of CORE-II simulations.

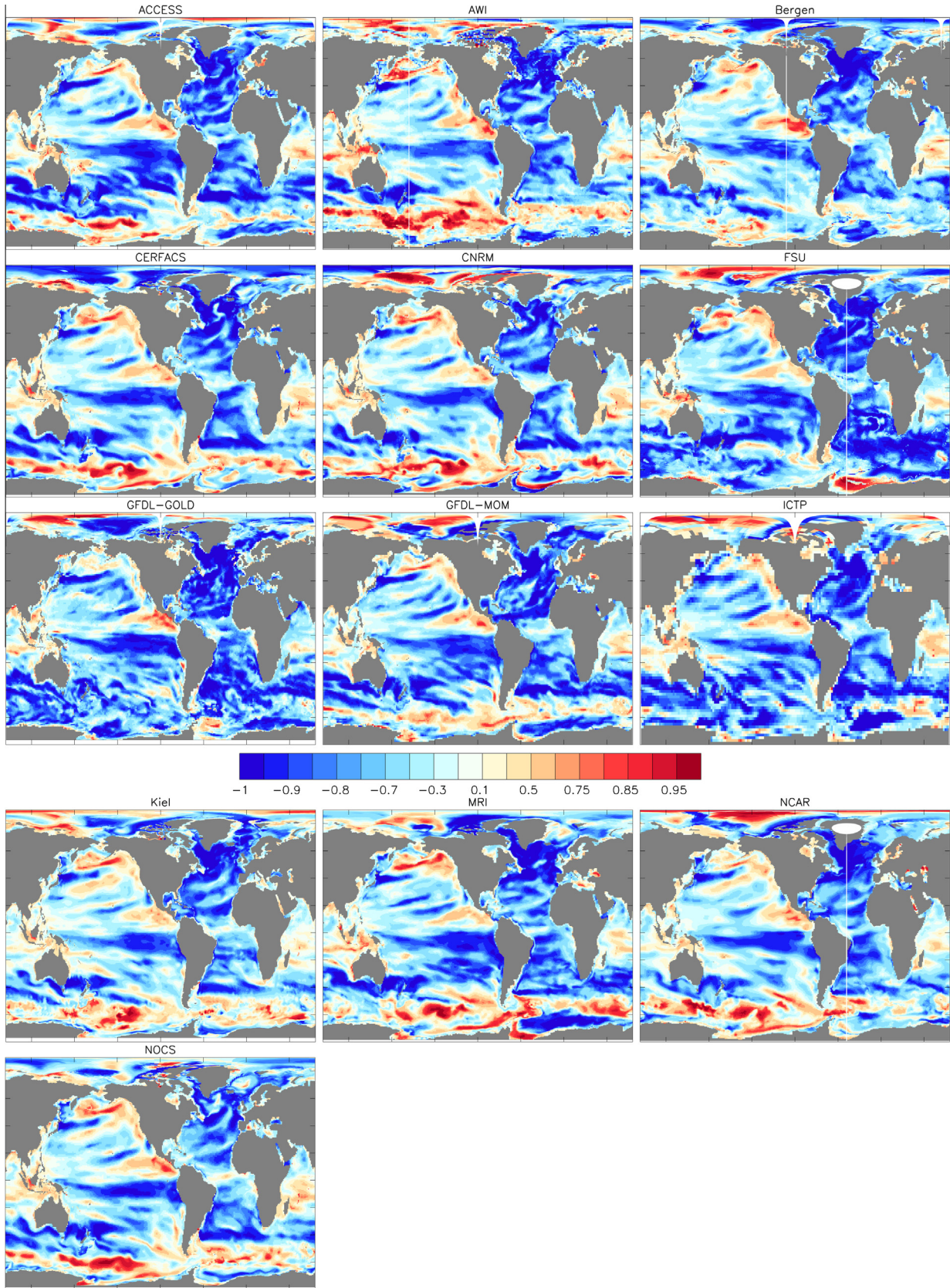


**Fig. 24.** Correlation between the time series of halosteric and thermosteric effects over the years 1993–2007 for the fifth CORE-II cycle. Positive values indicate halosteric and thermosteric effects acting in concert to either raise or lower sea level. The global area average of the correlation for each model is given in Table 3. The dominance of negative correlations indicates the dominance of density-compensated fluctuations in water masses.

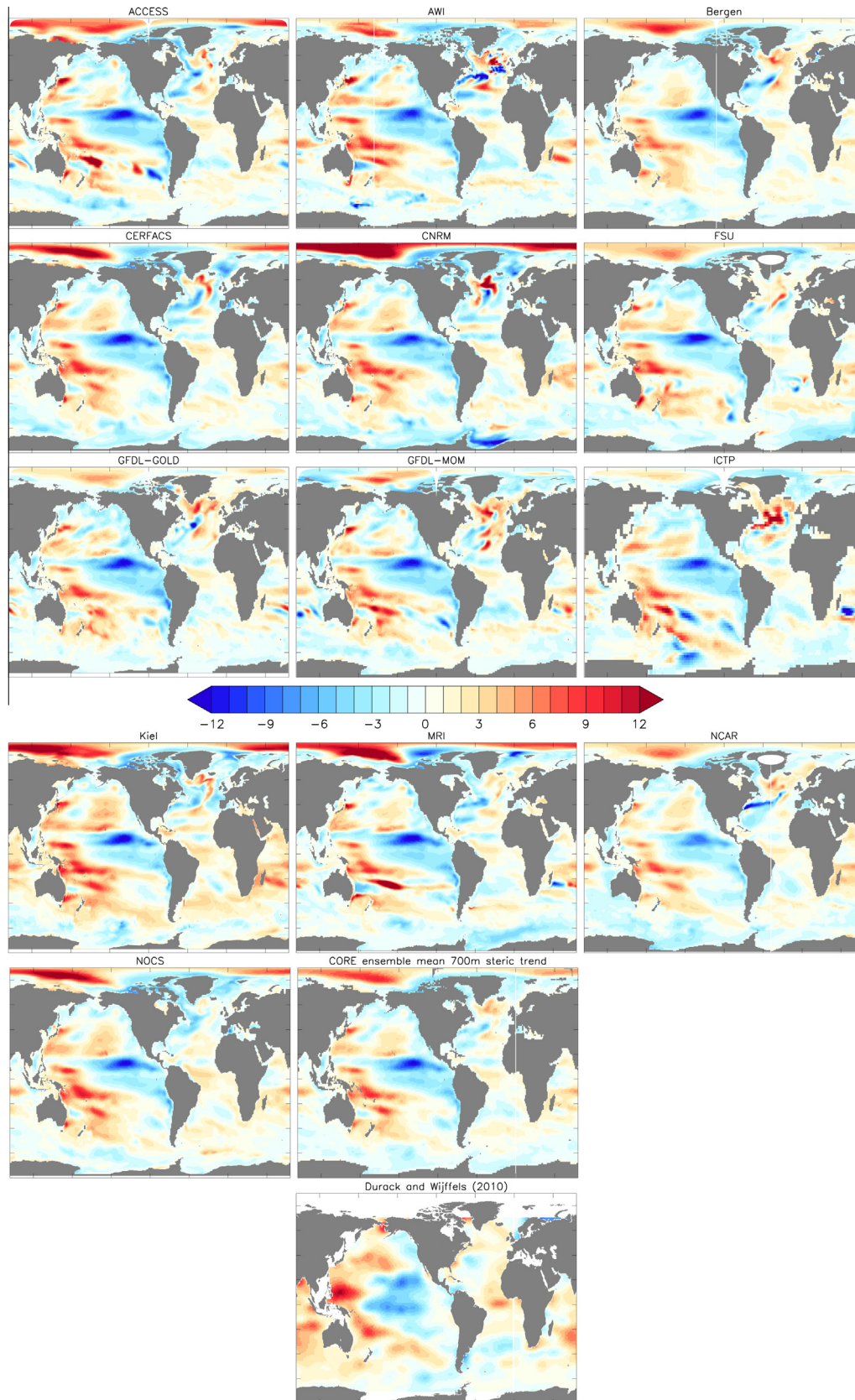


**Fig. 25.** Linear trend ( $\text{mm yr}^{-1}$ ) in steric sea level computed in the upper 700 m of water for years 1993–2007. The model results are taken from the 5th CORE-II cycle. The CORE-II ensemble mean is computed using all simulations. Observation-based estimates are shown from an updated analysis based on Durack and Wijffels (2010). The linear trends are computed by taking the annual mean steric contribution to sea level for each year and removing the global mean, so that the trends emphasize changes in patterns. A root-mean-square difference from the ensemble mean is given in Table 3. The spatial correlation between the CORE ensemble mean and the Durack and Wijffels (2010) observational analyses is 0.39.

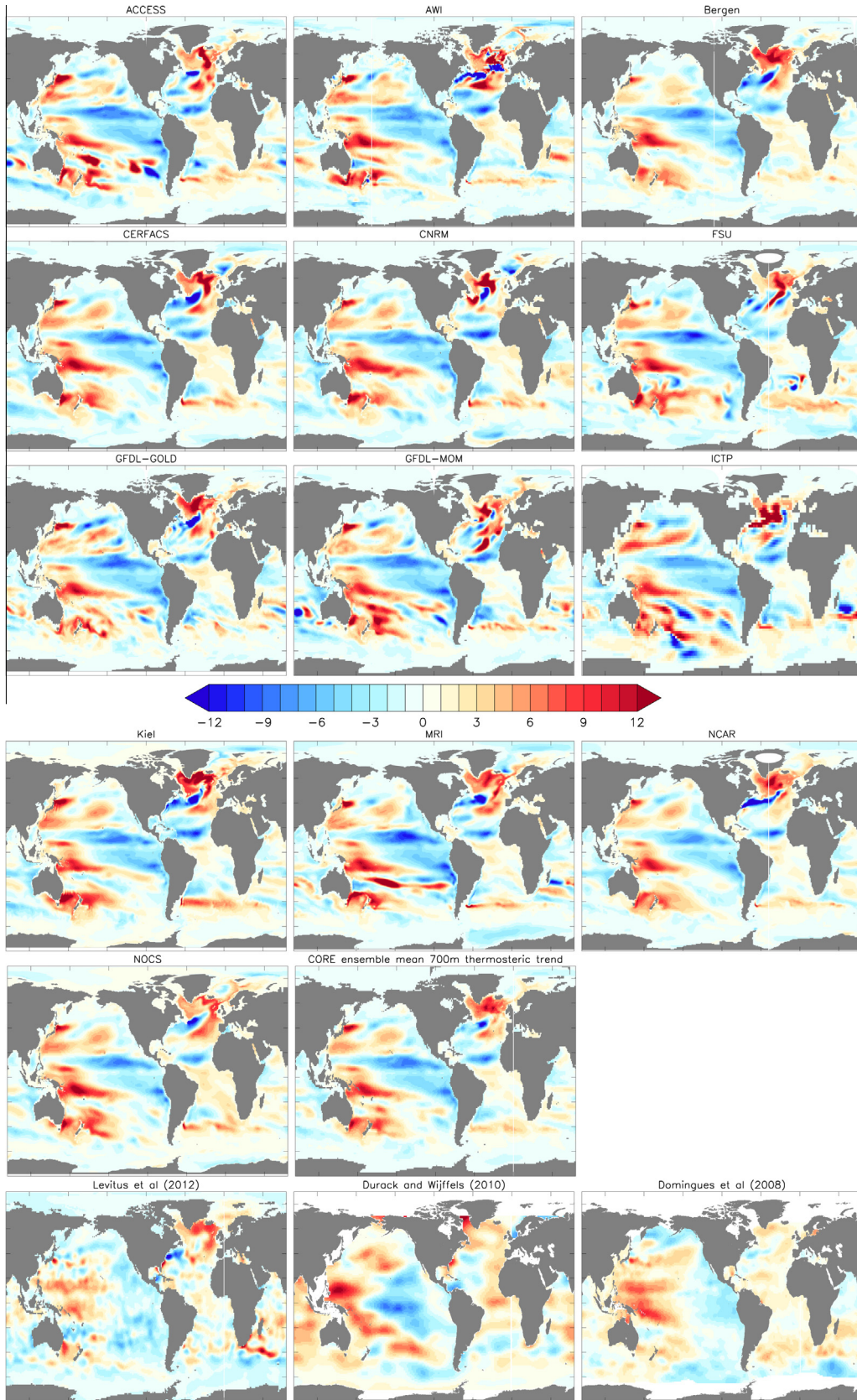


**Fig. 26.** Linear trend ( $\text{mm yr}^{-1}$ ) in thermosteric sea level computed in the upper 700 m of water for years 1993–2007. The model results are taken from the 5th CORE-II cycle. The CORE-II ensemble mean is computed using all simulations. Observation-based estimates are shown from Levitus et al. (2012); an updated analysis based on Domingues et al. (2008) and Church et al. (2010); and an updated analysis based on Durack and Wijffels (2010). The linear trends are computed by taking the annual mean thermosteric contribution to sea level for each year and removing the global mean, so that the trends emphasize changes in patterns. A root-mean-square difference from the ensemble mean is given in Table 3. The spatial correlation between the CORE ensemble mean and the observational analyses is given by CORE-Levitus = 0.31, CORE-Domingues = 0.43, CORE-Durack = 0.31.

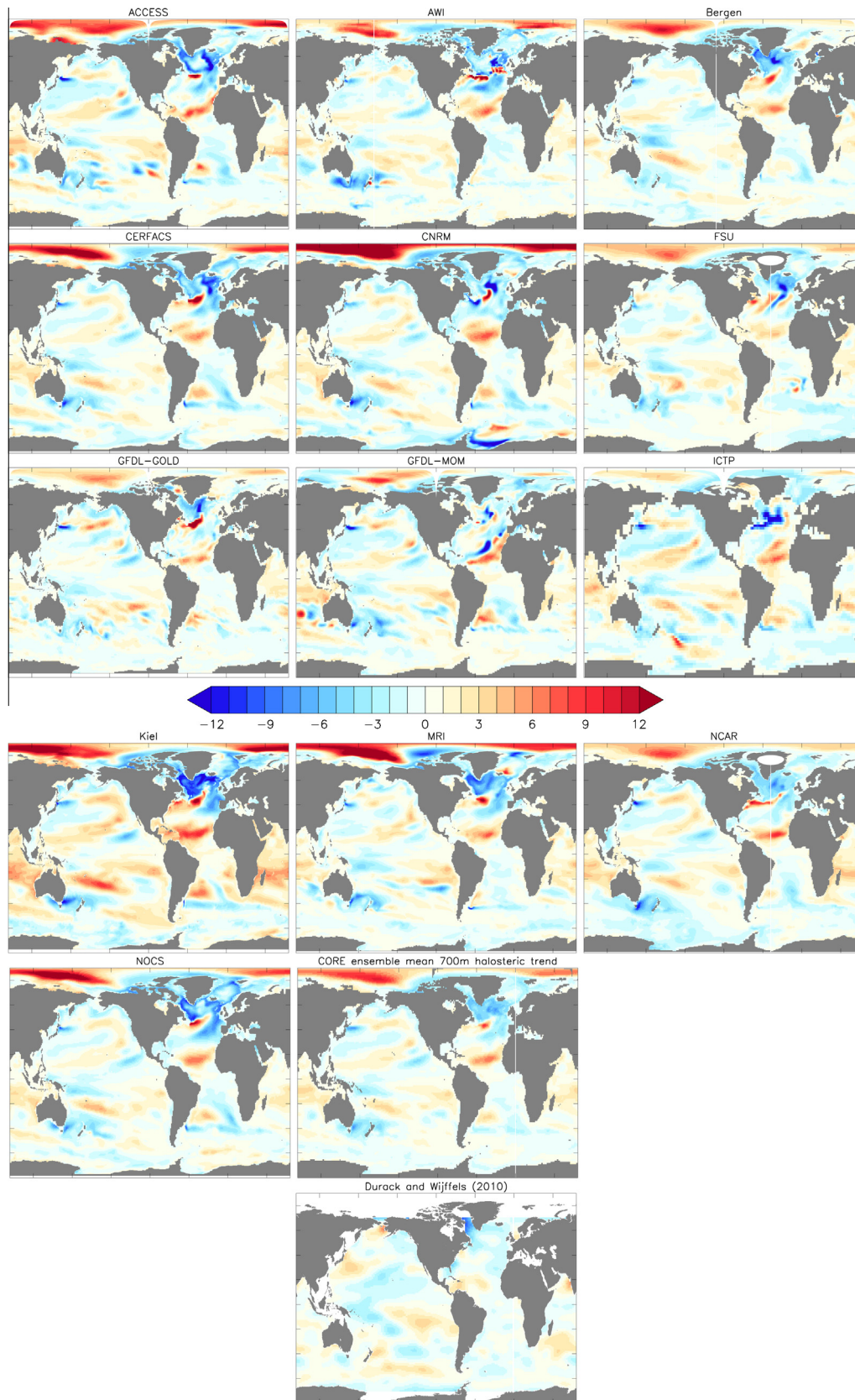


**Fig. 27.** Linear trend ( $\text{mm yr}^{-1}$ ) in halosteric sea level computed in the upper 700 m of water for years 1993–2007. The model results are taken from the 5th CORE-II cycle. The CORE-II ensemble mean is computed using all simulations. Observation-based estimates are shown from an updated analysis based on Durack and Wijffels (2010). The linear trends are computed by taking the annual mean halosteric contribution to sea level for each year and removing the global mean, so that the trends emphasize changes in patterns. A root-mean-square difference from the ensemble mean is given in Table 3, with this statistic indicating the spread amongst the ensemble of CORE-II simulations. The spatial correlation between the CORE ensemble mean and the Durack and Wijffels (2010) observational analysis is 0.18.

that compensation dominates in the Southern Ocean, whereas other models show closer to zero or slight positive correlations.

#### 5.4. Steric, thermosteric, and halosteric patterns over the upper 700 m

Limiting the analysis of steric trends to just the upper 700 m of the ocean allows us to compare the CORE-II simulations to various observation-based analyses. The Domingues et al. (2008) and Levitus et al. (2012) analyses focus on temperature changes, and so render an estimate only for thermosteric changes. The Durack and Wijffels (2010) analysis provides both temperature and salinity trends, and we use it to estimate linear trends in observed steric, thermosteric, and halosteric sea level.

We show the upper 700 m steric sea level trend in Fig. 25, with Figs. 26 and 27 showing the corresponding thermosteric and halosteric trends, respectively. As for the full depth trends (Figs. 19, 22, and 23), the upper 700 m steric trend is dominated by the thermosteric trend, except in the subpolar North Atlantic and Arctic. A prominent steric sea level trend pattern for both the models and the observations is seen in the Pacific west-east gradient. Domingues et al. (2008) and Levitus et al. (2012) show a somewhat diffuse western Pacific high and eastern Pacific low, reflecting that seen for the satellite-based dynamical sea level trends in Fig. 18. The models generally show a western Pacific positive trend closely aligned with the subtropical gyres, as well as an equatorial low that extends further into the western Pacific than seen in Domingues et al. (2008) and Levitus et al. (2012), but somewhat reflective of that seen in Durack and Wijffels (2010). We have more to say regarding the Pacific trends in Section 5.6.

All models exhibit a maximum increase in steric sea level (Fig. 25) along a zonal band extending across the south tropical Indian Ocean at about  $10^{\circ} - 15^{\circ}\text{S}$ . This pattern is indicative of a remote impact of the western Pacific warming via the Indonesian Passages and subsequent westward transmission by baroclinic Rossby waves as suggested by Schwarzkopf and Böning (2011).

All models exhibit a rather small thermosteric trend in the Southern Ocean, whereas the full-depth thermosteric trend in Fig. 22 shows a somewhat larger trend magnitude. Hence, the full-depth trend has a significant contribution from trends in the

deep waters. Some of the deep Southern Ocean trend is associated with model drift, as some models show cooling whereas others show warming (see Fig. 14 for the trends in zonal mean temperature). Each of the observation-based analyses show a positive trend in the Southern Hemisphere middle latitude mode water regions, particularly in the southwest Pacific, South Atlantic, and South Indian Ocean. The models also respect this positive trend, though somewhat more strongly in the Southwest Pacific. It has been suggested by Sallée et al. (2008) and Lombard et al. (2009) that these changes arise from movement of ocean fronts due to wind changes associated with Southern Annular Mode variations.

We noted in Section 5.1 that the models exhibit an increase in sea level in the subpolar North Atlantic region, with this increase triggered (initiated) by decreased surface cooling in the sub-polar gyre over the period studied here, whilst the advective heat transport from the south is still anomalously high. The studies of Lohmann et al. (2009), Yeager et al. (2012) and Danabasoglu et al. (2014) provide more details. The Levitus et al. (2012) and Durack and Wijffels (2010) analyses reflect the positive sea level trend in this region, whereas it is largely missing in Domingues et al. (2008). As part of the North Atlantic changes in the models, many exhibit a significant thermosteric sea level decrease in the Gulf Stream extension, which is also reflected in the Levitus et al. (2012) analysis and to a smaller degree in Durack and Wijffels (2010) and Domingues et al. (2008).

As mentioned in Section 3, the halosteric patterns are subject to caveats related to the use of surface salinity restoring for the CORE-II simulations. Additionally, the details of restoring are distinct across the models (see Danabasoglu et al., 2014). Nonetheless, there are some common patterns, notably a positive halosteric trend in the Arctic and negative halosteric trend in the subpolar North Atlantic. The trends found in the Durack and Wijffels (2010) analysis share some features with the CORE-II simulations, such as a halosteric sea level lowering in the subpolar North Atlantic associated with an increased salinity. The Pacific patterns, however, show low correlation. The low Pacific agreement may be due to the smaller amplitude of the trend. The smaller trend may in turn be impacted relatively more by differences in the surface salinity restoring between the CORE-II simulations. In general,

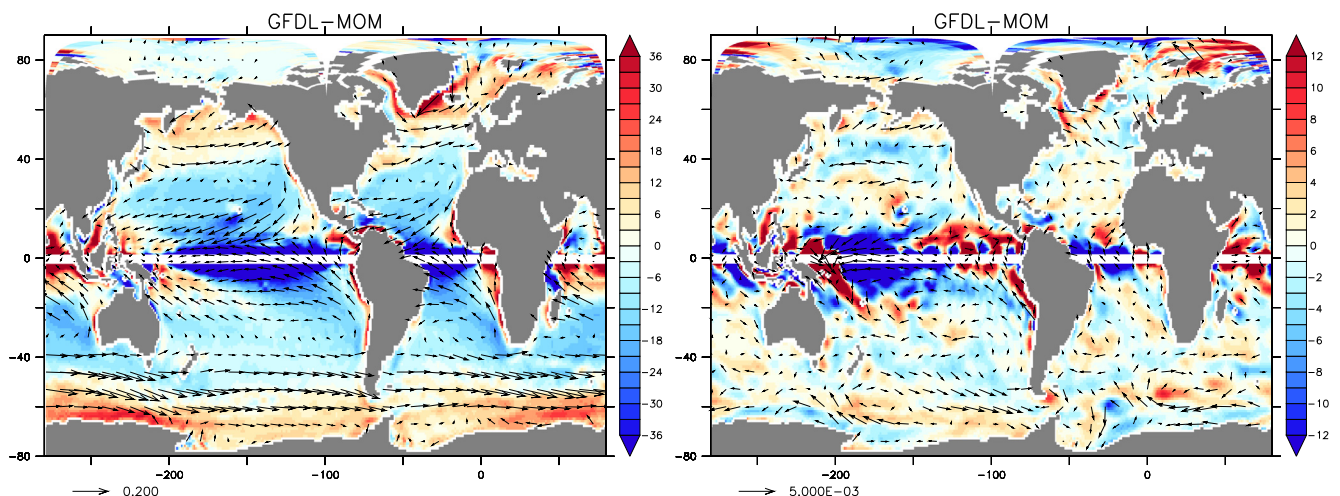


**Fig. 28.** Left panel: time mean wind stress vectors (stress applied to the ocean model surface;  $\text{N m}^{-2}$ ) and Ekman suction/pumping velocity,  $w_e = \rho_0^{-1} \hat{z} \cdot [\nabla \wedge (\tau/f)]$ , (colours;  $10^{-7} \text{ m s}^{-1}$ ) for years 1993–2007. Blue shading indicates downward Ekman pumping. The equatorial region is omitted due to vanishing Coriolis parameter. Right panel: linear trends, with wind stress trend (vectors) in units of  $\text{N m}^{-2} \text{ yr}^{-1}$  and trend in Ekman suction/pumping (colours) in units of  $10^{-8} \text{ m s}^{-1} \text{ yr}^{-1}$ . To minimize clutter, only every 9th vector in the x-direction and 7th vector in the y-direction are shown. We show results from the GFDL-MOM simulation, with other models showing similar structures, given that they all use the same atmospheric winds to generate stress. For the tropical and mid-latitude Pacific, note the trend for increased trade winds (easterlies) with near-equatorial Ekman downwelling in the central-west that pushes down the thermocline. This forcing is associated with increased thermosteric rise in the west Pacific as shown in Fig. 26 and as discussed by Feng et al. (2010), Bromirski et al. (2011), Merrifield (2011), Merrifield and Maltrud (2011).

the spatial correlation for the halosteric trends between Durack and Wijffels (2010) and the CORE ensemble mean is smaller than for the thermosteric trends.

### 5.5. Comments on the North Atlantic patterns of sea level change

North Atlantic dynamic sea level changes are influenced by the Atlantic meridional overturning circulation (AMOC). High-quality tide gauge records show that both the absolute values and acceleration of the sea level rise along the northeast USA, north of Cape Hatteras, were faster and larger than the global mean during the past 60 years (Sallenger et al., 2012; Ezer et al., 2013), consistent with model projections under the 21st century greenhouse-gas emission scenarios (Yin et al., 2009; Yin, 2012). In addition to a possible long-term trend, some studies have identified the potential role of multidecadal variability in this region (Chambers et al., 2012; Kopp, 2013). Nonetheless, recent sea level rise in this region exhibited some unusual behaviour. For example, most tide gauge stations on the New England and Canada coast recorded a large sea level jump during 2009–2010 of up to 100 mm, which is unprecedented and correlated with the 30% downturn of the AMOC (McCarthy et al., 2012) as well as the NAO index. During the period 1993–2007 considered in the present paper, the dynamic sea level in the North Atlantic was dominated by a dipole structure, with a DSL fall in the Gulf Stream and a DSL rise in the subpolar gyre (see Häkkinen and Rhines, 2004; Zhang, 2008). This dipole pattern has been captured by the CORE-II models as shown by the CORE-II ensemble mean in Fig. 18. Due to multi-decadal variability in North Atlantic, the decadal DSL trend shown in Fig. 18 may not be representative of the longer term.

### 5.6. Comments on the Pacific patterns of sea level change

The western Pacific is a hotspot for observed sea level rise, with the fastest sea level rise on the globe having occurred in this region since 1993. The west–east gradient of the dynamic sea level change seen in the simulations (Fig. 18) is consistent with the intensification of the easterly trade winds (see Fig. 28), according to the balance of the pressure gradient force and wind stress in the equatorial region (Timmermann et al., 2010; Merrifield, 2011; Merrifield and Maltrud, 2011; McGregor et al., 2012). The negative anomalies of the wind stress curl in the middle and western tropical Pacific cause downwelling of surface warm waters, and deepening of the thermocline (see Fig. 29). The downward migration of the thermocline leads to a significant thermosteric sea level rise in the western Pacific (Becker et al., 2012). In contrast, positive wind stress curl anomalies in the eastern tropical Pacific and along the west coast of South America result in an enhanced suction of cold deep water, and a shoaling of the thermocline. This process leads to a reduction in the sea level in the eastern Pacific.

Feng et al. (2010), Merrifield et al. (2012), Meyssignac et al. (2012) and McGregor et al. (2012) suggest that the west–east gradient of the DSL change reflects the negative phase of the Pacific Decadal Oscillation, rather than a trend induced by external climate forcing as originally proposed by Merrifield (2011) and Merrifield and Maltrud (2011). Interestingly, the wind stress curl caused a similar downwelling in the tropical Atlantic. But the dynamic sea level signal is weaker than in the Pacific (Fig. 18), with this difference perhaps due to the different size of the two ocean basins. Zhang and Church (2012) pointed out that the spatial patterns of sea level trend over a similar period in the Pacific are significantly affected by decadal climate variability, and to first order the spatial patterns can be approximated by sea level trends due to aliasing of the decadal variability plus the global mean sea level rise. Finally, we note that the CORE-II simulations generally show

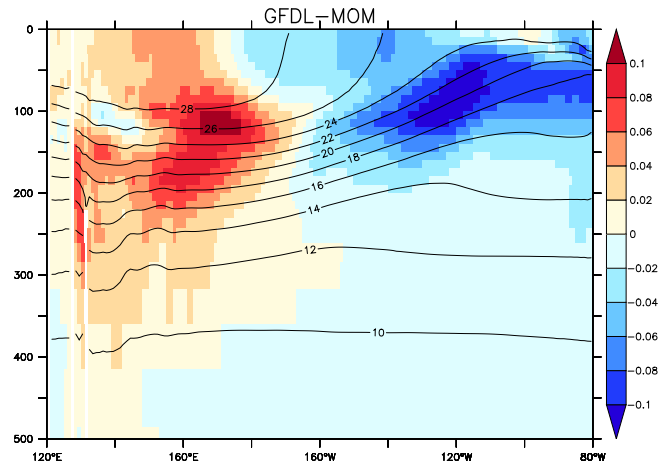


**Fig. 29.** Linear temperature trend along the equator in the Pacific for years 1993–2007 in the GFDL-MOM simulation, shown in units of degrees Celsius per year. The contours show the time mean temperature over years 1993–2007. Note the warming in the west and cooling in the east, with these trends reflected in the thermosteric sea level trends seen in Fig. 26.

a strong negative centre at the eastern Pacific, with the magnitude stronger than in the observations.

## 6. Summary and discussion

Sea level emerges from mechanical and thermodynamic forcing on the ocean boundaries, and is affected by transport and mixing in the ocean interior. Thus, all physical processes impacting the ocean impact sea level, including physical oceanographic processes as well as geophysical processes associated with changes in the earth's gravity and rotation. Sea level is a key field to accurately capture in simulations to assess the potential for climate impacts, particularly in coastal regions. Simulation of both its global mean and regional patterns in turn provides a strong test for numerical model integrity and utility.

In this study, we followed the protocol of the Coordinated Ocean-sea ice Reference Experiments, with details given by Griffies et al. (2009b) and Danabasoglu et al. (2014). These global ocean-sea ice simulations do not include all processes important for sea level (see Slangen et al., 2012 for a more comprehensive approach). Rather, the present study focuses on the global ocean-sea ice climate problem using a prescribed atmospheric state to derive boundary fluxes and with a static gravitational force, fixed land-sea boundaries (i.e., fixed ocean bottom topography). We therefore focused on ocean-centric measures of simulation features, predominantly associated with steric, thermosteric, and halosteric effects.

### 6.1. Why CORE comparisons are useful

The models contributing to this study represent a cross-section of the state-of-the-science configurations used for global ocean and climate studies, with many research groups using ocean-sea ice configurations taken from their companion coupled climate models that contributed to the CMIP5 project (Taylor et al., 2012). Additionally, some of the participating groups are only just now entering the “mainstream” of ocean climate modelling, such as the finite element ocean model from AWI-FESOM.

The various CORE comparison projects (e.g., the present paper as well as Griffies et al. (2009b) and Danabasoglu et al. (2014)) provide a valuable framework for ocean-sea ice climate modelling. One key feature of such projects is the sharing of experience and

knowledge between research groups that is essential for advancing both the model tools and the associated science supported by the simulations. That is, it is deeply valuable to analyze a suite of simulations in a side-by-side manner under well defined experimental conditions such as CORE. Doing so offers a powerful means to expose errors that may otherwise go unnoticed, and to identify robust features of scientific interest. Furthermore, if the present paper and its companions have longevity in the literature, we suggest they will do so largely by detailing analysis methods and model diagnostics of use to characterize ocean climate simulations.

There are reasons to expect the mean of a well sampled model suite to perform better than any individual model, largely due to the cancellation of model errors. We have partial support for this result from Fig. 17 and Table 2, which consider the model dynamic sea level compared to the satellite measures. In the following summary of CORE-II results, we therefore focus on the model ensemble mean as it compares to various observation-based estimates. We weight each model equally. We focus here on a descriptive discussion, particularly given the largely unquantified uncertainties in the observation-based analyses. At this stage, the use of more sophisticated statistical comparison tools is unnecessary.

### 6.2. Summary of global mean heat and global mean sea level

We considered global mean heat content and thermosteric sea level during the first portion of this paper. We raised important caveats in Sections 2.6 and 2.7 regarding the ability of the CORE-II protocol to make assessments of global mean sea level over long time scales. As emphasized by Doney et al. (2007), Large and Yeager (2009, 2012), the CORE-II atmospheric state is designed primarily for studies of interannual ocean variability. Our investigations of multi-decadal time scales supported this restricted use of the CORE-II simulations for global mean sea level studies, prompting us to focus the global mean analysis on the same 1993–2007 period used for regional pattern analysis.

Much of the trend in thermosteric sea level from the CORE-II simulations during 1993–2007 arises from changes in the upper 700 m of ocean (Fig. 8). We exhibit in Fig. 30 the time series for the CORE-II ensemble mean global mean heat content and thermosteric sea level, computed over the upper 700 m. The starting point for the ocean heat content and thermosteric sea level is biased low relative to the observation-based estimates. However, the rate of change is compatible with that estimated by Domingues et al. (2008), yet lower than the rate estimated by Domingues et al. (2008), yet lower than the rate estimated by Levitus et al. (2012). We offered conjectures in Section 2.6 for

why we may expect the CORE-II simulations to be biased low. One reason relates to an insufficient amount of warming found in the CORE-II atmospheric state, as suggested by the smaller rise in global mean SST in the simulations relative to observation-based estimates (Fig. 2). Another reason is related to the use of a repeated 60-year cycle for the CORE-II simulations, which in effect introduces a lag in the ocean response related to the time scale for ocean adjustment to changes in the surface heat fluxes.

There is negligible trend in global mean steric changes between 700 m–2000 m (Fig. 9), with the notable exception being in the high latitudes (Fig. 14). High latitude regions furthermore show widely varying trends for water deeper than 2000 m, due to the differing drifts inherent in simulations that have run for only 300 years. It takes a few thousand years for the deep ocean to reach equilibrium (Stouffer, 2004; Danabasoglu, 2004).

### 6.3. Summary of temperature trend patterns

We considered pattern changes in ocean heat content and temperature in Section 4. Direct comparison to observation-based analyses are available for heat content trends (Fig. 12), or for the related trends in temperature as averaged over the upper 700 m of the ocean. The CORE-II ensemble mean of the depth average temperature change is shown in Fig. 31. We also show the zonal mean of the temperature change in Fig. 14 for the full suite of CORE-II simulations, and the ensemble mean is again shown in Fig. 32.

We highlight here salient features of the linear trend in upper 700 m vertically averaged temperature and zonal mean temperature from the CORE-II ensemble mean as compared to the observation-based analyses.

- PACIFIC: Both CORE-II simulations and observation-based analyses indicate a warming in the west and cooling in the east low to mid-latitude Pacific. CORE-II and Durack and Wijffels (2010) exhibit an eastern cooling that reflects an El Niño Southern Oscillation pattern, whereas the cooling in Domingues et al. (2008) and Levitus et al. (2012) is less distinct. Cooling is found in the South Pacific and into the Southern Ocean in Domingues et al. (2008) and Durack and Wijffels (2010), and marginally in the CORE-II simulations, whereas there is marginal warming in this region in the Levitus et al. (2012) analysis. The CORE-II simulations show a warming in the Kuroshio extension of the North Pacific, yet there is a weaker signal in the observation-based analyses. This discrepancy may be related to an inaccurate rep-

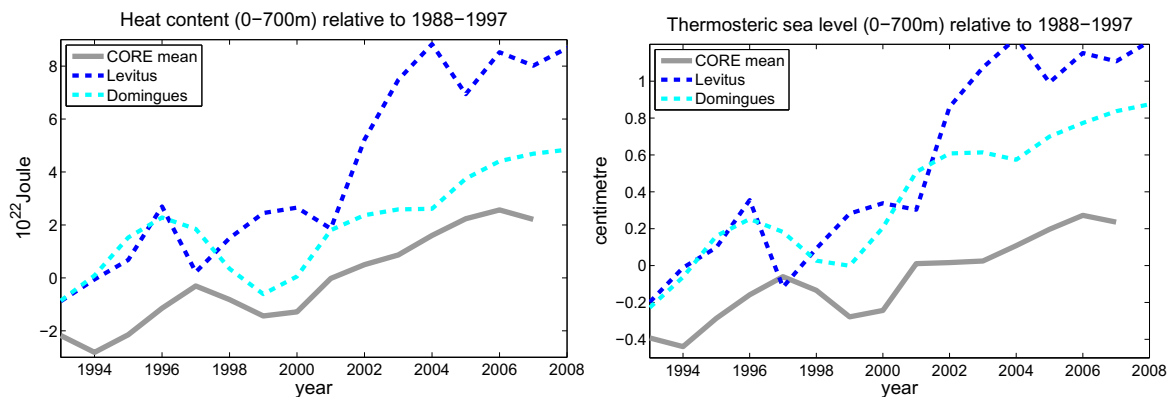


**Fig. 30.** Time series for annual mean ocean heat content and thermosteric sea level integrated over the upper 700 m of ocean, taken from the ensemble mean of the CORE-II simulations and two observation-based analyses. Results from the full model suite are presented in Fig. 8. The warming rate found in the CORE-II simulations is largely compatible with that estimated by Domingues et al. (2008), yet lower than the rate estimated by Levitus et al. (2012).

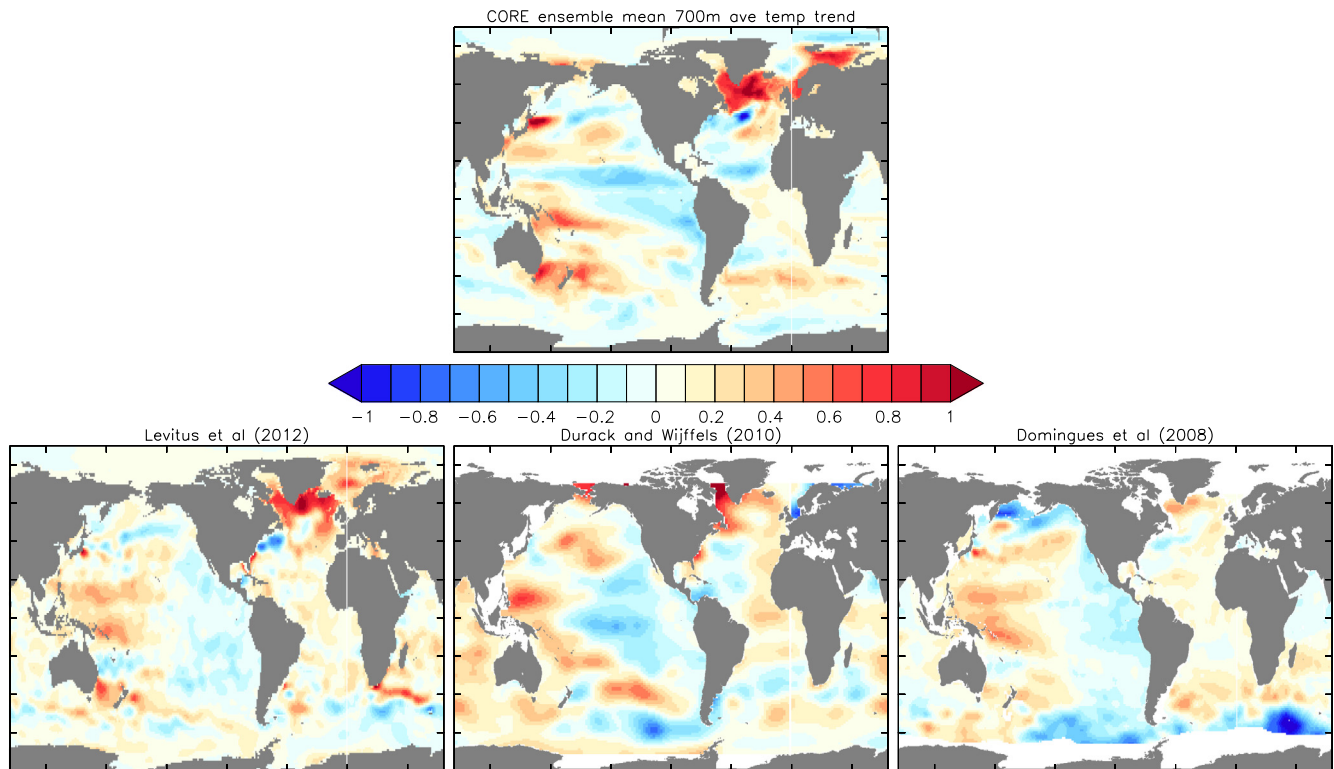


**Fig. 31.** Linear trend in annual mean ocean temperature as vertically averaged over the upper 700 m of ocean (units  $^{\circ}\text{Cdecade}^{-1}$ ) for the years 1993–2007, computed from the ensemble mean of the simulations over the fifth CORE-II cycle. Also shown is the corresponding observation-based trends over years 1993–2007 from [Levitus et al. \(2012\)](#); an updated analysis from [Domingues et al. \(2008\)](#) and [Church et al. \(2010\)](#); along with the trend over years 1990–2010 using an updated version of [Durack and Wijffels \(2010\)](#). This trend is quite similar to that shown in [Fig. 13](#) for the heat content shown there for each of the simulations as well as the CORE-II ensemble mean. The spatial correlation between the CORE ensemble mean and the observational analyses is given by CORE-Levitus = 0.45, CORE-Domingues = 0.33, CORE-Durack = 0.28.

resentation of the Kuroshio in the coarse-resolution CORE-II simulations, where the Kuroshio generally overshoots the correct separation latitude (around  $35^{\circ}\text{N}$ ) and flows northward along the east coast of Japan. Warmer surface waters are in turn carried by the biased Kuroshio during recent years in the simulations.

- **ATLANTIC:** Both CORE-II and observation-based analyses indicate a warming in the subpolar North Atlantic, with the warming found in [Domingues et al. \(2008\)](#) muted relative to the others. The zonal mean changes in [Fig. 32](#) indicate that the North Atlantic warming extends to around 1000–2000 m. The Gulf Stream extension for CORE-II and observation-based analyses show some cooling, with the signal in CORE-II stronger. This cooling is associated with a southward shift of the Gulf Stream during 1993–2007. CORE-II simulations also show some cooling in the near equatorial region, which is largely missing in the observation-based analyses. The South Atlantic is generally warming in CORE-II and observation-based analyses, though CORE-II and [Durack and Wijffels \(2010\)](#) reveal mild cooling in the high latitudes of the South Atlantic.
- **INDIAN:** The observation-based analyses indicate general warming in the Indian Ocean, with [Durack and Wijffels \(2010\)](#) showing the largest, extending through to the Indian Ocean sector of the Southern Ocean. The CORE-II simulations show a marginal cooling, whereas [Domingues et al. \(2008\)](#) and [Levitus et al. \(2012\)](#) show a marginal warming, though note that [Domingues et al. \(2008\)](#) and [Durack and Wijffels \(2010\)](#) show a hint of cooling in the north Arabian Sea.
- **SOUTHERN:** The CORE-II simulations reveal a warming in the South Pacific, South Atlantic, and South Indian ocean, with some cooling to the far south next to Antarctica. The observation-based

analyses generally agree that the region south of Australia is warming, as is the high latitude South Atlantic. However, [Domingues et al. \(2008\)](#) shows a strong cooling in the Indian sector of the Southern Ocean missing from other observation-based analyses and CORE-II, whereas both [Domingues et al. \(2008\)](#) and [Durack and Wijffels \(2010\)](#) show cooling in the South Pacific sector that is marginal at best in the CORE-II simulations and largely missing in [Levitus et al. \(2012\)](#).

We suspect that much of the observation-observation and model-observation ambivalence in the Southern Ocean arises from the relative paucity of *in situ* data and uncertainties in the CORE-II atmospheric state of [Large and Yeager \(2009\)](#).

- **ARCTIC:** The CORE-II simulations suggest a marginal cooling in the Arctic, whereas [Levitus et al. \(2012\)](#) suggests a marginal warming. The other observation-based analyses do not cover the Arctic.
- **ZONAL MEAN:** Besides the deep warming in the North Atlantic for CORE-II, [Levitus et al. \(2012\)](#); and [Durack and Wijffels \(2010\)](#), there is a broad warming in the upper 700 m throughout the ocean. However, there is a patch of cooling in the tropical northern hemisphere found in CORE-II that is marginally present in [Durack and Wijffels \(2010\)](#) but largely absent in [Levitus et al. \(2012\)](#). The CORE-II simulations indicate a marginally cooler Southern Ocean, which contrasts to the marginally warmer analysis from [Levitus et al. \(2012\)](#).

#### 6.4. Summary of dynamic sea level patterns

All of the CORE-II simulations considered here produce a respectable time mean dynamic sea level as compared to the 1993–2007 satellite measurements analyzed by AVISO ([Fig. 15](#)).

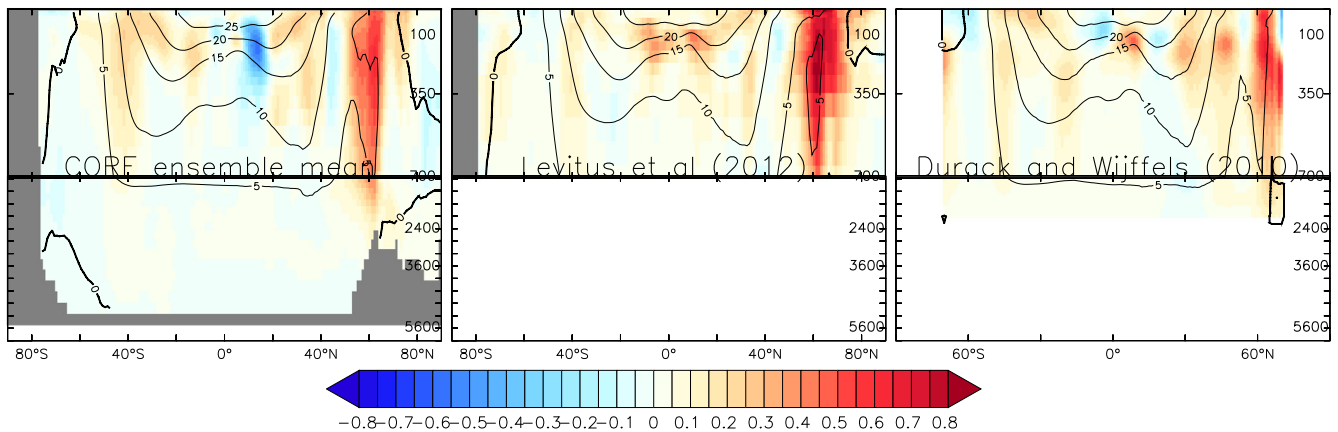


**Fig. 32.** Zonal average of the linear trend in annual mean ocean temperature ( $^{\circ}\text{C decade}^{-1}$ ) for the years 1993–2007 as computed from the CORE-II ensemble mean over the fifth CORE-II cycle. Also shown are two estimates of the observation-based trends. Overlaying the trends are contours for the time mean temperature computed from each respective model and observation-based analysis. The upper 700 m of the ocean is split from the deeper ocean to emphasize changes in the upper ocean. The images are computed by first mapping the 3d model results to a common spherical grid with a common vertical spacing, and then performing the zonal average.

However, consistent with other assessments, such as Lombard et al. (2009) (see their Fig. 2) and Church et al. (2010) (see their Fig. 6.3), the simulations here produce larger differences from satellite measurements in the high latitudes, particularly in the Atlantic basin and Southern Ocean. In general, those regions exhibiting deep water formation, mode water formation, and strong western boundary currents, display larger sea level deviations from satellites (Fig. 16). We suggest that these differences point to limitations of the models associated with the rather complex physical processes associated with mode and deep water formation and boundary currents. We do not have a suite of simulations where only the model resolution is varied, so we cannot make robust statements regarding the ability of refined resolution models to more accurately represent sea level at both the regional and global scales. These would represent an important ongoing aspect of developing models with skill at regional scales. In general, we acknowledge that some differences can arise from processes not simulated in the CORE-II models, such as changes to the gravity field impacting the static equilibrium sea level (Kopp et al., 2010).

As shown in Fig. 18 for the full suite of CORE-II simulations, and summarized in Fig. 33 for just the ensemble mean, the simulations exhibit dynamic sea level trends over the years 1993–2007 that reflect certain features also found in the satellite-based analysis. We highlight here some of the agreements and disagreements.

- **PACIFIC:** The models exhibit a rise in the western Pacific and fall in the eastern Pacific. Mechanisms for these changes in dynamic sea level are consistent with hypotheses put forward in the literature as associated with wind trends (Feng et al., 2010; Bromirski et al., 2011; Merrifield et al., 2012; McGregor et al., 2012; Zhang and Church, 2012) (see Figs. 28 and 29). However, the westward extent and magnitude of the sea level depression in the east is larger in CORE-II than the satellite, perhaps suggesting limitations with the CORE-II wind stress forcing. Both the CORE-II mean and satellite indicate a sea level drop in the North Pacific, extending into the Arctic sector just north of the Bering Strait. Both also indicate a rise in the Kuroshio region of the west Pacific.
- **ATLANTIC:** Both CORE-II and satellites indicate a sea level rise in the subpolar North Atlantic, with these changes associated with a switch in the North Atlantic Oscillation around 1995/1996 and the attendant impact from ocean meridional heat and salt transport into the subpolar region (Häkkinen and Rhines, 2004; Lohmann et al., 2009; Yeager et al., 2012; Danabasoglu et al., 2014). There is an associated dipole pattern in sea level

trends found along the east coast of the US, with recent altimetry and tide gauge data suggesting that the pattern is switching to one with a faster sea level rise north of Cape Hatteras, and slower sea level rise to the south (Yin and Goddard, 2013; Kopp, 2013). These studies suggest that the decadal trend of the dynamic sea level in the North Atlantic is not representative of the long-term, with trends quite different over the years 1993–2002 versus 2003–2012. One should thus keep this point in mind when comparing our results to previous studies.

- **INDIAN:** Both the CORE-II ensemble mean and satellite indicate a sea level rise in the South Atlantic and extending eastward into the South Indian Ocean. The trend in the Indian Ocean extends eastward from Madagascar. However, the satellite measures indicate a sea level fall in the North Indian Ocean during 1993–2007, whereas CORE-II indicates a rise.
- **SOUTHERN OCEAN:** A notable disagreement between models and satellite occurs in the Southern Ocean south of Australia, where the models generally show a decreasing sea level trend whereas the satellite shows a positive trend. This region is also one where the observation-based analysis of thermosteric sea level trends differs (Fig. 34), with Levitus et al. (2012) showing a marginally negative trend whereas Domingues et al. (2008) and Durack and Wijffels (2010) show a positive trend. We suspect that much of the observation-observation and model-observation disagreement in this region arises from the relative paucity of *in situ* data and uncertainties in the CORE-II atmospheric state of Large and Yeager (2009).
- **ARCTIC:** Changes in the Arctic found in the CORE-II simulations are largely associated with halosteric changes, as summarized in Section 6.5. Unfortunately, they are missing from the satellite measurements due to coverage limitations.

### 6.5. Summary of steric sea level patterns

Trends in dynamic sea level can be decomposed into steric and bottom pressure changes, according to the method proposed by Gill and Niiler (1973) (see Eq. (13) as well as Appendix B.1). The dynamic sea level trends from the CORE-II simulations are dominated by steric changes (Fig. 19), with changes in bottom pressure about an order of magnitude smaller (Fig. 20).

Local changes in steric sea level can in turn be decomposed into thermosteric and halosteric changes (Appendix B.1.2). Thermosteric effects (Fig. 22) are generally larger than halosteric effects (Fig. 23), with notable exceptions being the Arctic and subpolar

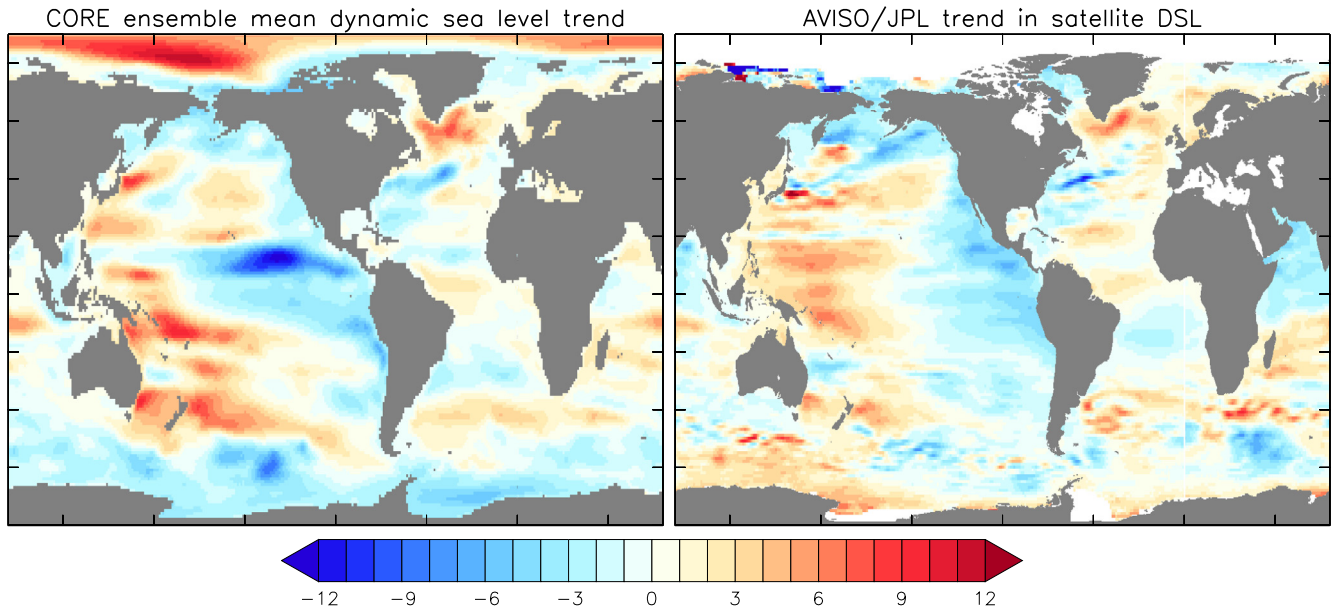


**Fig. 33.** Linear trend in annual mean dynamic sea level ( $\text{mm yr}^{-1}$ ) for the years 1993–2007 as computed from the ensemble mean of the CORE-II simulations over the fifth CORE-II cycle. Also shown are observation-based estimates of the trend based on satellite measurements (between roughly  $60^{\circ}\text{N}$ – $60^{\circ}\text{S}$ ). The JPL sea level field was obtained from AVISO, and downloaded from [podaac.jpl.nasa.gov/dataset/AVISO\\_L4\\_DYN\\_TOPO\\_1DEG\\_1MO](http://podaac.jpl.nasa.gov/dataset/AVISO_L4_DYN_TOPO_1DEG_1MO). The full suite of simulations is presented in Fig. 18. The spatial correlation between the CORE ensemble mean and the satellite analysis is 0.40.

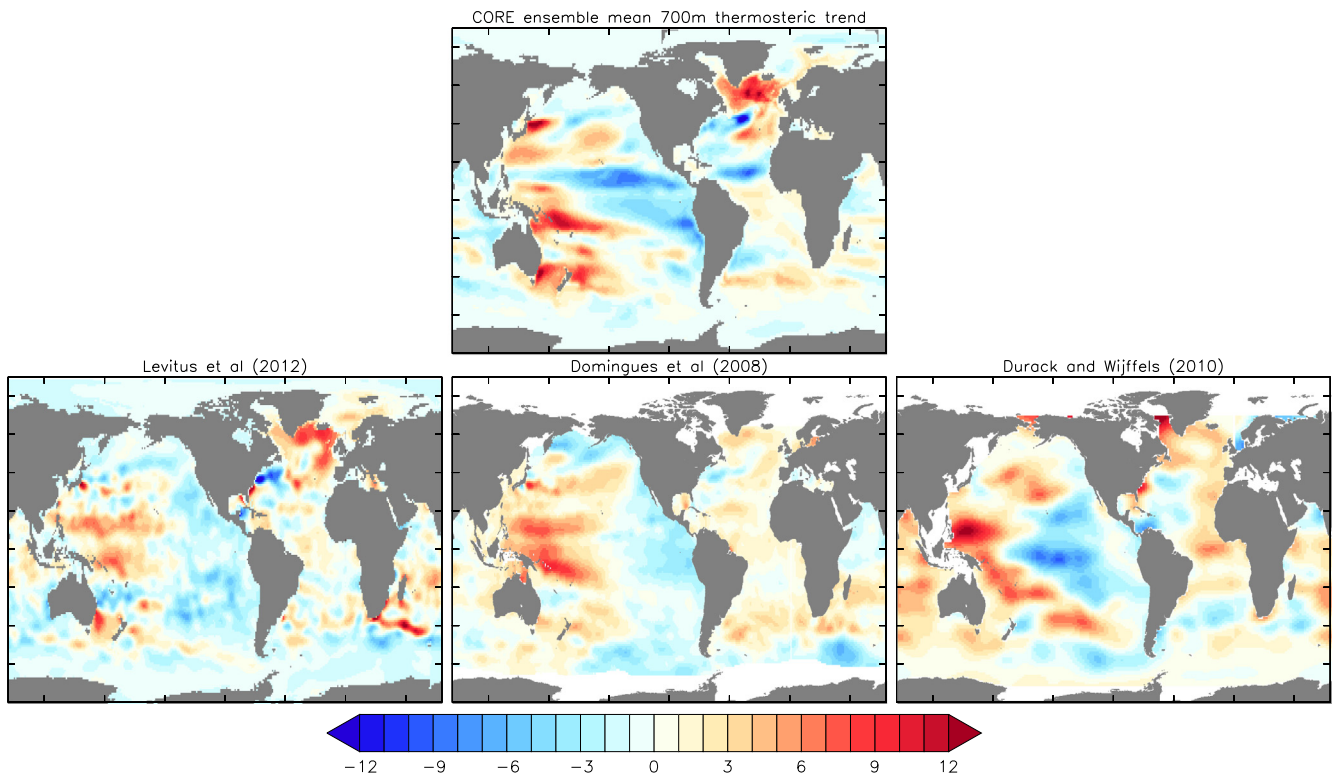


**Fig. 34.** Linear trend ( $\text{mm yr}^{-1}$ ) in thermosteric sea level computed in the upper 700 m of water for years 1993–2007. The model results are taken from the ensemble mean of the 5th CORE-II cycle. Observation-based estimates are shown from Levitus et al. (2012); an updated analysis of Domingues et al. (2008) and Church et al. (2010); and an updated analysis based on Durack and Wijffels (2010). Results from the full suite of CORE-II simulations are shown in Fig. 26. The spatial correlation between the CORE ensemble mean and the observational analyses is given by CORE-Levitus = 0.31, CORE-Domingues = 0.43, CORE-Durack = 0.31.

North Atlantic. We provide a discussion of these patterns in Section 5.3.

When limiting the analysis of steric trends to just the upper 700 m of the ocean, we are able to compare the CORE-II simulations to various observation-based analyses, in addition to the

Durack and Wijffels (2010) analysis that extends to 2000 dbar. As discussed in Section 2.8, the Durack and Wijffels (2010) analysis offers both temperature and salinity trends, and so can render an estimate of trends for steric, thermosteric, and halosteric sea level changes. The Domingues et al. (2008) and Levitus et al. (2012)

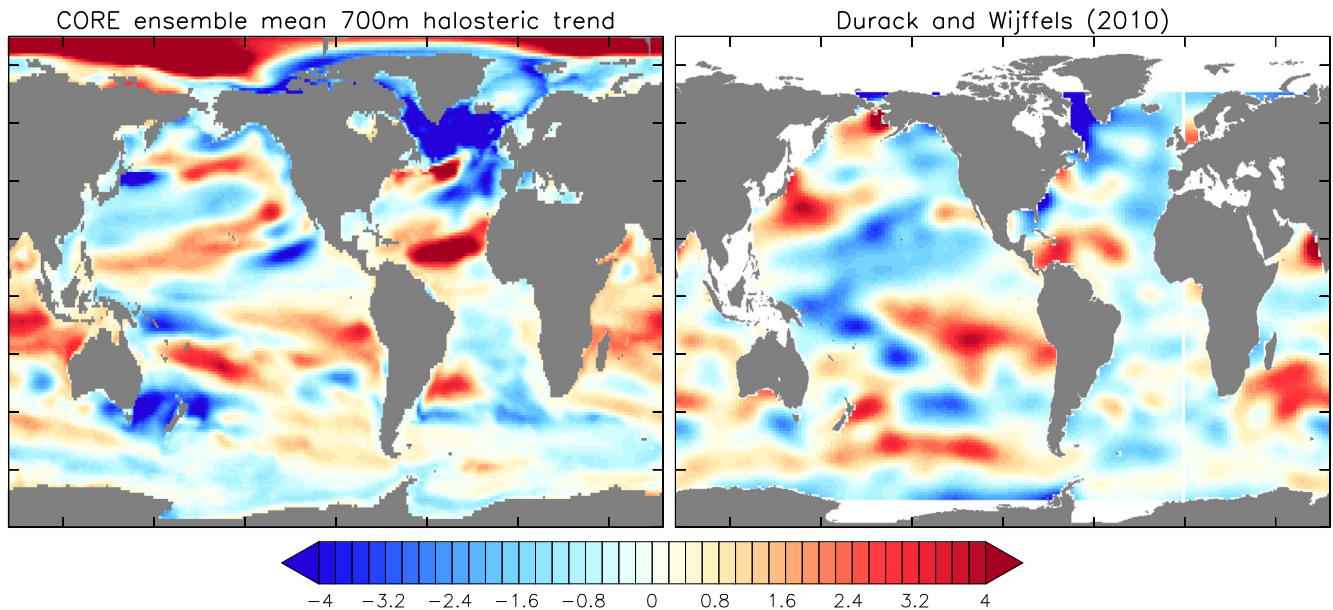


**Fig. 35.** Linear trend ( $\text{mm yr}^{-1}$ ) in halosteric sea level computed in the upper 700 m of water for years 1993–2007. The model results are taken from the ensemble mean of the 5th CORE-II cycle. Observation-based estimates are shown from an updated analysis based on Durack and Wijffels (2010). Results from the full suite of CORE-II simulations are shown in Fig. 27. We exhibit here a smaller color bar range than in other steric trend figures (e.g., Fig. 27) in order to better highlight the patterns. The spatial correlation between the CORE ensemble mean and the Durack and Wijffels (2010) observational analysis is 0.18.

analyses focus on temperature changes, and so allow an estimate only for thermosteric changes. We exhibit results from the full suite of CORE-II simulations in Figs. 25–27. A summary of the results for the thermosteric trends is given in Fig. 34, and halosteric trends in Fig. 35. Discussion of the agreements and disagreements for thermosteric patterns follow largely from those already considered for dynamic sea level in Section 6.4 and temperature trends in Section 6.3.

The halosteric trends are generally sub-dominant to the thermosteric trends, with important exceptions found in the North Atlantic, where they are comparable and counteract the thermal effects, and in the Arctic, where they are the dominant contributor in the CORE-II simulations. Unfortunately, there are no observation-based analyses providing estimates for the Arctic halosteric trends. For the remainder of the ocean, the CORE-II ensemble mean and Durack and Wijffels (2010) analysis suggest rather striking and complex trend patterns. However, many elements of these trend patterns do not agree well. As discussed in Section 3, we are unconvinced that details of the simulated halosteric patterns are physically meaningful since the CORE-II simulations use surface salinity relaxation of varying strength between the models, with such relaxation having no counterpart in the climate system (see Section 3 of Griffies et al., 2009b). This is an unfortunate limitation of the CORE-II design.

#### 6.6. Summary comments regarding CORE-II

Details certainly do differ amongst the suite of models, and we do not presume all details are correct either from the models or from the observation-based analyses. Furthermore, we cannot expect perfect agreement between models and observation-based analyses, particularly given the coarseness in the models, the limitations of the Large and Yeager (2009) CORE-II atmospheric state, the many holes in the observation-based analyses, and the additional processes impacting sea level that are missing from the simulations (e.g., gravitational and rotational effects). Nonetheless, we are satisfied that the CORE-II simulations, particularly in the upper 700 m of the ocean, are responding to the CORE-II atmospheric

state in a consistent manner. Furthermore, the ensemble mean of the CORE-II simulations exhibits trends in both global mean and regional patterns generally within the spread of the observation-based analyses.

Although we answered the questions posed at the start of this paper concerning global mean and regional patterns (Section 1.1), it is difficult to reach the end of an assessment paper such as this without a list of questions longer than at the start. In a nutshell, our assessment is that the CORE-II simulations are not inconsistent, at the larger scales, with a suite of observation-based analyses. Breaking open that nut, however, reveals many facets to the comparison that remain unanswered. Namely, can we explain details of how thermosteric and halosteric patterns differ amongst the models or in comparison to the observations, particularly at the regional scale? One piece required to answer these questions sits with forcing differences. Even though the CORE-II protocol aims to reduce such differences, the open-ended treatment of salinity boundary conditions leads to differences in the halosteric effects. Although halosteric effects were found to be sub-dominant to thermosteric effects in many regions, there are notable exceptions such as in the Arctic, where halosteric effects dominate, and North Atlantic, where they largely compensate for the strong thermosteric rise. We consider the absence of a robust statement about halosteric patterns, particularly in the lower latitudes, to be a notable weakness of the CORE-II protocol.

We suspect that a further key reason for model differences concerns physical and numerical formulations of the various ocean model configurations, with sea ice model differences conjectured to be less important. We note that there are opportunities for parameterization and/or numerical choices within a single model code to contribute to substantial differences in sea level patterns and global mean trends. For example, the NOCS and CERFACS models are based on the same ocean and sea ice model, but differ in ocean physical parameterizations. More generally, studies of vertical ocean mixing, both physically motivated as in MacKinnon et al. (2013) and numerically induced as in Griffies et al. (2000), provide examples where physical parameterizations and numerical choices impact on heat uptake, with attendant impacts on model drift and hence on simula-

tions of sea level. Parameterization and/or representation of meso-scale eddies (Fox-Kemper et al., 2013) also play a potentially important role in determining regional sea level patterns.

We contend that a physical process-based analysis is needed on a model-by-model basis to uncover mechanisms accounting for model differences. Examples include the analysis of Griffies and Greatbatch (2012), who decomposed the global mean sea level budget, as well as that from Palter et al. (2014), who decomposed the local steric sea level budget. Such analyses are nontrivial to perform with a single model. They are logistically even more difficult across a broad suite of models such as considered here. Nonetheless, we expect that significant progress will be made to understand model-model differences only when detailed budget analyses are performed at the level of specific physical processes. We hope that the present paper provides a useful starting point for such studies.

### 6.7. CORE-II, reanalysis, and CMIP

In parallel to the efforts described here focusing on the prognostic CORE-II simulations, the ocean reanalysis community is pursuing comparison studies of sea level, ocean heat content, and ocean salt content in reanalysis products (Storto et al., 2014; Hernandez et al., 2014; Palmer et al., 2014; Alves et al., 2014). As those comparisons mature, an intercomparison between CORE-II and reanalysis products would be a useful means to further constrain the models, assimilation methods, and observations, and to provide physical insight into the ocean climate system. As emphasized in Section 2.5.4, a comparison that renders mechanistic understanding requires the models and assimilation methods to conserve heat and salt.

We furthermore note the potential for more intimate interactions between CORE and CMIP. As discussed in Section 2.1, there are important differences between CORE (coupled ocean/ sea ice models with prescribed atmospheric state) and CMIP (fully coupled climate models). The complementary aspects of the two efforts foster independent questions and methods, all of which supports the scientific value of ocean and climate modelling. However, we contend that more interaction between the two communities would prove of value as well, particularly now that CORE simulations are becoming a *de facto* community standard for vetting global ocean-sea ice models in a manner akin to AMIP (Atmospheric Model Intercomparison Project) (Gates, 1993). Do biases in CORE simulations transfer into coupled climate models using the same ocean and sea ice models as components? Are CORE simulations a necessary and/or sufficient means of benchmarking ocean/ sea ice models used as part of CMIP coupled climate models? Answering these questions requires a new phase in the CORE process, whereby thorough comparisons of model behaviour in “CORE-mode” versus “coupled climate mode” are considered. Preliminary ideas are being contemplated within the community of ocean and climate modellers. We trust that future papers will document results from such deliberations.

### Acknowledgement

The WCRP/CLIVAR Working Group on Ocean Model Development (WGOMD) is responsible for organizing the Coordinated Ocean-sea ice Reference Experiments. The conceptual and technical details associated with global ocean-sea ice model comparisons have comprised the majority of the group’s deliberations since its inception in 1999. We thank Anna Pirani from the CLIVAR staff for her tireless and gracious support of WGOMD activities.

Much of the analysis in this paper made use of the free software package Ferret, developed at NOAA-PMEL. We thank Frank Bryan, Carolina Dufour, Matthew England, Andy Hogg, Robert Kopp, Ange-

lique Melet, and Ron Stouffer for comments and discussions that have greatly helped this paper. We thank Christophe Cassou for comments on the possible effects from wind errors in their relation to biases in equatorial Pacific sea level patterns. Finally, we thank the critical input from three anonymous reviewers.

NCAR is sponsored by the US National Science Foundation. The ACCESS model is supported by the Australian Government Department of the Environment, the Bureau of Meteorology and CSIRO through the Australian Climate Change Science Programme. E. Fernandez was supported by the BNP-Paribas foundation via the PRECLIDE project under the CNRS research convention agreement 30023488. P.J. Durack was supported by the Regional and Global Climate Modeling Program of the U.S. Department of Energy Office of Science, and his research was performed at LLNL under Contract DE-AC52-07NA27344. A.M. Treguier acknowledges support of the European Commission’s 7th Framework Programme, under Grant Agreement number 282672, EMBRACE project. J. Yin and P. Goddard are supported by NOAA CPO under Grant NA13OAR4310128. D.M. Holland was supported by NYU Abu Dhabi grant G1204.

### Appendix A. Global mean sea level

We summarize in this appendix basic elements of the kinematic evolution of the sea surface height (SSH), with particular attention given to how the global mean sea level is impacted by steric effects. There are two basic assumptions made here, consistent with the models considered in this study.

- **CONSTANT GRAVITATIONAL ACCELERATION:** The gravitational acceleration is assumed to be constant in space and time. Hence, the issues associated with changes in the geoid or earth rotation (Mitrovica et al., 2001; Kopp et al., 2010) are ignored.
- **CONSTANT HORIZONTAL AREA OF OCEAN:** The ocean is assumed to have a time independent horizontal area, so that questions of wetting and drying, important for coastal erosion studies and changes to ice shelf grounding lines, are not captured by the ocean models in this study.

#### A.1. Mass continuity and the kinematic evolution of sea level

We start by considering the equation for mass conservation of a fluid parcel

$$\frac{1}{\rho} \frac{d\rho}{dt} = -\nabla \cdot \mathbf{v}, \quad (14)$$

where  $\mathbf{v} = (\mathbf{u}, w)$  is the three dimensional velocity of a fluid parcel,  $\mathbf{u}$  the horizontal component and  $w$  the vertical, and  $d\rho/dt$  is the material time evolution of *in situ* density. Integration of mass conservation over the full depth of an ocean column, with use of the surface ( $z = \eta(x, y, t)$ ) and bottom ( $z = -H(x, y)$ ) kinematic boundary conditions, renders the kinematic sea level equation

$$\frac{\partial \eta}{\partial t} = \frac{Q_m}{\rho(\eta)} - \nabla \cdot \mathbf{U} - \int_{-H}^{\eta} \frac{1}{\rho} \frac{d\rho}{dt} dz. \quad (15)$$

In this equation,  $\eta(x, y, t)$  is the sea surface height (SSH) that measures the height of the ocean free surface above the  $z = 0$  geoid;

$$\mathbf{U} = \int_{-H}^{\eta} \mathbf{u} dz \quad (16)$$

is the vertically integrated horizontal velocity that measures the horizontal volume transport through a column of fluid;  $\rho(\eta) = \rho(x, y, z = \eta(x, y, t), t)$  is the liquid seawater density at the ocean free surface, and  $Q_m$  is the material mass per time per horizontal area entering the ocean through the surface boundary. There has been no dynamical assumption made to derive the sea surface height

Eq. (15). Instead, it follows solely from the kinematics of a mass conserving fluid.

Eq. (15) provides a kinematic partition of SSH evolution into three physical processes:

- **MASS:** boundary fluxes of mass associated with precipitation, evaporation, river runoff, and land ice melt;
- **CURRENTS:** the convergence of vertically integrated currents, which act to redistribute volume without altering the global mean sea level;
- **NON-BOUSSINESQ STERIC:** vertically integrated material changes in the ocean *in situ* density, referred to as the non-Boussinesq steric effect by Griffies and Greatbatch (2012).

When taking a global mean, it is only the mass term and non-Boussinesq steric term that contribute to global mean SSH evolution

$$\partial_t \bar{\eta} = \overline{\left( \frac{Q_m}{\rho(\bar{\eta})} \right)} - \overline{\left( \int_{-H}^{\eta} \frac{1}{\rho} \frac{d\rho}{dt} dz \right)}, \quad (17)$$

where a global area mean is given by

$$\bar{\eta} = \mathcal{A}^{-1} \int_{\text{globe}} \eta \, dA, \quad (18)$$

with horizontal integration over the global ocean surface. The global ocean surface area,  $\mathcal{A} = \int_{\text{globe}} dA$ , is assumed to be constant, and  $dA$  is the horizontal area element (equal in a numerical model to the grid cell horizontal area). Eq. (17) is the form of the global mean sea level equation examined by Griffies and Greatbatch (2012), with their focus on how physical processes impact on the global mean non-Boussinesq steric effect. However, when detailed online diagnostics are not available, it is more practical to employ the alternative partition of global mean SSH evolution as presented in Section A.2.

The non-Boussinesq steric effect arises from the impacts on SSH evolution due to material changes in ocean *in situ* density. In particular, a material reduction in density over the depth of a fluid column leads to an increase in SSH due to the expansion of the water column. This term is dropped when determining the evolution of sea surface height,  $\eta^B$ , in volume conserving Boussinesq ocean simulations, whereby

$$\frac{\partial \eta^B}{\partial t} = \frac{Q_m}{\rho_o} - \nabla \cdot \mathbf{U}. \quad (19)$$

This equation results from volume conservation for a column of Boussinesq fluid, which contrasts to the evolution of SSH given by Eq. (15) arising from mass conservation. The use of volume conserving kinematics in Boussinesq fluids is accurate for many applications of ocean climate modelling, where the relatively small degree of seawater compressibility can be safely ignored for kinematic purposes. For example, the large-scale patterns of SSH from both volume conserving and mass conserving ocean models is quite similar (e.g., see Fig. 3 in Griffies and Greatbatch (2012)). However, it is through the non-Boussinesq steric effect that global mean SSH rises through ocean warming (Greatbatch (1994)). Griffies and Greatbatch (2012) detail a global adjustment to the Boussinesq SSH that renders it more consistent with the non-Boussinesq SSH (see their Appendix D), with a summary provided here in Section A.3.

## A.2. Global steric effects and the evolution of global mean sea level

The global ocean liquid seawater mass is given by

$$\mathcal{M} = \int dA \int_{-H}^{\eta} \rho dz, \quad (20)$$

and the corresponding expression for the global ocean volume is

$$\mathcal{V} = \int dA \int_{-H}^{\eta} dz = \int (H + \eta) dA, \quad (21)$$

so that the global mean *in situ* seawater density is

$$\langle \rho \rangle = \frac{\mathcal{M}}{\mathcal{V}}. \quad (22)$$

Time evolution of the global ocean mass is thus written as

$$\partial_t \mathcal{M} = \langle \rho \rangle \partial_t \mathcal{V} + \mathcal{V} \partial_t \langle \rho \rangle. \quad (23)$$

The global ocean mass changes due to the input of mass through the ocean boundaries, so that

$$\partial_t \mathcal{M} = \mathcal{A} \overline{Q_m}, \quad (24)$$

where  $\overline{Q_m}$  is the global area mean surface mass flux. The global ocean volume changes due to changes in the global mean ocean free surface (assuming the ocean bottom remains constant)

$$\partial_t \mathcal{V} = \mathcal{A} \partial_t \bar{\eta}. \quad (25)$$

Use of these expressions in the mass budget (23) thus leads to an evolution equation for the global mean sea level

$$\partial_t \bar{\eta} = \frac{\overline{Q_m}}{\langle \rho \rangle} - \frac{\mathcal{V}}{\mathcal{A}} \left( \frac{1}{\langle \rho \rangle} \frac{\partial \langle \rho \rangle}{\partial t} \right). \quad (26)$$

As expected, if the global mean *in situ* density decreases, the global mean sea level rises. We refer to the term

$$\left( \frac{\partial \bar{\eta}}{\partial t} \right)^{\text{global steric}} \equiv - \frac{\mathcal{V}}{\mathcal{A}} \left( \frac{1}{\langle \rho \rangle} \frac{\partial \langle \rho \rangle}{\partial t} \right) \quad (27)$$

as the global steric contribution to global mean sea level evolution. This term is absent from the evolution of the prognostic sea level in Boussinesq ocean models (Greatbatch, 1994). Appendix D in Griffies and Greatbatch (2012) detail some straightforward adjustments required to measure global mean sea level in Boussinesq models, with salient points also provided in Section A.3 below.

Eq. (26) is more convenient for model comparison diagnostics than the alternative Eq. (17). The reason is that it is more convenient to work with time tendencies of global mean density, which is readily computed from model output, than the global mean of the material time change, which requires more terms than generally available from model output. Hence, we make use of the evolution Eq. (26) in our studies of the CORE-II simulations in Section 3.

## A.3. Approximations for diagnosing global mean sea level changes in CORE-II simulations

Although there are exceptions, the CORE-II simulations considered in this paper are designed to have a zero net mass/volume flux crossing the ocean surface (Griffies et al., 2009b). The one exception is the relatively small exchanges associated with sea ice melt and formation, with such phase changes leaving the effective global mean sea level unchanged, as a result of the inverse barometer response of the liquid ocean to sea ice loading (see Appendix C2 in Griffies and Greatbatch (2012)). Hence, global mean sea level for our purposes changes only through changes in global mean seawater density, in which case Eq. (26) takes the form

$$\partial_t \bar{\eta} = - \frac{\mathcal{V}}{\mathcal{A}} \left( \frac{1}{\langle \rho \rangle} \frac{\partial \langle \rho \rangle}{\partial t} \right). \quad (28)$$

This continuous time relation is approximated by

$$\bar{\eta}(t) - \bar{\eta}(t-1) \approx - \left( \frac{\mathcal{V}(0)}{\mathcal{A} \langle \rho(0) \rangle} \right) (\langle \rho(t) \rangle - \langle \rho(t-1) \rangle), \quad (29)$$

in which time evolution is computed as a finite difference, and where  $\langle \rho(0) \rangle$  is the initial global ocean seawater *in situ* density, and  $\mathcal{V}(0)$  is the initial global ocean volume. The diagnostics presented in this paper use annual means for the global mean *in situ* density. Sensitivity to this time average has been found to be negligible with tests using the GFDL-MOM configuration.

#### A.4. Global mean ocean temperature

Globally integrated ocean heat content (SI units of Joules) is given by

$$\mathcal{H} = C_p^0 \mathcal{V} \langle \rho \Theta \rangle = C_p^0 \mathcal{M} \langle \Theta \rangle^\rho, \quad (30)$$

where

$$\langle \Theta \rangle^\rho = \frac{\langle \rho \Theta \rangle}{\langle \rho \rangle} \quad (31)$$

introduces a density weighted mean temperature. Note that the *in situ* density weighting in these equations reduces, for a Boussinesq fluid, to a constant reference density  $\rho_o$  weighting. The specific heat capacity of sea water,  $C_p^0$ , is assumed to be constant here for the various models. However, as noted by McDougall (2003) (see also IOC et al., 2010), use of a constant specific heat capacity is accurately justified only when the temperature variable is the conservative temperature rather than the commonly used potential temperature.

It follows from the definition (30) that the total ocean heat changes according to changes in the mean temperature and the ocean mass

$$\frac{\partial_t \mathcal{H}}{\mathcal{H}} = \frac{\partial_t \langle \Theta \rangle^\rho}{\langle \Theta \rangle^\rho} + \frac{\partial_t \mathcal{M}}{\mathcal{M}}. \quad (32)$$

As heat (or more correctly potential enthalpy) is a conserved quantity in the ocean (McDougall, 2003), we know that the net ocean heat changes only via the net heat flux crossing the liquid ocean surface, in which we write

$$\partial_t \mathcal{H} = \mathcal{A} \overline{Q^{\text{heat}}}. \quad (33)$$

The term  $\mathcal{A} \overline{Q^{\text{heat}}}$  is the area integrated boundary heat flux (SI units of Watts). This heat flux includes the surface fluxes from shortwave, longwave, latent, and sensible heating, as well as exchanges with sea ice (see Section 3.4.1 of Griffies and Greatbatch (2012)). Some models also include geothermal heating. We denote the sum of these terms the non-advective heat flux,  $Q_{\text{non-advect}}^{\text{heat}}$ . In addition, the ocean heat content changes when mass is exchanged, since the mass will carry a nonzero heat across the ocean boundary, so that the total heat flux is the sum

$$Q^{\text{heat}} = Q_{\text{non-advect}}^{\text{heat}} + Q_{\text{advect}}^{\text{heat}}. \quad (34)$$

The advective surface heat flux for CORE simulations is typically approximated by

$$Q_{\text{advect}}^{\text{heat}} \approx Q_m C_p^0 T_{\text{sst}}, \quad (35)$$

where  $C_p^0$  is the ocean heat capacity,  $Q_m$  is the mass transport across the ocean boundary, and  $T_{\text{sst}}$  is the sea surface *in situ* temperature. If  $Q_{\text{advect}}^{\text{heat}}$  is not diagnosed online with each time step, it is of sufficient accuracy for CORE diagnostics to estimate it with the monthly mean mass flux multiplying the monthly mean sea surface temperature. Use of annual means to approximate  $Q_{\text{advect}}^{\text{heat}}$  is not accurate due to the importance of the seasonal cycle. In the real climate system, evaporation generally leaves the ocean in regions of warmer sea surface temperature than precipitation, thus leading to a negative area mean  $Q_{\text{advect}}^{\text{heat}}$ . In the coupled model study of Delworth et al.

(2006) (see their Section 3), they find  $Q_{\text{advect}}^{\text{heat}} \approx -0.15 \text{ W m}^{-2}$ . For the CORE-II simulations considered here,

$$Q_{\text{advect}}^{\text{heat}} \approx -0.3 \text{ W m}^{-2}. \quad (36)$$

Finally, we note that those models that use a virtual salt flux rather than a real water flux (see Table 1) necessarily have

$$Q_{\text{advect}}^{\text{heat}} = 0 \quad \text{if } Q_m = 0. \quad (37)$$

Substitution of Eqs. (33) and (24) into Eq. (32) leads to an expression for the evolution of global mean ocean temperature

$$\frac{\partial_t \langle \Theta \rangle^\rho}{\langle \Theta \rangle^\rho} = \mathcal{A} \left( \frac{\overline{Q^{\text{heat}}}}{\mathcal{H}} - \frac{\overline{Q_m}}{\mathcal{M}} \right). \quad (38)$$

Use of expression (30) for the heat content leads to

$$\frac{\partial_t \langle \Theta \rangle^\rho}{\partial_t} = \frac{\mathcal{A}}{C_p \mathcal{M}} \left( \overline{Q^{\text{heat}}} - C_p \langle \Theta \rangle^\rho \overline{Q_m} \right). \quad (39)$$

Finally, we substitute the advective heat flux (35) to render

$$\frac{\partial_t \langle \Theta \rangle^\rho}{\partial_t} = \frac{\mathcal{A}}{C_p \mathcal{M}} \left( \overline{Q_{\text{non-advect}}^{\text{heat}}} + C_p \overline{Q_m \Theta_{\text{sst}}} - C_p \langle \Theta \rangle^\rho \overline{Q_m} \right). \quad (40)$$

It remains very accurate for global models to set the mass term  $\mathcal{M}$  to a constant, since its relative change is tiny. For those CORE simulations where the global mean ocean mass flux is nonzero only due to exchanges with sea ice, the term  $C_p \langle \Theta \rangle^\rho \overline{Q_m}$  is far smaller than the non-advective and advective heat fluxes  $\overline{Q_{\text{non-advect}}^{\text{heat}}} + C_p \overline{Q_m \Theta_{\text{sst}}}$ .

#### A.5. Global mean sea level and global mean boundary heating

Global mean steric sea level is dominated by global mean temperature, with this dominance understood by considering how global mean density evolves. For this purpose, recall the *in situ* density is a function of temperature (potential or conservative temperature are used in ocean models), salinity, and pressure

$$\rho = \rho(\Theta, S, p). \quad (41)$$

We assume that the time evolution of global mean density can be written (we comment on this assumption at the end of the section)

$$\partial_t \ln(\rho) = -\alpha_{\text{bulk}} \partial_t \langle \Theta \rangle^\rho + \beta_{\text{bulk}} \partial_t \langle S \rangle^\rho + \frac{\partial_t \langle p \rangle^\rho}{(\rho c^2)_{\text{bulk}}}. \quad (42)$$

This expression is only approximate, due to nonlinearities in the equation of state. We consider it to be a physically relevant expression if the linear expansion coefficients correspond to physically relevant values for a bulk thermal expansion coefficient ( $\alpha_{\text{bulk}}$ ), haline contraction coefficient ( $\beta_{\text{bulk}}$ ), and density times the squared sound speed ( $(\rho c^2)_{\text{bulk}}$ ).

For the majority of the CORE-II simulations considered in this paper, the liquid ocean salt content is nearly constant since the only exchanges are associated with either melting and freezing of sea ice, or through the surface salinity restoring, which is normalized to zero globally in most of the simulations. Since the ocean mass is also nearly constant, changes in the global mean salinity are negligible. Pressure effects in Eq. (42) are likewise relatively small. The reason is that in a hydrostatic fluid, pressure at a depth equals to the mass per horizontal area of liquid above that depth. So unless there is a systematic rearrangement of mass in the ocean, we expect the horizontal area averaged pressure at each depth to remain roughly unchanged, thus leading to global averaged pressure remaining roughly unchanged. Fig. 36 exhibits the terms appearing in Eq. (42) for the GFDL-MOM simulation, thus verifying the above emphasis on mean temperature evolution for determining global mean sea level changes due to steric effects.

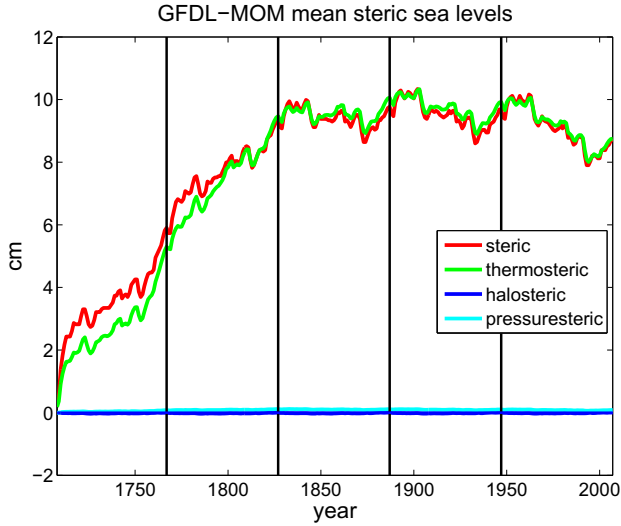


**Fig. 36.** Time series for the global mean sea level from the GFDL-MOM simulation for the five cycles of the CORE-II simulations. We also exhibit the three contributions to this time series from the global mean potential temperature (with  $\alpha_{\text{bulk}} = 1.9 \times 10^{-4} \text{ C}^{-1}$ ), global mean salinity (with  $\beta_{\text{bulk}} = 7.5 \times 10^{-5} \text{ psu}^{-1}$ ), and global mean pressure (with  $(\rho c^2)_{\text{bulk}} = 2.35 \times 10^9 \text{ kg m}^{-1} \text{ s}^{-2}$ ), according to Eq. (42). The bulk parameters were not formally optimized. As expected, the global mean sea level tracks quite closely to the global mean temperature, whereas salinity and pressure contributions are negligible. The vertical lines denote the start of a new 60 year cycle. We date the first cycle as starting at year 1708 to allow for a continuous time series over the five cycles completed at year 2007.

We conclude that for our purposes, the global mean density changes are dominated by global mean potential or conservative temperature changes. Correspondingly, the global mean steric sea level Eq. (28) takes on the approximate form

$$\frac{\partial \bar{\eta}}{\partial t} \approx \left( \frac{\nu \alpha_{\text{bulk}}}{\mathcal{A}} \right) \frac{\partial \langle \Theta \rangle^p}{\partial t}. \quad (43)$$

Eq. (40) relates the mean temperature evolution to surface mass and heat fluxes. Focusing on the heat fluxes, and using (30) for the global mean heat content, renders

$$\frac{\partial \bar{\eta}}{\partial t} \approx \left( \frac{\alpha_{\text{bulk}}}{C_p \langle \rho \rangle} \right) \overline{Q^{\text{heat}}}. \quad (44)$$

This expression, though approximate, provides a useful guide for how global mean sea level evolves as a function of boundary fluxes. We identify the bulk thermal expansion coefficient,  $\alpha_{\text{bulk}}$ , as the measure for how efficient surface ocean heating is for changing global mean sea level. A warmer ocean generally has a larger  $\alpha_{\text{bulk}}$  (Fig. 1), in which case surface heating increases sea level more efficiently than for a cooler ocean. This increased efficiency is also reflected by a reduction in the global mean density  $\langle \rho \rangle$  appearing in the denominator of Eq. (44). To garner an order of magnitude estimate, assume the bulk thermal expansion coefficient to be  $\alpha_{\text{bulk}} \approx 1.54 \times 10^{-4} \text{ K}^{-1}$  (i.e., the global mean from Fig. 1), and set  $\langle \rho \rangle = 1035 \text{ kg m}^{-3}$  (an estimate for the global mean density). In this case, a global mean heat flux of  $\overline{Q^{\text{heat}}} = 1 \text{ W m}^{-2}$  yields a thermosteric sea level rise of roughly  $1.2 \text{ mm yr}^{-1}$ .

The above considerations have proven to be quite useful for many purposes of global mean sea level analyses, largely due to the good agreement seen in Fig. 36 between the evolution of global mean temperature and global mean sea level. However, there are disparities in Fig. 36. It is thus useful to consider cases where Eq. (42) fails. One reason this equation fails in principle is due to nonlinearities in the equation of state. To see how, consider a case in

which global mean temperature, salinity, and pressure remain constant. According to Eq. (42), global mean density should also remain constant. However, if ocean transport processes (i.e., advection and diffusion) redistribute temperature into regions of differing thermal expansion, then global mean density will change. Global mean sea level will thus change through global steric effects, yet without a global thermosteric effect. Apparently this counter-example to the utility of Eq. (42) is not a leading order effect. However, it may be important locally.

## Appendix B. Regional patterns of sea level

We discuss in this appendix rudiments of how dynamical processes are associated with regional patterns of sea level. A full accounting of this topic requires a textbook on ocean dynamics. Our aim is far more modest. Much of the material here borrows from the more thorough discussions in Greatbatch (1994), Mellor and Ezer (1995), Huang and Jin (2002) and Lowe and Gregory (2006). Furthermore, a summary of how wave phenomena (e.g., Rossby and Kelvin waves), as well as currents and mesoscale eddies, reflect on sea level measured from altimeters can be found in the review by Fu et al. (2001).

Throughout this appendix we make the dynamical assumption that the fluid maintains a hydrostatic balance (as do all of the models in this study), so that pressure at a depth  $z \leq \eta$  is given by

$$p(z) = p_a + g \int_z^\eta \rho dz', \quad (45)$$

where  $p_a$  is pressure applied at the ocean surface, presumably from atmosphere or sea ice loading. This balance provides an expression for the pressure in terms of the weight per area of seawater. The weight of fluid is a function of the amount of fluid, which is proportional to the sea level. We may thus employ the hydrostatic balance to deduce relations between the sea level, ocean density, and ocean mass.

### B.1. Temporal sea level fluctuations related to mass and density fluctuations

The hydrostatic balance (45) leads to the expression for bottom pressure

$$p_b = p_a + g \int_{-H}^\eta \rho dz. \quad (46)$$

Taking the time derivative and rearranging leads to

$$\underbrace{\frac{\partial \eta}{\partial t}}_{\text{sea level tendency}} = \underbrace{\frac{1}{g \langle \rho \rangle (\eta)} \left( \frac{\partial (p_b - p_a)}{\partial t} \right)}_{\text{mass tendency}} - \underbrace{\frac{1}{\langle \rho \rangle (\eta)} \left( \int_{-H}^\eta \frac{\partial \rho}{\partial t} dz \right)}_{\text{local steric tendency}}. \quad (47)$$

This decomposition of sea level tendency, first analyzed by Gill and Niiler (1973), relates temporal fluctuations in sea level to fluctuations in seawater mass per horizontal area within an ocean column (i.e., the difference between bottom pressure and applied surface pressure) and to fluctuations in density integrated over the column (i.e., the local steric effect). In simple terms, it relates the changes in ocean volume to changes in ocean mass and changes in ocean density. The mass tendency is associated with barotropic motions, and for a mass-conserving hydrostatic fluid it takes the form

$$\frac{1}{g} \left( \frac{\partial (p_b - p_a)}{\partial t} \right) = -\nabla \cdot \mathbf{U}^p + Q_m, \quad (48)$$

where  $-\nabla \cdot \mathbf{U}^p$  is the convergence of the vertically integrated horizontal mass transport,

$$\mathbf{U}^p = \int_{-H}^\eta \rho \mathbf{u} dz, \quad (49)$$

and  $Q_m$  is the mass flux crossing the ocean boundary. The density term in Eq. (47) arises from changes in the density integrated over the depth of the water column.

Landerer et al. (2007b,a), Yin et al. (2009) and Yin et al. (2010a) made use of the balance (47) to help interpret simulated sea level patterns seen as the ocean warms in climate model simulations. We conduct a similar analysis in Section 5. Namely, as heating penetrates a water column, the amplitude of local steric sea level rise will be greater for deeper columns because there is more water to absorb a greater quantity of heat. Hence, there is an associated dynamic topography gradient next to continental shelf regions, with low dynamic topography on the shelves and high dynamic topography in the deeper ocean. Dynamic topography gradients lead, through dynamical adjustments, to modifications in ocean currents. Without rotation, water will move onto the shelves, thus increasing mass and hence bottom pressure on the shelves, and decreasing bottom pressure in the adjacent deeper ocean. Rotation and hence geostrophic adjustment will modify this tendency to pile up mass on the shelves, as will boundary friction associated with interactions with topography.

Another way to present the above argument follows from noting that the relative change in mass of a fluid column is given by the sum of the relative change in volume and the relative change in density

$$\frac{\delta M}{M} = \frac{\delta V}{V} + \frac{\delta \rho}{\rho}. \quad (50)$$

Now assume that the relative change in density is uniform throughout the seawater column. A change in sea level, such as through uniform heating, will change volume,  $\delta V > 0$ . The relative volume change,  $\delta V/V$ , will be larger in the shallow ocean where  $V$  is small. Correspondingly, the relative change in mass for a seawater column is larger in the shallow ocean, such as on continental shelves, than the deep ocean. Gregory et al. (2013) made use of this argument when discussing the associated implications of the mass redistributions on the gravitational self-attraction and loading.

#### B.1.1. A note about certain linearized free surface methods

Many ocean models employ a linear free surface, such as in the papers from Killworth et al. (1991) and Dukowicz and Smith (1994). In some implementations of these models, the free surface is not felt by the budgets for tracer in the top model grid cell. Hence, the upper limit on the density integral in the hydrostatic balance (46) is set to  $z = 0$  rather than  $z = \eta$ . A time derivative of this approximate hydrostatic balance leads to a balance between column mass and steric effects

$$\frac{\partial(p_b - p_a)}{\partial t} = g \int_{-H}^0 \frac{\partial \rho}{\partial t} dz \quad \text{some linear free surface models.} \quad (51)$$

Note that the linear free surface from Roulet and Madec (2000) correctly includes the  $\partial \eta / \partial t$  term as in Eq. (47), yet this term is omitted in models based on the Dukowicz and Smith (1994) method. Models that maintain the balance (51) can diagnose terms appearing in the physically correct balance (47) by including the extra contribution to the vertical integrals when computing both the bottom pressure and the steric tendency.

#### B.1.2. Local steric contributions to sea level changes

A question often asked in association with anthropogenic ocean warming is how trends in water mass properties impact sea level (e.g., Lowe and Gregory, 2006; Landerer et al., 2007b; Yin et al., 2010a). In general, sea level trends are impacted by changes in bottom pressure as well as changes in *in situ* density, with Eq. (47) the fundamental relation for a hydrostatic fluid. As a means to partially

address the question, we may diagnose how temperature and salinity changes alter the *in situ* density, and so focus just on the density tendency (the local steric term) in Eq. (47).

To introduce the algorithm for computing steric trends in sea level, we discretize the time tendency of density according to

$$\Delta \tau \partial_t \rho \approx \rho(\tau + \Delta \tau) - \rho(\tau) \quad (52)$$

where  $\tau > 0$  is the time after the initial condition and  $\Delta \tau$  is the time step. Expanding the right hand side in a Taylor Series in terms of the density derivatives due to conservative/potential temperature, salinity, and pressure, and truncating to the leading terms in the expansion, yields

$$\begin{aligned} \rho(\tau + \Delta \tau) - \rho(\tau) &\approx \frac{\partial \rho}{\partial \theta} [\theta(\tau + \Delta \tau) - \theta(\tau)] + \frac{\partial \rho}{\partial S} [S(\tau + \Delta \tau) - S(\tau)] \\ &+ \frac{\partial \rho}{\partial p} [p(\tau + \Delta \tau) - p(\tau)] \approx \rho[\theta(\tau + \Delta \tau), S(\tau), p(\tau)] \\ &- \rho[\theta(\tau), S(\tau), p(\tau)] + \rho[\theta(\tau), S(\tau + \Delta \tau), p(\tau)] - \rho[\theta(\tau), S(\tau), p(\tau)] \\ &+ \rho[\theta(\tau), S(\tau), p(\tau + \Delta \tau)] - \rho[\theta(\tau), S(\tau), p(\tau)]. \end{aligned} \quad (53)$$

The steric sea level change over a single time step is then defined by the vertical integral

$$\eta^{\text{steric}}(\tau + \Delta \tau) = \eta(\tau) - \frac{1}{\rho_o} \sum dz [\rho[\theta(\tau + \Delta \tau), S(\tau + \Delta \tau), p(\tau + \Delta \tau)] - \rho[\theta(\tau), S(\tau), p(\tau)]]. \quad (54)$$

Iterating on this expression leads to the steric sea level at an arbitrary time step as a function of the initial time, which defines a reference state

$$\eta^{\text{steric}}(\tau) = \eta(\tau^r) - \frac{1}{\rho_o} \sum dz [\rho(\theta, S, p) - \rho(\theta^r, S^r, p^r)], \quad (55)$$

where the three dimensional conservative/potential temperature, salinity, and pressure  $(\theta^r, S^r, p^r)$  define the properties of the reference state. An analogous expression holds for the thermosteric sea level, defined by

$$\eta^{\text{thermosteric}}(\tau) = \eta(\tau^r) - \frac{1}{\rho_o} \sum dz [\rho(\theta, S^r, p^r) - \rho(\theta^r, S^r, p^r)], \quad (56)$$

the halosteric sea level, defined by

$$\eta^{\text{halosteric}}(\tau) = \eta(\tau^r) - \frac{1}{\rho_o} \sum dz [\rho(\theta^r, S, p^r) - \rho(\theta^r, S^r, p^r)], \quad (57)$$

and the pressure-steric sea level, defined by

$$\eta^{\text{pressure-steric}}(\tau) = \eta(\tau^r) - \frac{1}{\rho_o} \sum dz [\rho(\theta^r, S^r, p) - \rho(\theta^r, S^r, p^r)]. \quad (58)$$

Again,  $\eta(\tau^r)$  is the sea level at the reference state, and  $\rho_o$  is a globally constant reference density. We may alternatively choose the reference density to equal  $\rho(\theta^r, S^r, p^r)$ , in which case it is brought inside the vertical integral. Although only leading to a trivial difference in the patterns, we prefer to use  $\rho_o$  as it relates to the simplified version of Eq. (47) considered in Section 5 (see Eq. (13)). Either way,  $\eta^{\text{thermosteric}}$  partitions the impact on sea level due to temperature changes,  $\eta^{\text{halosteric}}$  does so for salinity changes,  $\eta^{\text{pressure-steric}}$  does so for pressure changes, and  $\eta^{\text{steric}}$  includes all effects.

Notably, the pressure-steric term  $\eta^{\text{pressure-steric}}$  is largely subdominant, so that the steric changes in Eq. (54) are largely described by the sum of  $\eta^{\text{thermosteric}}$  and  $\eta^{\text{halosteric}}$ . Even so, in some cases there is partial compensation (i.e., cancellation) between thermosteric and halosteric effects, such as in the Atlantic where warm salty waters accumulate in the abyssal regions under global warming scenarios (see Section 5). Finally, we note that the truncation used to derive the expansion (53) has been found to hold reasonably well for the CORE-II simulations analyzed in this paper.

That is, the steric sea level trends shown in Fig. 19 are largely equal to the sum of the thermosteric trends in Fig. 22 and the halosteric trends in Fig. 23.

It may also be of interest to determine the depth range over which the dominant local steric changes appear, such as in the study of Chang et al. (2010). Correspondingly, steric sea level changes are best estimated from the observational record over just the upper 700 m of ocean, and only for thermosteric effects. We thus may choose to consider the steric sea level as defined above, but only for a portion of the ocean column. Fig. 26 shows the patterns for 700 m thermosteric changes and compares to various observation-based analyses. We may also wish to determine the full depth dependence of the steric sea level changes, as averaged horizontally over the globe, with Figs. 5–7 showing the steric, thermosteric, and halosteric contributions to global mean sea level as a function of depth and time.

We based our diagnostic calculations of the steric sea level patterns shown in Section 5 on the annual mean conservative/potential temperature, salinity, and depth/pressure from the simulations. The *in situ* density was computed using the same equation of state for all models to evaluate the various density terms in equations (56)–(58). We performed this diagnostic calculation using model temperature and salinity mapped to depth or pressure levels. We are unaware of how to perform this decomposition using results on isopycnal layers.

### B.2. Sea level gradients related to mass and density gradients

We now apply a horizontal gradient to the bottom pressure Eq. (46), which leads to the following expression for the horizontal gradient of sea level

$$\rho(\eta) \nabla \eta = g^{-1} \nabla (p_b - p_a) - \rho(-H) \nabla H - \int_{-H}^{\eta} \nabla \rho \, dz, \quad (59)$$

where  $\rho(-H) = \rho(x, y, z = -H(x, y), t)$  is seawater density at the ocean bottom. The horizontal gradient of sea level is thus decomposed into a horizontal gradient of the mass in a fluid column, the gradient of bottom topography, and the vertically integrated horizontal gradient of density. To simplify this expression, approximate the surface and bottom density as a constant reference density to write

$$\nabla \eta \approx \frac{1}{g \rho_o} \nabla (p_b - p_a) - \nabla H - \frac{1}{\rho_o} \int_{-H}^{\eta} \nabla \rho \, dz. \quad (60)$$

Much of the horizontal variations in bottom pressure arise from changes in ocean bottom topography. To remove this piece, consider bottom pressure variations relative to a static background bottom pressure  $\rho_o g H$ . Writing

$$p_b = \rho_o g H + p'_b \quad (61)$$

renders

$$\nabla \eta \approx \frac{1}{g \rho_o} \nabla (p'_b - p'_a) - \frac{1}{\rho_o} \int_{-H}^{\eta} \nabla \rho' \, dz, \quad (62)$$

where  $\rho = \rho' + \rho_o$ , and  $p_a = p'_a + \bar{p}_a$  introduce deviations of density and applied pressure from a spatially uniform background. Eq. (62) for the spatial structure of sea level takes the same form mathematically as the temporal structure given by Eq. (47). Both expressions partition sea level fluctuations (in time or space) into a contribution from fluctuations in the mass within a fluid column, and fluctuations of density integrated over the column.

To understand the spatial structure revealed by Eq. (62), consider the case where there are no bottom pressure gradients; i.e., there is a level of no-motion beneath which the horizontal gradients of pressure vanish (see Fig. 37). Eq. (62) then indicates that

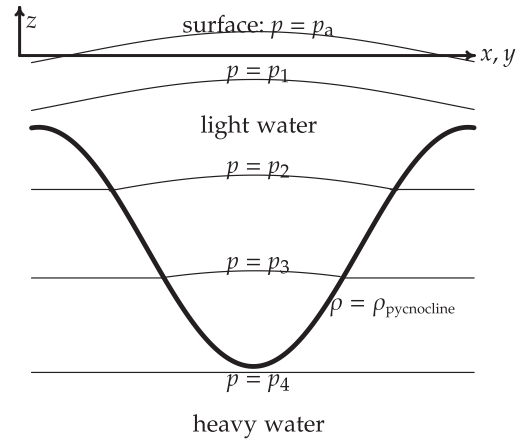


**Fig. 37.** A vertical slice through a 1.5 layer ocean in hydrostatic balance, taken after Fig. 3.3 from Tomczak and Godfrey (1994). Shown here is a plug of light water, as may occur in a warm core eddy, sitting on top of heavy water, where motion is assumed to vanish in the heavy water. The sea surface experiences an applied pressure  $p = p_a$ , assumed to be uniform for this idealized situation. Isolines of hydrostatic pressure are shown, with a slight upward bow to the isobars within the light water region, and flat isobars beneath, in the region of zero motion. Note how sea level is a maximum above the pycnocline minimum, which occurs due to baroclinic compensation. The slope of the pycnocline is about 100–300 times larger than the sea level (Rule 1a of Tomczak and Godfrey, 1994).

the sea level slope is opposite to the slope of the vertically integrated density gradient. For example, consider a warm anomaly in the upper ocean, in which case isopycnals depress downward. Sea level, in turn, will expand upwards to render a local maximum (as in Fig. 37).

The overall magnitude of the sea level gradient associated with density gradients scales according to

$$\nabla \eta \sim - \left( \frac{\delta \rho \, h}{\rho_o \, L} \right), \quad (63)$$

where  $\delta \rho$  is the scale for the horizontal deviations in density. The depth  $h$  is the scale above the level of no motion where density has a nontrivial horizontal gradient; it may also represent the depth of the thermocline. Finally,  $L$  is the horizontal length scale over which horizontal density gradients are measured. For large-scale circulations, we are concerned with horizontal length scales much larger than vertical, so that  $L \gg h$ . Additionally, horizontal deviations of density are far smaller than the constant reference density,  $\rho_o \gg \delta \rho$ . Consequently, the sea level slope is much smaller in magnitude than the pycnocline slope. In particular, Tomczak and Godfrey (1994) (see Rule 1a on their page 33) notes that the sea level slope is roughly 100 to 300 times shallower than the pycnocline slope.

### B.3. Balances between currents and sea level gradients

The connection between sea level and currents is made by noting that the horizontal gradient of hydrostatic pressure (Eq. (45)), which appears in the momentum equation, is given by

$$\nabla_z p = \nabla p_a + g \rho(\eta) \nabla \eta + g \int_z^{\eta} \nabla_z \rho \, dz. \quad (64)$$

This expression exposes how sea level gradients impact the horizontal pressure gradient, which in turn drives ocean currents.

There are many cases where the sea level responds rapidly to atmospheric loading in establishing an inverse barometer structure (e.g., see Appendix C in Griffies and Greatbatch (2012)). In this case, it is useful to absorb the applied pressure  $p_a$  into an effective sea level

$$\nabla\eta + \frac{\nabla p_a}{g\rho(\eta)} \approx \nabla\eta', \quad (65)$$

where

$$\eta' = \eta + p_a/(\rho_o g), \quad (66)$$

in which case the horizontal pressure gradient is given by

$$\nabla_z p \approx \nabla\eta' + g \int_z^\eta \nabla_z \rho dz. \quad (67)$$

This approximate relation forms the basis for the analysis in this section.

### B.3.1. Surface ocean

Perhaps the simplest oceanographically relevant relation between sea level and ocean currents occurs when the surface ocean flow is in geostrophic balance, in which case

$$g\nabla\eta' = -f\hat{\mathbf{z}} \wedge \mathbf{u}, \quad (68)$$

where  $\mathbf{u}$  is the surface horizontal velocity. This equation forms the basis for how surface ocean currents are diagnosed from sea level observations (Wunsch and Stammer, 1998).

If we include in the balance the turbulent momentum flux  $\tau^s$  through the ocean surface boundary, then the sea level gradient takes the form

$$g\nabla\eta' = -f\hat{\mathbf{z}} \wedge \mathbf{u} + \frac{\tau^s}{\rho_o h_E}, \quad (69)$$

where  $h_E$  is the Ekman depth over which the boundary stresses penetrate the upper ocean. As noted by Lowe and Gregory (2006), surface currents in balance with surface wind stresses tend to flow parallel to the sea level gradient, whereas geostrophically balanced surface currents are aligned with surfaces of constant sea level.

### B.3.2. Full ocean column

Vertically integrating the linearized form of the horizontal momentum budget in the absence of horizontal friction leads to the relation

$$(g\rho_o H)\nabla\eta' = \tau^s + Q_m \mathbf{u}_m - \tau^b - (\partial_t + f\hat{\mathbf{z}} \wedge) \mathbf{U}^\rho - \mathbf{B}. \quad (70)$$

In this equation,  $Q_m \mathbf{u}_m$  is the horizontal advective momentum flux associated with surface boundary fluxes of mass, with  $\mathbf{u}_m$  the horizontal momentum per mass of material crossing the ocean surface.<sup>4</sup> Furthermore,  $\tau^b$  is the bottom momentum drag, and

$$\mathbf{B} = g \int_{-H}^\eta dz \int_z^\eta \nabla_z \rho dz \quad (71)$$

is a horizontal pressure gradient arising from horizontal density gradients throughout the ocean column. In addition to the surface and bottom boundary terms, Eq. (70) reveals that the sea level gradient is balanced by time tendencies and Coriolis force associated with the depth integrated mass transport, and a horizontal pressure gradient arising from depth integrated baroclinic structure. Lowe and Gregory (2006) employed the steady state version of this balance while ignoring boundary terms (see their Eq. (7)),

$$(g\rho_o H)\nabla\eta' \approx -f\hat{\mathbf{z}} \wedge \mathbf{U}^\rho - \mathbf{B} \quad (72)$$

to help interpret the mechanisms for sea level changes in their coupled climate simulations.

### B.3.3. Barotropic geostrophic balance

As seen by Eq. (70), sea level gradients balance many terms, including surface fluxes, internal pressure gradients, and vertically integrated transport. Dropping all terms except Coriolis leads to a

geostrophic balance for the vertically integrated flow, whereby Eq. (70) reduces to

$$(g\rho_o H)\nabla\eta' = f\hat{\mathbf{z}} \wedge \mathbf{U}^\rho, \quad (73)$$

which is equivalent to

$$\mathbf{U}^\rho = -\left(\frac{g\rho_o H}{f}\right)\hat{\mathbf{z}} \wedge \nabla\eta'. \quad (74)$$

That is, in this idealized flow situation, the sea level is, with a constant depth and Coriolis parameter, the streamfunction for the vertically integrated flow.

Following Wunsch and Stammer (1998), we consider the relation (73) for the purpose of capturing a scaling to see how much vertically integrated transport is associated with a deviation in the sea level. In particular, the meridional transport between two longitudes  $x_1$  and  $x_2$  is given by

$$\int_{x_1}^{x_2} dx V^\rho = \frac{g\rho_o H}{f} [\eta(x_2) - \eta(x_1)], \quad (75)$$

where we assumed the ocean bottom is flat. Note that the horizontal distance drops out from the right hand side, so that the meridional geostrophic transport only depends on the difference in sea level across the zonal section, and not on the length of the section. Following the example of Wunsch and Stammer (1998), assume the ocean depth is  $H = 4000$  m and set  $f = 7.3 \times 10^{-5} \text{ s}^{-1}$ , as occurs at  $30^\circ$  latitude, which renders a transport of about  $6 \times 10^9 \text{ kg s}^{-1}$ , or six Sverdrups,<sup>5</sup> for a sea level deviation of  $\Delta\eta = 0.01$  m. This calculation, though subject to many assumptions, provides a useful order of magnitude scaling to gauge the significance of a sea level deviation.

### B.4. Evolution of ocean column thickness and dynamic topography

It is often assumed in physical oceanography that there is a pressure at which baroclinic currents vanish (Pond and Pickard, 1983; Tomczak and Godfrey, 1994). This level of no motion occurs if the barotropic pressure head associated with an undulation in the sea level is exactly compensated by density structure within the ocean interior. Currents are static below the level of no motion, and so this deeper region of the ocean is dynamically disconnected from changes in sea level. Fig. 37 illustrates this situation in the commonly considered 1.5 layer ocean. The evolution of ocean column thickness between the surface and the level of no motion then provides a useful proxy for the evolution of sea level.

The above discussion motivates the following mathematical formulation, in which we consider the thickness of fluid extending from the ocean free surface to a chosen pressure level in the ocean interior, as given by

$$\mathcal{D}(\mathcal{P}) = \eta - z(\mathcal{P}). \quad (76)$$

We may relate this expression to the vertical integral between two pressure surfaces of the specific volume  $\rho^{-1}$

$$\mathcal{D}(\mathcal{P}) = \int_{z(\mathcal{P})}^\eta dz = g^{-1} \int_{p_a}^{\mathcal{P}} \frac{dp}{\rho}, \quad (77)$$

where the second step used the hydrostatic balance  $\partial_z p = -g\rho$ . We refer to the thickness  $\mathcal{D}(\mathcal{P})$  as the *dynamic topography* with respect to a reference pressure  $\mathcal{P}$ . Note that it is sometimes also called the *steric sea level* with respect to pressure  $\mathcal{P}$ . Evolution of the dynamic topography  $\mathcal{D}$  arises from changes in the applied pressure, and changes in the specific volume

<sup>5</sup> A volume transport of  $1 \text{ m}^3 \text{ s}^{-1}$  corresponds to roughly  $10^3 \text{ kg s}^{-1}$  mass transport of seawater, so that a volume Sverdrup of  $10^6 \text{ m}^3 \text{ s}^{-1}$  corresponds to a mass Sverdrup of  $10^9 \text{ kg s}^{-1}$ .

<sup>4</sup> In ocean models,  $\mathbf{u}_m$  is generally taken as the surface ocean horizontal velocity.

$$g \frac{\partial \mathcal{D}(\mathcal{P})}{\partial t} = -\frac{1}{\rho(\eta)} \frac{\partial p_a}{\partial t} + \int_{p_a}^{\mathcal{P}} \frac{\partial \rho^{-1}}{\partial t} dp, \quad (78)$$

where the time derivative acting on the specific volume is taken on surfaces of constant pressure. If the depth  $z(\mathcal{P})$  of the constant pressure surface is static, then the evolution of layer thickness  $\mathcal{D}(\mathcal{P})$  is identical to the sea level  $\eta$ . In general, there is no such static pressure level, thus making the time tendencies differ, though certain situations may warrant this approximation.

Analyses based on assuming a level of no motion were common in simulations with a rigid lid ocean model, as in the studies of Delworth et al. (1993), Bryan (1996) and Griffies and Bryan (1997). Rigid lid models were the dominant algorithmic choice for ocean climate models through the early 2000s. As there is no tendency equation for the free surface in rigid lid models, only indirect methods are available for obtaining information about the time variations of the sea level. Gregory et al. (2001) provide an appendix in which they summarize commonly used methods for analyzing sea level fluctuations within rigid lid ocean models. Amongst the various methods, Gregory et al. (2001) note that the use of a level of no motion is inaccurate in those regions where currents readily reach to the bottom. The Southern Ocean is one such region, where the flow has a large barotropic component. Also, as noted by Danabasoglu and McWilliams (2002), on intra-annual time scales, the tropical circulations on the depth/latitude plane penetrate to the ocean bottom.

Free surface ocean models compute dynamic sea level directly, in which case there is no need to assume a level of no motion. Nor is it necessary to employ the approximate methods detailed by Gregory et al. (2001) required to analyze simulated sea level variations in rigid lid models. For this reason, and others such as the straightforward use of water fluxes rather than virtual tracer fluxes (Griffies et al., 2001), rigid lid models are rarely used today for realistic climate modelling, with preference given to models computing sea level or bottom pressure prognostically. Nonetheless, given the records of observed hydrography, it remains useful to consider dynamic topography as a proxy for dynamic sea level (e.g., Levitus, 1990).

### Appendix C. Heat conservation properties of the CORE-II models

Given the importance of heat and salt conservation in ocean models used to study sea level, we present in this Appendix a brief analysis of the heat conservation properties of the models considered in this paper. We show that all but one of the models conserve heat.

#### C.1. Quantitative statements about heat fluxes and global mean sea level

A global ocean mean boundary heat flux of  $\overline{Q^{\text{heat}}} = 1 \text{ W m}^{-2}$  increases the global ocean temperature by roughly<sup>6</sup>

$$\frac{\overline{Q^{\text{heat}}}}{\rho_o C_p^o H} \approx 0.2 \text{ }^\circ\text{C century}^{-1}, \quad (79)$$

<sup>6</sup> The convention used in this paper for reporting heat fluxes (enthalpy per time per horizontal area) is to normalize by the ocean surface area. To compute the net enthalpy per time (in units of Watt) crossing the ocean surface requires multiplying by the ocean surface area. The alternative convention, often used in climate studies not specifically focused on the ocean, considers the enthalpy per time normalized by the total surface area of the earth. The two fluxes, measured as a Watt per square metre, differ by the area ratio which is roughly 0.7. Hence, a heat flux of  $1 \text{ W m}^{-2}$  computed with respect to the ocean surface area corresponds to  $0.7 \text{ W m}^{-2}$  with respect to the total earth surface area.

$H \approx 4000 \text{ m}$  is the mean ocean depth. It is at this level, or slightly smaller, that estimates from observations suggest the ocean has warmed during the second half of the 20th century, with an increase in warming seen in the early years of the 21st century (Church et al., 2011). This same heat flux gives rise to a global mean sea level rise of magnitude (see Eq. (44) in Appendix A.5)

$$\frac{\overline{Q^{\text{heat}}}}{\rho_o C_p} \alpha_{\text{bulk}} \approx 1 \text{ mm yr}^{-1} = 0.1 \text{ m century}^{-1}, \quad (80)$$

where we assumed the thermal expansion coefficient to be  $\alpha_{\text{bulk}} \approx 1.7 \times 10^{-4} \text{ K}^{-1}$  (i.e., the average over the upper 1000 m as shown in Fig. 1).

It is notable that there is a huge disparity between the magnitude of local values of ocean surface heat fluxes, which can be  $\pm 100\text{--}1000 \text{ W m}^{-2}$ , and the relatively small residual global mean ocean heat flux, which is on the order of  $1 \text{ W m}^{-2}$ . Local values of boundary heating drive regional changes in thermosteric sea level, whereas the global mean heat flux drives the global mean thermosteric sea level (Appendix A.5). As described by Large and Yeager (2012) and Stephens et al. (2012), local uncertainties in the observed heat fluxes, which can be more than  $\pm 10 \text{ W m}^{-2}$ , make it difficult to detect trends in anthropogenic ocean warming through direct measures of boundary fluxes. Measures of global mean sea level provide an indirect means to determine the net ocean heating, with the ocean integrating the heat fluxes and so highlighting low frequency trends. This is the key reason that studies of global mean sea level are closely related to studies of ocean heat content.

On interannual and longer time scales, the relatively large ocean heat capacity makes the ocean the dominant media (more than 90%) for heat storage in the climate system.<sup>7</sup> Hence, one requirement for using ocean models to study global mean sea level is that the models properly represent the transfer of heat across the ocean boundaries, and impart that heat to the ocean fluid. That is, the models should conserve heat, so that the global mean ocean temperature changes only through the passage of fluxes across the ocean boundaries. Heat resulting from spurious sources or sinks is generally sequestered in the ocean and in turn impacts on global mean sea level. This is the key reason that heat conservation is essential for ocean models used to study global mean sea level. Salt conservation must also be respected for the same reasons.

#### C.2. A method to diagnose heat conservation

Many models have online diagnostics to determine the degree to which the model conserves scalar fields, such as heat and salt. When available, we use these diagnostics to assess conservation. We also make use of another approach that integrates the budget for global mean ocean temperature, following the formulation in Appendix A.4. Given the heat and mass fluxes crossing the liquid ocean boundaries, we time step Eq. (40) to provide an *offline* calculation of global mean ocean temperature. This *offline* global mean temperature is then compared to the *online* global mean temperature diagnosed directly from the associated model simulation. The two global mean ocean temperatures will not agree exactly, since we do not have access to the model restart files. So we must time step the *offline* Eq. (40) using annual mean boundary heat and mass fluxes, whereas the *online* mean temperature is accumulated using each model time step.

<sup>7</sup> As discussed on page 22 of Gill (1982), the atmosphere mass per horizontal area at the ocean surface is  $\approx 10^4 \text{ kg m}^{-2}$ . This is the mass per area of 10 m of liquid ocean. Furthermore, the specific heat capacity for the ocean,  $C_p^o \approx 3990 \text{ J }^\circ\text{C}^{-1} \text{ kg}^{-1}$ , is about four times that of the atmosphere. Hence, 2.5 m of liquid ocean has the same heat capacity per horizontal area as the entire atmosphere.

To examine the conservation properties of the simulations, we compute the ratio of the global mean annual ocean temperature computed online to that computed offline. Unity signals perfect agreement, yet again, perfect agreement is not possible due to temporal sampling differences. Correspondingly, we expect a slight drift between the two calculations, since the offline calculation accumulates the errors from temporal subsampling. We make the following observations based on this calculation.

- ALL BUT ONE OF THE CORE-II SIMULATIONS CONSIDERED HERE CONSERVE OCEAN HEAT. As stated above, many of the conserving models possess online diagnostics that more rigorously verify their conservation properties, thus supporting the conclusion that they are conservative.
- THE FSU-HYCOM CORE-II SIMULATION DOES NOT CONSERVE HEAT. The online global mean ocean temperature from FSU-HYCOM is systematically warmer than the offline temperature computed from boundary heat fluxes. Both time series are reasonably linear (not shown), suggesting that the non-conservation is roughly constant in time. To test this hypothesis, we added  $1 \text{ W m}^{-2}$  to the surface heat flux for all time steps in the offline calculation. Doing so brings the temperature ratio in line to those from the conservative models (not shown). Megann et al. (2010) noted that when coupled to an atmosphere and land model, the HYCOM ocean temperature drifted in a way that suggested a spurious heat source on the order of  $0.5 \text{ W m}^{-2}$ . A non-conservative source of heat on the order of  $0.5\text{--}1 \text{ W m}^{-2}$  thus appears to be associated with the HYCOM dynamical core used in the present study as well as Megann et al. (2010). The spurious heat source in FSU-HYCOM dominates the simulated global mean sea level throughout the CORE-II simulation. In particular, the net boundary heat flux into the FSU-HYCOM ocean during years 1993–2007 of the 5th CORE-II cycle is  $-0.75 \text{ W m}^{-2}$  (Figs. 10 and 11). For a conservative model, this negative heat flux would lead to a downward trend in global mean ocean temperature. However, global mean ocean temperature, as diagnosed within the prognostic model, is in fact rising during this same period (see Fig. 4).

### C.3. Some lessons learned

Heat conservation, and in fact conservation of any scalar, should not be presumed of an ocean model until proven through analysis such as that considered here. Given the fundamental nature of scalar conservation, this basic analysis can be a powerful means of revealing limitations and/or bugs in a numerical ocean code. In fact, two earlier contributing models in this study were removed due to their egregious lack of heat conservation. Exposing problems with model conservation properties has resulted in the respective model developers re-examining their code with an aim to ensure that the numerical methods are fully conservative. The HYCOM code is a case in point, in which a version more recent than that used here has been written that conserves heat and salt (Rainer Bleck and Shan Sun, personal communication 2013). A suitable CORE-II simulation using this updated code was not available in time for inclusion in the present study.

## References

Alves, O., Shi, L., Wedd, R., Balmaseda, M., Chang, Y., Chepurin, G., Fujii, Y., Gaillard, F., Good, S., Guinehut, S., Haines, K., Hernandez, F., Lee, T., Palmer, M., Peterson, K., Smasuda, S., Storto, A., Toyoda, T., Valdivieso, M., Vernieres, G., Wang, X., Yin, Y., 2014. An assessment of upper ocean salinity reanalyses from CLIVAR GSOP/GODAE systems. *CLIVAR Exchanges* (19,1 – February 2014), pp. 11–14.

Antonov, J., Seidov, D., Boyer, T.P., Locarnini, R.A., Mishonov, A.V., Garcia, H.E., Baranova, O.K., Zweng, M.M., Johnson, D.R., 2010. Salinity. *World Ocean Atlas 2009*, vol. 2. NOAA Atlas NESDIS 69, NOAA/NESDIS, U.S. Dept. of Commerce, Washington, D.C.

Bates, S., Fox-Kemper, B., Jayne, S.R., Large, W.G., Stevenson, S., Yeager, S.G., 2012. Mean biases, variability, and trends in air-sea fluxes and sea surface temperature in the CCSM4. *J. Clim.* 25, 7781–7801.

Becker, M., Meyssignac, B., Letetrel, C., Llovel, W., Cazenave, A., Delcroix, T., 2012. Sea level variations at tropical Pacific islands since 1950. *Global Planet. Change* 80–81, 85–98.

Bouttes, N., Gregory, J.M., Lowe, J.A., 2013. The reversibility of sea level rise. *J. Clim.* 26, 259–280.

Boyer, T.P., Levitus, S., Antonov, J.I., Locarnini, R.A., Garcia, H.E., 2005. Linear trends in salinity for the World Ocean, 1955–1998. *Geophys. Res. Lett.* 32, L01604. <http://dx.doi.org/10.1029/2004GL021791>.

Brodeau, L., Barnier, B., Treguier, A., Penduff, T., Gulev, S., 2010. An ERA40-based atmospheric forcing for global ocean circulation models. *Ocean Modell.* 31, 88–104.

Bromirski, P., Miller, A., Flick, R., Auad, G., 2011. Dynamical suppression of sea level rise along the Pacific coast of North America: Indications for imminent acceleration. *J. Geophys. Res.*, 116–C07005. <http://dx.doi.org/10.1029/2010JC006759>.

Bryan, F.O., 1997. The axial angular momentum balance of a global ocean general circulation model. *Dyn. Atmos. Oceans* 25, 191–216.

Bryan, K., 1996. The steric component of sea level rise associated with enhanced greenhouse warming: a model study. *Climate Dyn.* 12, 545–555.

Capotondi, A., Alexander, M., Bond, N., Curchitser, E., Scott, J., 2012. Enhanced upper ocean stratification with climate change in the CMIP3 models. *J. Geophys. Res.*, 117–C04031. <http://dx.doi.org/10.1029/2011JC007409>.

Chambers, D., Merrifield, M., Nerem, R., 2012. Is there a 60-year oscillation in global mean sea level? *Geophys. Res. Lett.* 39 (L18607). <http://dx.doi.org/10.1029/2012gl052885>.

Chang, Y.-S., Rosati, A., Vecchi, G., 2010. Basin patterns of global sea level changes for 2004–2007. *J. Marine Syst.* 80, 115–124.

Church, J., Roemmich, D., Domingues, C.M., Willis, J.K., White, N.J., Gilson, J.E., Stammer, D., Köhl, A., Chambers, D.P., Landerer, F.W., Marotzke, J., Gregory, J.M., Suzuki, T., Cazenave, A., Traou, P.-Y.L., 2010. Ocean temperature and salinity contributions to global and regional sea-level change. In: Church, J.A., Woodworth, P.L., Aarup, T., Wilson, W.S. (Eds.), *Understanding Sea-Level Rise and Variability*. Blackwell Publishing, pp. 143–176.

Church, J., White, N., Domingues, C., Monselesan, D., 2013a. Sea-level change and ocean heat-content change. In: Siedler, G., Griffies, S.M., Gould, J., Church, J. (Eds.), *Ocean Circulation and Climate. A 21st Century Perspective*, second ed., International Geophysics Series second ed., vol. 103 Academic Press.

Church, J., White, N., Konikow, L., Domingues, C., Cogley, J., Rignot, E., Gregory, J., van den Broeke, M., Monaghan, A., Velicogna, I., 2011. Revisiting the earth's sea-level and energy budgets from 1961 to 2008. *Geophys. Res. Lett.* 38, L18601. <http://dx.doi.org/10.1029/2011GL048794>.

Church, J.A., Clark, P.U., Cazenave, A., Gregory, J.M., Jevrejeva, S., Levermann, A., Merrifield, M.A., Milne, G.A., Nerem, R.S., Nunn, P.D., Payne, A.J., Pfeffer, W.T., Stammer, D., Unnikrishnan, A.S., 2013b. Sea level change. *Climate Change 2013: The Physical Science Basis. Contribution of Working Group I to the Fifth Assessment Report of the Intergovernmental Panel on Climate Change*. Cambridge University Press, Cambridge, United Kingdom, pp. 1137–1216.

Conkright, M., Antonov, J., Baranova, O., Boyer, T., Garcia, H., Gelfeld, F., Johnson, D., Locarnini, R., Murphy, P., O'Brien, T., Smolyar, I., Stephens, C., 2002. *Introduction. World Ocean Database 2001*, vol. 1. NOAA Atlas NESDIS 42, U.S. Government Printing Office 13, NOAA, Washington, D.C., 167 pp.

Dai, A., Qian, T., Trenberth, K., Milliman, J., 2009. Changes in continental freshwater discharge from 1948–2004. *J. Clim.* 22, 2773–2791.

Danabasoglu, G., 2004. A comparison of global ocean general circulation model solutions obtained with synchronous and accelerated integration methods. *Ocean Modell.* 7, 323–341.

Danabasoglu, G., McWilliams, J., 2002. Eulerian and eddy-induced meridional overturning circulations in the tropics. *J. Phys. Oceanogr.* 32, 2054–2071.

Danabasoglu, G., Yeager, S.G., Bailey, D., Behrens, E., Bentsen, M., Bi, D., Biastoch, A., Böning, C.W., Bozec, A., Canuto, V.M., Cassou, C., Chassignet, E., Coward, A.C., Danilov, S., Diansky, N., Drange, H., Farneti, R., Fernandez, E., Fogli, P.G., Forget, G., Fujii, Y., Griffies, S.M., Gusev, A., Heimbach, P., Howard, A., Jung, T., Kelley, M., Large, W.G., Leboissetier, A., Lu, J., Madec, G., Marsland, S.J., Masina, S., Navarra, A., Nurser, A.G., Pirani, A., y Méliá, D.S., Samuels, B.L., Scheinert, M., Sidorenko, D., Treguier, A.-M., Tsujino, H., Uotila, P., Valcke, S., Voldoire, A., Wang, Q., 2014. North Atlantic simulations in Coordinated Ocean-ice Reference Experiments phase II (CORE-II). Part I: Mean states. *Ocean Modell.* 73 (0), 76–107 <<http://dx.doi.org/10.1016/j.ocemod.2013.10.005>>.

Delworth, T.L., Broccoli, A.J., Rosati, A., Stouffer, R.J., Balaji, V., Beesley, J.A., Cooke, W.F., Dixon, K.W., Dunne, J., Dunne, K.A., Durachta, J.W., Findell, K.L., Ginoux, P., Gnanadesikan, A., Gordon, C., Griffies, S.M., Gudgel, R., Harrison, M.J., Held, I.M., Hemler, R.S., Horowitz, L.W., Klein, S.A., Knutson, T.R., Kushner, P.J., Langenhorst, A.L., Lee, H.-C., Lin, S., Lu, L., Malyshev, S.L., Milly, P., Ramaswamy, V., Russell, J., Schwarzkopf, M.D., Shevliakova, E., Sirutis, J., Spelman, M., Stern, W.F., Winton, M., Wittenberg, A.T., Wyman, B., Zeng, F., Zhang, R., 2006. GFDL's CM2 global coupled climate models – Part I: Formulation and simulation characteristics. *J. Clim.* 19, 643–674.

Delworth, T.L., Manabe, S., Stouffer, R.J., 1993. Interdecadal variations of the thermohaline circulation in a coupled ocean–atmosphere model. *J. Clim.* 6, 1993–2011.

Domingues, C., Church, J., White, N., Gleckler, P., Wijffels, S., Barker, P., Dunn, J., 2008. Improved estimates of upper-ocean warming and multi-decadal sea-level rise. *Nature* 453, 1090–1093.

- Doney, S.C., Yeager, S., Danabasoglu, G., Large, W., McWilliams, J., 2007. Mechanisms governing interannual variability of upper-ocean temperature in a global ocean hindcast simulation. *J. Phys. Oceanogr.* 37, 1918–1938.
- Ducet, N., Le Traon, P.-Y., Reverdin, G., 2000. Global high-resolution mapping of ocean circulation from TOPEX/Poseidon and ERS-1 and -2. *J. Geophys. Res.* 105, 19477–19498.
- Dukowicz, J.K., Smith, R.D., 1994. Implicit free-surface method for the Bryan-Cox-Semtner ocean model. *J. Geophys. Res.* 99, 7991–8014.
- Durack, P., Wijffels, W., 2010. Fifty-year trends in global ocean salinities and their relationship to broad-scale warming. *J. Clim.* 23, 4342–4362.
- Durack, P., Wijffels, W., Matear, R., 2012. Ocean salinities reveal strong global water cycle intensification during 1950 to 2000. *Science* 336, 455–458.
- Esselborn, S., Eden, C., 2001. Sea surface height changes in the North Atlantic Ocean related to the North Atlantic Oscillation. *Geophys. Res. Lett.* 28, 3473–3476.
- Ezer, T., Atkinson, L.P., Corlett, W., Blanco, J., 2013. Gulf Stream's induced sea level rise and variability along the U.S. mid-Atlantic coast. *J. Geophys. Res.* 118. <http://dx.doi.org/10.1002/jgrc.20091>.
- Feng, M., McPhaden, M., Lee, T., 2010. Decadal variability of the Pacific subtropical cells and their influence on the southeast Indian Ocean. *Geophys. Res. Lett.* 37, L09606. <http://dx.doi.org/10.1029/2010GL042796>.
- Fox-Kemper, B., Lumpkin, R., Bryan, F., 2013. Lateral transport in the ocean interior. In: Siedler, G., Griffies, S.M., Gould, J., Church, J. (Eds.), *Ocean Circulation and Climate. A 21st Century Perspective*, second ed., International Geophysics Series second ed., vol. 103 Academic Press, pp. 185–209.
- Fu, L.-L., 2001. Ocean circulation and variability from satellite altimetry. In: Seidler, G., Church, J., Gould, J. (Eds.), *Ocean Circulation and Climate, International Geophysics Series*, vol. 77. Academic Press, San Diego, pp. 141–172.
- Gates, W., 1993. AMIP: The Atmosphere Model Intercomparison Project. *Bull. Am. Meteorol. Soc.* 73, 1962–1970.
- Gerdes, R., Hurlin, W.J., Griffies, S.M., 2006. Sensitivity of a global ocean model to increased run-off from Greenland. *Ocean Modell.* 12, 416–435.
- Gill, A., 1982. *Atmosphere-ocean dynamics*. International Geophysics Series, vol. 30. Academic Press, London, 662+xxv pp.
- Gill, A.E., Niiler, P., 1973. The theory of the seasonal variability in the ocean. *Deep-Sea Res.* 20 (9), 141–177.
- Gleckler, P., Santer, B., Domingues, C., Pierce, D., Barnett, T., Church, J., Taylor, K., AchutaRao, K., Boyer, T., Ishii, M., Caldwell, P., 2012. Human-induced global ocean warming on multidecadal timescales. *Nat. Clim. Change* 2, 524–529.
- Gower, J., 2010. Comment on Response of the global ocean to Greenland and Antarctic ice melting. *J. Geophys. Res.* 115. <http://dx.doi.org/10.1029/2010JC006097>.
- Greatbatch, R.J., 1994. A note on the representation of steric sea level in models that conserve volume rather than mass. *J. Geophys. Res.* 99, 12767–12771.
- Gregory, J., Church, J., Boer, G., Dixon, K., Flato, G., Jackett, D., Lowe, J., O'Farrell, S., Roeckner, E., Russell, G., Stouffer, R., Winton, M., 2001. Comparison of results from several AOGCMs for global and regional sea-level change 1900–2100. *Clim. Dyn.* 18, 225–240.
- Gregory, J., White, N., Church, J., Bierkens, M., Box, J., van den Broeke, R., Cogley, J., Fettweis, X., Hanna, E., Huybrechts, P., Konikow, L., Leclercq, P., Marzeion, B., Orelemans, J., Tamsisla, M., Wada, Y., Wake, L., van den Wal, R., 2013. Twentieth-century global-mean sea-level rise: is the whole greater than the sum of the parts? *J. Clim.* 26, 4476–4499.
- Griffies, S.M., Adcroft, A.J., Aiki, H., Balaji, V., Bentson, M., Bryan, F., Danabasoglu, G., Denvil, S., Drange, H., England, M., Gregory, J., Hallberg, R., Legg, S., Martin, T., McDougall, T.J., Pirani, A., Schmidt, G., Stevens, D., Taylor, K., Tsujino, H., 2009a. Sampling physical ocean fields in WCRP CMIP5 simulations, ICPO Publication Series 137, WCRP Informal Report No. 3/2009. <http://www-pcmdi.llnl.gov>.
- Griffies, S.M., Biastoch, A., Böning, C.W., Bryan, F., Danabasoglu, G., Chassignet, E., England, M.H., Gerdes, R., Haak, H., Hallberg, R.W., Hazeleger, W., Jungclauss, J., Large, W.G., Madec, G., Pirani, A., Samuels, B.L., Scheinert, M., Gupta, A.S., Severijns, C.A., Simmons, H.L., Treguier, A.M., Winton, M., Yeager, S., Yin, J., 2009b. Coordinated Ocean-ice Reference Experiments (COREs). *Ocean Modell.* 26, 1–46.
- Griffies, S.M., Bryan, K., 1997. A predictability study of simulated North Atlantic multidecadal variability. *Clim. Dyn.* 13, 459–487.
- Griffies, S.M., Greatbatch, R.J., 2012. Physical processes that impact the evolution of global mean sea level in ocean climate models. *Ocean Modell.* 51, 37–72.
- Griffies, S.M., Pacanowski, R., Schmidt, M., Balaji, V., 2001. Tracer conservation with an explicit free surface method for z-coordinate ocean models. *Mon. Weather Rev.* 129, 1081–1098.
- Griffies, S.M., Pacanowski, R.C., Hallberg, R.W., 2000. Spurious diapycnal mixing associated with advection in a z-coordinate ocean model. *Mon. Weather Rev.* 128, 538–564.
- Häkkinen, S., 2000. Decadal air-sea interaction in the North Atlantic based on observations and modeling results. *J. Clim.* 13, 1195–1219.
- Häkkinen, S., Rhines, P., 2004. Decline of subpolar North Atlantic circulation during the 1990s. *Science* 304, 555–559.
- Hallberg, R., Adcroft, A., Dunne, J., Krasting, J., Stouffer, R., 2013. Sensitivity of twenty-first-century global-mean steric sea level rise to ocean model formulation. *J. Clim.* 26, 2947–2956.
- Hanna, E., Navarro, F., Pattyn, F., Domingues, C., Fettweis, X., Ivins, E., Nicholls, R., Ritz, C., Smith, B., Tulaczy, S., Whitehouse, P., Zwally, H., 2013. Ice-sheet mass balance and climate change. *Nature* 498, 51–59.
- Hernandez, F., Ferry, N., Balmaseda, M., Chang, Y.-S., Chepurin, G., Fujii, Y., Guinehut, S., Kohl, A., Martin, M., Meyssignac, B., Parent, L., Peterson, K., Storto, A., Toyoda, T., Valdivieso, M., Vernieres, G., Wang, O., Wang, X., Xue, Y., Yin, Y., 2014. Sea level intercomparison: initial results. CLIVAR Exchanges (19,1 – February 2014), pp. 18–21.
- Hosoda, S., Sugo, T., Shikama, N., Mizuno, K., 2009. Global surface layer salinity change detected by Argo and its implication for hydrological cycle intensification. *J. Oceanogr.* 65, 579–586.
- Hsieh, W., Bryan, K., 1996. Redistribution of sea level rise associated with enhanced greenhouse warming: a simple model study. *Clim. Dyn.* 12, 535–544.
- Huang, R.X., 1993. Real freshwater flux as a natural boundary condition for the salinity balance and thermohaline circulation forced by evaporation and precipitation. *J. Phys. Oceanogr.* 23, 2428–2446.
- Huang, R.X., Jin, X., 2002. Sea surface elevation and bottom pressure anomalies due to thermohaline forcing: Part I: Isolated perturbations. *J. Phys. Oceanogr.* 32, 2131–2150.
- Hurrell, J., Hack, J., Shea, D., Caron, J., Rosinski, J., 2008. A new sea surface temperature and sea ice boundary data set for the Community Atmosphere Model. *J. Clim.* 21, 5145–5153.
- IOC, SCOR, IAPSO, 2010. The international thermodynamic equation of seawater-2010: calculation and use of thermodynamic properties. Intergovernmental Oceanographic Commission, Manuals and Guides No.56, UNESCO. <http://www.TEOS-10.org>. 196 pp
- Ishii, M., Kimoto, M., 2009. Reevaluation of historical ocean heat content variations with time-varying XBT and MBT depth bias corrections. *J. Oceanogr.* 65, 287–299.
- Kalnay, E.M., Kanamitsu, M., Kistler, R., Collins, W., Deaven, D., Gandin, L., Iredell, M., Saha, S., White, G., Woollen, J., Zhu, Y., Leetmaa, A., Reynolds, R., Chelliah, M., Ebisuzaki, W., Higgins, W., Janowiak, J., Mo, K.C., Ropelewski, C., Wang, J., Jenne, R., Joseph, D., 1996. The NMC/NCAR 40-year reanalysis project. *Bull. Am. Meteorol. Soc.* 77, 437–471.
- Kennedy, J., Rayner, N., Smith, R., Parker, D., Saunby, M., 2011. Reassessing biases and other uncertainties in sea surface temperature observations measured in situ since 1850: 1. Measurement and sampling uncertainties. *Geophys. Res. Lett.* 116, D14103. <http://dx.doi.org/10.1029/2010JD015218>.
- Killworth, P.D., Stainforth, D., Webb, D.J., Paterson, S.M., 1991. The development of a free-surface Bryan-Cox-Semtner ocean model. *J. Phys. Oceanogr.* 21, 1333–1348.
- Köhl, A., Stammer, D., 2008. Decadal sea level changes in the 50-year GECCO ocean synthesis. *J. Clim.* 21, 1876–1890.
- Kopp, R.E., 2013. Does the mid-Atlantic United States sea-level acceleration hot spot reflect ocean dynamic variability? *Geophys. Res. Lett.* <http://dx.doi.org/10.1002/grl.50781>.
- Kopp, R.E., Mitrovica, J.X., Griffies, S.M., Yin, J., Hay, C.C., Stouffer, R.J., 2010. The impact of Greenland melt on regional sea level: a preliminary comparison of dynamic and static equilibrium effects. *Clim. Change Lett.* 103, 619–625.
- Kuhlbrodt, T., Gregory, J.M., 2012. Ocean heat uptake and its consequences for the magnitude of sea level and climate change. *Geophys. Res. Lett.* 38, L18608. <http://dx.doi.org/10.1029/2012GL052952>.
- Lambeck, K., Esat, T., Potter, E., 2002. Links between climate and sea levels for the past three million years. *Nature* 419, 199–206.
- Landerer, F., Jungclauss, J., Marotzke, J., 2007a. Ocean bottom pressure changes lead to a decreasing length-of-day in a warming climate. *Geophys. Res. Lett.* 34, L06307. <http://dx.doi.org/10.1029/2006GL029106>.
- Landerer, F., Jungclauss, J., Marotzke, J., 2007b. Regional dynamic and steric sea level change in response to the IPCC-A1B Scenario. *J. Phys. Oceanogr.* 37, 296–312.
- Large, W.G., Yeager, S., 2009. The global climatology of an interannually varying air-sea flux data set. *Clim. Dyn.* 33, 341–364.
- Large, W.G., Yeager, S., 2012. On the observed trends and changes in global sea surface temperature and air-sea heat fluxes (1984–2006). *J. Clim.* 25, 6123–6135.
- Laxon, S., Giles, K.A., Ridout, A.L., Ingham, D.J., Willatt, R., Cullen, R., Kwok, R., Schweiger, A., Zhang, J., Haas, C., Hendricks, S., Krisheld, R., Kurtz, N., Farrell, S., Davidson, M., 2013. CryoSat-2 estimates of Arctic sea ice thickness and volume. *Geophys. Res. Lett.* 40. <http://dx.doi.org/10.1002/grl.50193>.
- Le Traon, P.-Y., Nadal, F., Ducet, N., 1998. An improved mapping method of multi-satellite altimeter data. *J. Atmos. Oceanic Technol.* 15, 522–534.
- Leuliette, E., Willis, J., 2011. Balancing the sea level budget. *Oceanography* 24, 122–129.
- Levitus, S., 1990. Multipentadal variability of steric sea level and geopotential thickness of the north atlantic ocean, 1970/1974 versus 1955/1959. *J. Geophys. Res.* 95, 5233–5238.
- Levitus, S., Antonov, J., Boyer, T., 2005. Warming of the world ocean, 1955/2003. *Geophys. Res. Lett.* 32 (2). <http://dx.doi.org/10.1029/2004GL021592>.
- Levitus, S., Antonov, J., Boyer, T., Baranova, O., Garcia, H., Locarnini, R., Mishonov, A., Reagan, J., Seidov, D., Yarosh, E., Zweng, M.M., 2012. World ocean heat content and thermohaline sea level change (0–2000 m), 1955–2010. *Geophys. Res. Lett.* 39, L10603. <http://dx.doi.org/10.1029/2012GL051106>.
- Locarnini, R., Mishonov, A.V., Antonov, J.I., Boyer, T.P., Garcia, H.E., Baranova, O.K., Zweng, M.M., Johnson, D.R., 2010. Temperature. World Ocean Atlas 2009, vol. 1. NOAA Atlas NESDIS 68, NOAA/NESDIS, U.S. Dept. of Commerce, Washington, D.C.
- Lohmann, K., Drange, H., Bentzen, M., 2009. A possible mechanism for the strong weakening of the north atlantic subpolar gyre in the mid-1990s. *Geophys. Res. Lett.* 36 (15). <http://dx.doi.org/10.1029/2009GL039166>.
- Lombard, A., Garric, G., Penduff, T., 2009. Regional patterns of observed sea level change: insights from a 1/4° global ocean/sea-ice hindcast. *Ocean Dyn.* 59, 433–449.

- Lorbacher, K., Dengg, J., Böning, C., Biastoch, A., 2010. Regional patterns of sea level change related to interannual variability and multidecadal trends in the Atlantic meridional overturning circulation. *J. Phys. Oceanogr.* 23, 4243–4254.
- Lorbacher, K., Marsland, S.J., Church, J.A., Griffies, S.M., Stammer, D., 2012. Rapid barotropic sea-level rise from ice-sheet melting scenarios. *J. Geophys. Res.* 117, C06003.
- Losch, M., Adcroft, A., Campin, J.-M., 2004. How sensitive are coarse general circulation models to fundamental approximations in the equations of motion? *J. Phys. Oceanogr.* 34, 306–319.
- Lowe, J.A., Gregory, J.M., 2006. Understanding projections of sea level rise in a Hadley Centre coupled climate model. *J. Geophys. Res.* 111 (C11) <<http://dx.doi.org/10.1029/2005JC003421>>, n/a–n/a.
- MacKinnon, J., St. Laurent, Louis, Garabato, A.N., 2013. Diapycnal mixing processes in the ocean interior. In: Siedler, G., Griffies, S.M., Gould, J., Church, J. (Eds.), *Ocean Circulation and Climate: A 21st Century Perspective*, second ed., International Geophysics Series second ed., vol. 103 Academic Press.
- McCarthy, G., Frajka-Williams, E., Johns, W., Baringer, M., Meinen, C., Bryden, H., Rayner, D., Duchez, A., Roberts, C., Cunningham, S.A., 2012. Observed interannual variability of the Atlantic meridional overturning circulation at 26.5°N. *Geophys. Res. Lett.* <http://dx.doi.org/10.1029/2012GL052933>.
- McDougall, T.J., 2003. Potential enthalpy: a conservative oceanic variable for evaluating heat content and heat fluxes. *J. Phys. Oceanogr.* 33, 945–963.
- McGregor, S., Sen Gupta, A., England, M., 2012. Constraining wind stress products with sea surface height observations and implications for Pacific ocean sea level trend attribution. *J. Clim.* 25, 8164–8176.
- Meehl, G., Covey, C., Delworth, T., Latif, M., McAvaney, B., Mitchell, J., Stouffer, R., Taylor, K., 2007. The WCRP CMIP3 multimodel dataset: a new era in climate change research. *Bull. Am. Meteorol. Soc.* 88, 1383–1394.
- Meehl, G., Hi, A., Santer, B., 2009. The mid-1970s climate shift in the Pacific and the relative roles of forced versus inherent decadal variability. *J. Clim.* 22, 780–792.
- Megann, A., New, A., Blaker, A., Sinha, B., 2010. The sensitivity of a coupled climate model to its ocean component. *J. Clim.* 23, 5126–5150.
- Mellor, G.L., Ezer, T., 1995. Sea level variations induced by heating and cooling: an evaluation of the Boussinesq approximation in ocean models. *J. Geophys. Res.* 100, 20565–20577.
- Merrifield, M., 2011. A shift in western tropical Pacific sea level trends during the 1990s. *J. Clim.* 24, 4126–4138.
- Merrifield, M., Maltrud, M., 2011. Regional sea level trends due to a Pacific trade wind intensification. *Geophys. Res. Lett.* 38–L21605. <http://dx.doi.org/10.1029/2011GL049576>.
- Merrifield, M., Thompson, P.R., Lander, M., 2012. Multidecadal sea level anomalies and trends in the western tropical Pacific. *Geophys. Res. Lett.* 39, L13602.
- Meysignac, B., Salas y Melia, D., Becker, M., Llovel, W., Cazenave, A., 2012. Tropic Pacific spatial trend patterns in observed sea level: internal variability and/or anthropogenic signature? *Clim. Past* 8, 787–802.
- Mitrovica, J.X., Tamisiea, M.E., Davis, J.L., Milne, G.A., 2001. Recent mass balance of polar ice sheets inferred from patterns of global sea-level change. *Nature* 409, 1026–1029.
- Palmer, M., Balmaseda, M., Chang, Y.-S., Chepurin, G., Fujii, Y., Good, S., Guinehut, S., Hernandez, F., Martin, M., Masuda, S., Peterson, K., Toyoda, T., Valdivieso, M., G. Vernieres, O.W., Xue, Y., 2014. CLIVAR-GSOP/GODAE intercomparison of ocean heat content: initial results. *CLIVAR Exchanges* (19.1 – February 2014), pp. 8–10.
- Palter, J.B., Griffies, S.M., Galbraith, E.D., Gnanadesikan, A., Samuels, B.L., Klocker, A., 2014. The deep ocean buoyancy budget and its temporal variability. *J. Clim.* 27, 551–573.
- Pardaens, A., Gregory, J., Lowe, J., 2011a. A model study of factors influencing projected changes in regional sea level over the twenty-first century. *Climate Dyn.* <http://dx.doi.org/10.1029/2011GL047678>.
- Pardaens, A.K., Lowe, J.A., Brown, S., Nicholls, R.J., de Gusmo, D., 2011b. Sea-level rise and impacts projections under a future scenario with large greenhouse gas emission reductions. *Geophys. Res. Lett.* 38 (12). <http://dx.doi.org/10.1029/2011GL047678>.
- Peterson, B., Holmes, R., McClelland, J., Vörösmarty, C., Lammers, R., Shiklomanov, A., Shiklomanov, I., Rahmstorf, S., 2012. Increasing river discharge to the Arctic Ocean. *Science* 298, 2171–21738044.
- Pond, S., Pickard, G.L., 1983. *Introductory Dynamical Oceanography*, 2nd Edition. Pergamon Press, Oxford.
- Purkey, S., Johnson, G., 2010. Warming of global abyssal and deep Southern Ocean waters between the 1990s and 2000s: contributions to global heat and sea level rise budgets. *J. Clim.* 23, 6336–6351.
- Rabe, B., Karcher, M., Schauer, U., Toole, J.M., Krishfield, R.A., Pisarev, S., Kauker, F., Gerdes, R., Kikuchi, T., 2011. An assessment of Arctic Ocean freshwater content changes from the 1990s to the 2006–2008 period. *Deep Sea Res. Part I: Oceanogr. Res. Papers* 58 (2), 173–185 <<http://www.sciencedirect.com/science/article/pii/S0967063710002414>>.
- Reynolds, R.W., Rayner, N., Smith, T.M., Stokes, D., Wang, W., 2002. An improved in situ and satellite SST analysis for climate. *J. Clim.* 15, 1609–1625.
- Robson, J., Sutton, R., Lohmann, K., Smith, D., Palmer, M.D., 2012. Causes of the rapid warming of the North Atlantic Ocean in the mid-1990s. *J. Clim.* 25, 4116–4134.
- Roemmich, D., Gilson, J., 2011. The global ocean imprint of ENSO. *Geophys. Res. Lett.* 38 (13). <http://dx.doi.org/10.1029/2011GL047992>.
- Roemmich, D., Gilson, J., Davis, R., Sutton, P., Wijffels, W., Riser, S., 2007. Decadal spinup of the South Pacific subtropical gyre. *J. Phys. Oceanogr.* 37, 162–173.
- Rohling, E., Grant, K., Bolshaw, M., Roberts, A.P., Siddall, M., Hemleben, C., Kucera, M., 2009. Antarctic temperature and global sea level closely coupled over the past five glacial cycles. *Nature Geosci.* 2, 500–504.
- Roullet, G., Madec, G., 2000. Salt conservation, free surface, and varying volume: a new formulation for OGCMs. *JGR* 105, 23927–23947.
- Sallée, J.-B., Speer, K., Morrow, R., 2008. Ocean fronts and their variability in climate modes. *J. Clim.* 21, 3020–3039.
- Sallenger, A.H., Doran, K.S., Howd, P.A., 2012. Hotspot of accelerated sea-level rise on the Atlantic coast of North America. *Nature Geosci.* 2, 884–888.
- Schiller, A., Lee, T., Masuda, S., 2013. Methods and applications of ocean synthesis in climate research. In: Siedler, G., Griffies, S.M., Gould, J., Church, J. (Eds.), *Ocean Circulation and Climate: A 21st Century Perspective*, second ed., International Geophysics Series second ed., vol. 103 Academic Press, pp. 581–608.
- Schwarzkopf, F.U., Böning, C.W., 2011. Contribution of Pacific wind stress to multi-decadal variations in upper-ocean heat content and sea level in the tropical south Indian Ocean. *Geophys. Res. Lett.* 38. <http://dx.doi.org/10.1029/2011GL047651>.
- Shepherd, A., Wingham, D., Wallis, D., Giles, K., Laxon, S., Sundal, A.V., 2010. Recent loss of floating ice and the consequent sea level contribution. *Geophys. Res. Lett.* 37 (13). <http://dx.doi.org/10.1029/2010GL042496>.
- Slangen, A., Katsman, C., van de Wal, R., Vermeersen, L., Riva, R., 2012. Towards regional projections of twenty-first century sea-level change based on IPCC SRES scenarios. *Clim. Dyn.* <http://dx.doi.org/10.1007/s00382-011-1057-6>.
- Stammer, D., 2008. Response of the global ocean to Greenland and Antarctic ice melting. *J. Geophys. Res.* 113. <http://dx.doi.org/10.1029/2006JC004079>.
- Steele, M., Morfley, R., Ermold, W., 2001. PHC: A global ocean hydrography with a high-quality Arctic Ocean. *J. Clim.* 14, 2079–2087.
- Stephens, G., Ward, M., Jr., P.S., L'Ecuyer, T., Kato, S., Hendersen, D., 2012. The global character of the flux of downward longwave radiation. *J. Clim.* 25, 2329–2340.
- Storto, A., Masina, S., Balmaseda, M., Guinehut, S., Martin, M., Peterson, K., Good, S., Valdivieso, M., Haines, K., Köhl, A., Yin, Y., Shi, L., Smith, G., Chang, Y.-S., Vernieres, G., Wang, X., Wang, O., Ferry, T.L.N., Fujii, Y., Hernandez, F., Ishikawa, Y., Masuda, S., 2014. Comparison of steric sea level from ocean reanalyses and objective analyses. *CLIVAR Exchanges* (19.1 – February 2014), pp. 15–17.
- Stouffer, R.J., 2004. Time scales of climate response. *J. Clim.* 17, 209–217.
- Taylor, K., Stouffer, R., Meehl, G., 2012. An overview of CMIP5 and the experiment design. *Bull. Am. Meteorol. Soc.* 93, 484–498.
- Timmermann, A., McGregor, S., Jin, F.-F., 2010. Wind effects on past and future regional sea level trends in the Southern Indo-Pacific. *J. Clim.* 23, 4429–4437.
- Tomczak, M., Godfrey, J.S., 1994. *Regional Oceanography: An Introduction*. Pergamon Press, Oxford, England, 422+VII pp.
- Trenberth, K.E., Hurrell, J., 1994. Decadal atmosphere-ocean variations in the Pacific. *Clim. Dyn.* 9, 303–319.
- Weijer, W., Maltrud, M., Hecht, M., Dijkstra, H., Klijhuis, M., 2012. Response of the Atlantic ocean circulation to Greenland ice sheet melting in a strongly-eddy ocean model. *Geophys. Res. Lett.* 39–L09606. <http://dx.doi.org/10.1029/2012GL051611>.
- Wijffels, S.E., Willis, J., Domingues, C.M., Barker, P., White, N.J., Gronell, A., Ridgway, K., Church, J.A., 2008. Changing expendable bathythermograph fall rates and their impact on estimates of thermohaline sea level rise. *J. Clim.* 21, 5657–5672.
- Wunsch, C., Heimbach, P., 2013. Dynamically and kinematically consistent global ocean circulation and ice state estimates. In: Siedler, G., Griffies, S.M., Gould, J., Church, J. (Eds.), *Ocean Circulation and Climate: A 21st Century Perspective*, second ed., International Geophysics Series second ed., vol. 103 Academic Press, pp. 553–579.
- Wunsch, C., Heimbach, P., 2014. Bidecadal thermal changes in the abyssal ocean. *J. Phys. Oceanogr.* <http://dx.doi.org/10.1175/JPO-D-13-096.1>.
- Wunsch, C., Ponte, R., Heimbach, P., 2007. Decadal trends in sea level patterns: 1992–2004. *J. Clim.* 20, 5889–5911.
- Wunsch, C., Stammer, D., 1998. Satellite altimetry, the marine geoid, and the oceanic general circulation. *Ann. Rev. Earth Planet. Sci.* 26, 219–253.
- Yeager, S.G., Karspeck, A., Danabasoglu, G., Tribbia, J., Teng, H., 2012. A decadal prediction case study: late twentieth-century North Atlantic ocean heat content. *J. Clim.* 25, 5173–5189.
- Yin, J., 2005. A consistent poleward shift of the storm tracks in simulations of 21st century climate. *Geophys. Res. Lett.* 32–L18701. <http://dx.doi.org/10.1029/2005GL023684>.
- Yin, J., 2012. Century to multi-century sea level rise projections from CMIP5 models. *Geophys. Res. Lett.* 39 (17). <http://dx.doi.org/10.1029/2012GL052947>.
- Yin, J., Goddard, P., 2013. Oceanic control of sea level rise patterns along the east coast of the United States. *Geophys. Res. Lett.* 40, 5514–5520.
- Yin, J., Griffies, S.M., Stouffer, R., 2010a. Spatial variability of sea-level rise in 21st century projections. *J. Clim.* 23, 4585–4607.
- Yin, J., Overpeck, J., Griffies, S., Hu, A., Russell, J., Stouffer, R., 2011. Different magnitudes of projected subsurface ocean warming around Greenland and Antarctica. *Nat. Geosci.* 4, 524–528.
- Yin, J., Schlesinger, M., Stouffer, R., 2009. Model projections of rapid sea-level rise on the northeast coast of the United States. *Nat. Geosci.* 2, 262–266.

- Yin, J., Stouffer, R., Spelman, M.J., Griffies, S.M., 2010b. Evaluating the uncertainty induced by the virtual salt flux assumption in climate simulations and future projections. *J. Clim.* 23, 80–96.
- Zhang, R., 2008. Coherent surface-subsurface fingerprint of the Atlantic meridional overturning circulation. *Geophys. Res. Lett.* 35. <http://dx.doi.org/10.1029/2008gl035463>.
- Zhang, X., Church, J.A., 2012. Sea level trends, interannual and decadal variability in the pacific ocean. *Geophys. Res. Lett.* 39 (21). <http://dx.doi.org/10.1029/2012GL053240>.